Engineering Journal

American Institute of Steel Construction

First Quarter 2016 Volume 53, No. 1

www.aisc.org

Analysis and Design of Stabilizer Plates in Single-Plate Shear Connections

PATRICK J. FORTNEY and WILLIAM A. THORNTON

ABSTRACT

Single-plate shear connections experience some magnitude of torsional moment, either due to the lateral torsional buckling phenomena or due to the effects of lap eccentricity. When the required torsional strength of the connection exceeds the available torsional strength of the connection, the designer has two options: alter the geometry of the connection to increase the torsional resistance of the connecting plate or provide stabilizer plates. Thornton and Fortney (2011) provide analysis techniques for accounting for the effects of lap eccentricity and lateral torsional buckling strength. Part 10 of the *Manual* (*Steel Construction Manual,* 14th ed., 2011) presents a summary of the equations used for such an evaluation. However, no discussion was provided by Thornton and Fortney with regard to the size and detailing of a stabilizer plate when such a plate is required. This paper presents recommendations for the analysis with regard to appropriate stabilizer plate cross-sectional dimensions and the attachment of the stabilizer plate to the connecting material and support. Three different types of stabilizer plates are presented along with recommendations for the design and detailing of the stabilizer plates; the impact that each type has on the design of the single-plate shear connection and the supporting column is presented as well.

Keywords: nodal bracing, single-plate shear connections, stabilizer plates, stiffener plates.

INTRODUCTION

Stabilizer plates can be used to counteract the effects of lap eccentricity and to prevent lateral torsional buckling in single-plate shear connections (Thornton and Fortney, 2011). Part 10 of the *Steel Construction Manual* (AISC, 2011) presents equations for evaluating the need for stabilizer plates based on these two considerations. For either limit state, the role of the stabilizer plate in the connection is simply to provide lateral support to the connecting material. In the ideal case, the stabilizer plate is not part of the load path for transferring the beam end shear to the support. In order to minimize the participation of the stabilizer plate in transferring the force to the support, the stiffness that the stabilizer plate provides to the overall connection must be minimized. However, it may not be desirable to provide such a "flexible" stabilizer plate. When this is the case, the role that the stabilizer plate plays in the load path of the beam-to-column connection needs to be considered. When developing analysis and design procedures for stabilizer plates, the following questions should be considered:

Patrick J. Fortney, Ph.D., P.E., S.E., P.Eng., President and Chief Engineer, Cives Engineering Corporation, Roswell, GA (corresponding). Email: pfortney@cives.com

William A. Thornton, Ph.D., P.E., NAE, Corporate Consultant, Cives Engineering Corporation, Roswell, GA. Email: bthornton@cives.com

Paper No. 2013-15

1. What is the role of the stabilizer plate?
2. What types of stabilizer plates need to be considered?
3. What types of analysis and design procedures should be used?
    a. To what degree does the stabilizer plate act as part of the load path in the beam-to-column connection?
    b. What is the impact on the beam-to-column connection design?
    c. What impact does the stabilizer plate have on the supporting member?

These three primary questions are addressed in this paper.

ROLE OF THE STABILIZER PLATE

The purpose of the stabilizer plate is to provide a lateral brace to the single-plate shear connection when the required shear force in the connection exceeds the shear that initiates lateral torsional buckling or to offset the effects of lap eccentricity. A stabilizer plate should only be used when all attempts to work with connection geometry and hardware cannot provide adequate torsional strength. Stabilizer plates not only add unnecessary costs, they potentially change the behavior of the connection and induce rotational demands not accounted for during the frame analyses as well.

The lateral brace can be thought of as a nodal brace, in the sense of AISC *Specification* Appendix 6 (AISC, 2010),

between the connecting plate and the column flange (see Figure 1), thus providing lateral stability to the connecting plate. To provide adequate bracing, both the axial strength and axial stiffness of the stabilizer plate must be considered. The required brace force in the stabilizer plate, P_s, would need to be transferred from the connection plate to the stabilizer plate. The bracing load acts at approximately mid-length of the stabilizer plate. If the ends of the stabilizer plate are connected to the column flanges, one-half of the stabilizer plate is in compression, while the other half is in tension (see Figure 1). The axial force can be resisted either through bearing at the plate-column flange interface on the compression side or through a weld at the plate-column flange interface on the tension side.

TYPES OF STABILIZER PLATES

In order to assess the number of different types of stabilizer plates that might be used, not only the connected beam and column must be considered, but also the members framing into the joint from the perpendicular direction. The role the stabilizer plate plays in transporting the beam end shear to the support also needs to be considered.

For the purposes of the discussion presented in this paper, the authors assume that there are two different types of connections provided for the perpendicular members: simple shear connections and moment connections. When simple shear connections are used to connect the perpendicular members, it is assumed that the joint is clean (i.e., no continuity plates or web doublers). When moment connections are used to connect the perpendicular members, it is assumed that continuity plates are required and the shear connection plate is fitted to the continuity plates. Note that if the perpendicular members are moment-connected and continuity plates are not required, the joint is clean and, for the purpose of a discussion regarding stabilizer plates, can be considered to be no different than when the perpendicular members were shear-connected. Additionally, it is not uncommon to see the connection plate in a single-plate shear connection fitted to the flanges of a spandrel beam in a beam-to-spandrel beam connection or a beam-to-beam connection with a supported beam on only one side of the support beam. This condition is similar to a connection plate fitted to the continuity plates in a joint with moment connections framing in from the perpendicular direction.

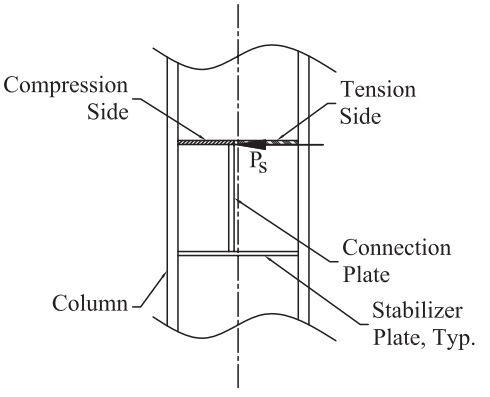

Fig. 1. Brace force, P_s*, provided by stabilizer plate.*

Figure 2 shows sketches of three different types of stabilizer plates: types I, II and III. Type I and type II stabilizer plates can be used at joints where the perpendicular members are shear connected (a clean joint). Where the perpendicular member is moment-connected and continuity plates are required, the type III stabilizer plate would be required. Type Ia and type Ib stabilizer plates are assumed to play no role in transporting the required beam end shear. Types II (if not permitted to float) and III will play a role in the transport of the beam end shear.

The type Ia stabilizer plate is not practical. This type of stabilizer plate would certainly raise concerns in regard to surviving transportation and erection. It is presented only as a tool to facilitate a discussion regarding the analysis and design of the plate. The type Ib stabilizer plate will provide a more practical approach to providing lateral stability of the single-plate shear connection while not participating in the load path for the connection.

Analysis and Design of Stabilizer Plates

A stabilizer plate may increase the amount of rotational restraint provided by the connection. One simple way of eliminating any concern in this regard is to make no attachment of the stabilizer plate to the column flanges. Note that this approach can be considered only for type I and II plates; it would not be an option for a type III stabilizer plate, which also acts as a continuity plate for the moment-connected beam framing into the joint from the perpendicular direction. If the stabilizer plate is not attached to the column flanges, it would be attached to the connection plate only, and given a length, l_s (see Figure 3)—such that the stabilizer plate fits within the column flanges—but is allowed to translate relative to the column flanges as the beam undergoes simple beam end rotation under the presence of load. In essence, the stabilizer plate is permitted to "float" between the column flanges.

Where a welded connection of the stabilizer plate to the column flange is neither required nor desired, the required axial force, P_s, in the stabilizer plate would be transferred to the column flange through bearing. Under this condition, because no weld is provided on the "tension" side of the stabilizer plate (refer to Figures 1 and 3), buckling of the stabilizer plate would need to be considered when determining the cross-sectional dimensions of the stabilizer plate. Where a welded connection is required or desired at the stabilizer

plate-column flange interface, buckling of the stabilizer plate would not be a concern because the axial force in the stabilizer plate would be resisted on the tension side of the plate.

Type Ia Stabilizer Plates

Figure 4 shows a sketch representative of a type Ia stabilizer plate. This type of stabilizer plate is relatively flexible and can be reasonably assumed to provide no additional stiffness or rotational resistance to the single-plate shear connection. Furthermore, it is reasonable to assume that the stabilizer plate provides no appreciable redundancy to the connection. That is, the stabilizer plate is not part of the load path for transporting the required beam end shear to the support. Therefore, the design of the single-plate shear connection would follow established design procedures (Part 10 of the AISC *Manual*). For this type of stabilizer plate, the required cross-sectional dimensions can be established as follows.

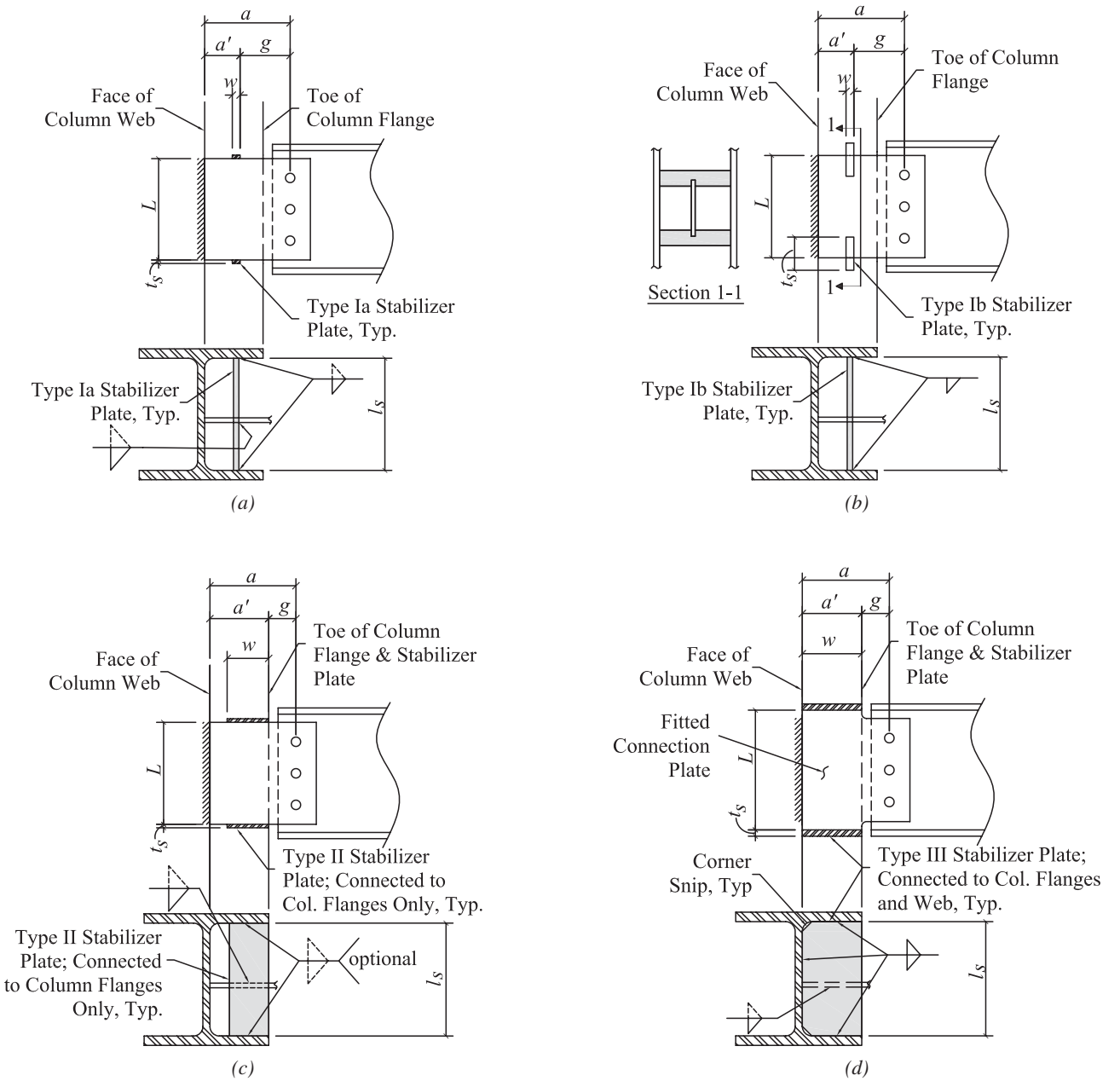

Fig. 2. Options for stabilizer plates: (a) type Ia; (b) type Ib; (c) type II; (d) type III.

Assuming nodal bracing, the required axial strength of the stabilizer plate can be taken as given in *Specification* Equation A-6-7 (AISC, 2010). A form of that equation is shown here in Equation 1.

$$P_S = \frac{0.02 M_b C_d}{L} \tag{1}$$

where

P_s = the required axial strength of the stabilizer plate
$M_b = M_{ba} = R_a a$ (ASD), $M_{bu} = R_u a$ (LRFD)
$C_d = 1.0$
L = connection length (see Figure 2)
R = R_a (ASD), R_u (LRFD)

Taking the axial tensile strength of the stabilizer plate as

$$\phi P_n = \phi F_y A_s \qquad \text{(LRFD)} \tag{2a}$$

$$\frac{P_n}{\Omega} = \frac{F_y A_s}{\Omega} \qquad \text{(ASD)} \tag{2b}$$

where A_s is the cross-sectional area of the stabilizer plate, the cross-section of the stabilizer plate can be determined by setting Equation 1 equal to Equation 2 and rearranging to solve for A_s, as shown in Equation 3.

$$\phi F_y A_s = \frac{0.02 M_{bu} C_d}{L}$$
$$\phi F_y A_s L = 0.02 M_{bu} C_d$$
$$\phi F_y A_s L = 0.02 R_u a (1.0)$$

$$A_s = \frac{0.02 R_u a}{\phi F_y L} \qquad \text{(LRFD)} \tag{3a}$$

$$\frac{F_y A_s}{\Omega} = \frac{0.02 M_{ba} C_d}{L}$$
$$\frac{F_y A_s L}{\Omega} = 0.02 M_{ba} C_d$$
$$\frac{F_y A_s L}{\Omega} = 0.02 R_a a (1.0)$$

$$A_s = \frac{0.02 \Omega R_a a}{F_y L} \qquad \text{(ASD)} \tag{3b}$$

In Equations 3a and 3b, $\phi = 0.75$ and $\Omega = 2.00$.

Similarly, the required axial stiffness of the stabilizer plate can be taken as given in *Specification* Equation A-6-8, and shown in Equation 4.

$$\beta_S = \frac{1}{\phi}\left(\frac{10 M_{bu} C_d}{aL}\right) \qquad \text{(LRFD)} \tag{4a}$$

$$\beta_s = \Omega\left(\frac{10 M_{ba} C_d}{aL}\right) \qquad \text{(ASD)} \tag{4b}$$

where

β_s = required axial stiffness of the stabilizer plate
$M_{bu} = R_u a$, $M_{ba} = R_a a$
C_d = 1.0
L = connection depth
a = the unbraced length of the connection plate

The axial stiffness of the stabilizer plate is taken as

$$\beta_s = \frac{A_s E}{\frac{l_s}{2}} = \frac{2 A_s E}{l_s} \tag{5}$$

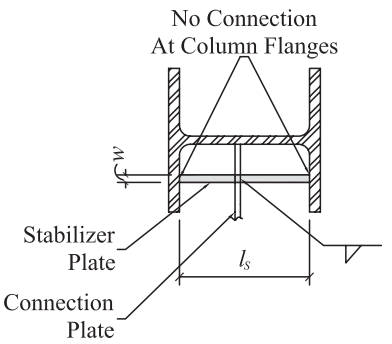

Fig. 3. Type I floating stabilizer plate (no connection to column flanges).

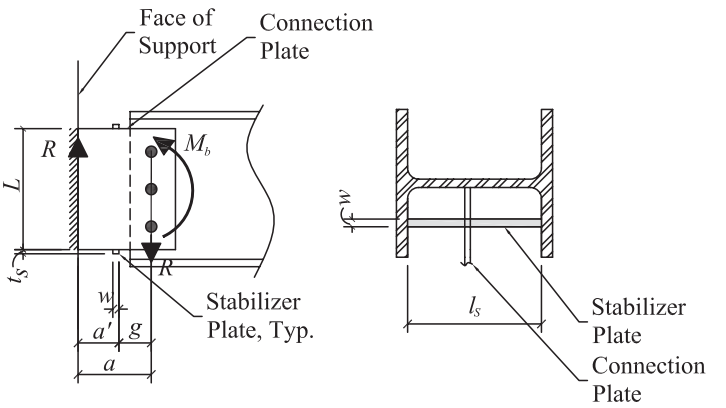

Fig. 4. Type Ia stabilizer plate (flexible).

where l_s is the length of the stabilizer plate. Note that in Equation 5, the stiffness of the stabilizer plate is based on the length of the plate between the connection plate and the column flange ($l_s/2$). The cross-section of the stabilizer can be determined by setting Equation 4 equal to Equation 5 and rearranging to solve for A_s, as shown in Equation 6.

$$\frac{1}{\phi}\left(\frac{10M_{bu}C_d}{aL}\right)=\frac{2A_sE}{l_s}$$

$$A_s=\frac{10M_{bu}C_dl_s}{2\phi aLE}=\frac{10R_ua(1.0)l_s}{2\phi aLE}$$

$$A_s=\frac{5R_ul_s}{\phi LE} \qquad \text{(LRFD)} \tag{6a}$$

$$\Omega\left(\frac{10M_{ba}C_d}{aL}\right)=\frac{2A_sE}{l_s}$$

$$A_s=\frac{10\Omega M_{ba}C_dl_s}{2aLE}=\frac{10\Omega R_aa(1.0)l_s}{2aLE}$$

$$A_s=\frac{5\Omega R_al_s}{LE} \qquad \text{(ASD)} \tag{6b}$$

In Equations 6a and 6b, $\phi = 0.75$, $\Omega = 2.00$.

When using a flexible stabilizer plate, it can be assumed that little or no additional connection stiffness is provided and that no additional rotational restraint is provided by the connection. For these given assumptions, the single-plate shear connection would be designed using the same procedures used if the stabilizer plate were not present. The stabilizer plate cross-section would be determined using Equations 3 and 6 to check against the required axial strength and stiffness.

The attachment of the stabilizer plate to the connection plate can be made with a fillet weld sized to transfer the required axial strength as determined by Equation 1. Note that the weld lengths will need to be at least as long as four times the fillet weld size (Section J2b of AISC 360-10). Therefore, the stabilizer plate width, w, will need to be at least ¾ in. (assuming a 3⁄16-in. fillet weld is used). Because it is assumed that the type Ia plate does not participate in the load path for transporting the beam end reaction, only the axial force, P_s, need be considered in the determination of the size of the stabilizer plate or its attachment.

Where the stabilizer plate axial force is transferred to the column flange through bearing and no welded connection is made at the column flanges, the cross-sectional dimensions of the stabilizer plate will be controlled by bearing or buckling. Equations 7 and 8 give design equations for checking bearing strength at the column flange–stabilizer plate interface and buckling of the stabilizer plate, respectively, where P_s is determined by Equation 1.

$$P_{su} \le \phi 1.8F_yA_s \qquad \text{(LRFD)} \tag{7a}$$

$$P_{sa} \le \frac{1.8F_yA_s}{\Omega} \qquad \text{(ASD)} \tag{7b}$$

In Equations 7a and 7b, $\phi = 0.75$ and $\Omega = 2.00$.

$$P_{su} \le \phi F_{cr}A_s \qquad \text{(LRFD)} \tag{8a}$$

$$P_{sa} \le \frac{F_{cr}A_s}{\Omega} \qquad \text{(ASD)} \tag{8b}$$

In Equations 8a and 8b, $\phi = 0.90$ and $\Omega = 1.67$.

Example Problem 1—Flexible Stabilizer Plate, Type Ia

Problem Statement

Figure 5 shows a single-plate shear connection used as a beam end connection for a W12×35 framing to the web of a W12×30 column. The required shear force for the design of the connection is $R_u = 22$ kips.

1. Determine if a stabilizer plate is required based on
   a. Lateral torsional buckling of the plate.
   b. The effect of lap eccentricity.
2. Whether a stabilizer plate is required or not, determine the required cross-sectional dimensions for a type Ia A36 stabilizer plate. The stabilizer plate will be welded to the column flanges. Specify the welds at the column flanges and connection plate. Assume a one-sided 3⁄16-in. fillet weld is used for attaching the stabilizer plate.

Solution

Part 1a

The lateral torsional buckling strength of the plate is (Thornton and Fortney, 2011)

$$\phi R_n = \phi \frac{1{,}500\pi L t^3}{a^2}$$
$$= (0.9)\left(\frac{(1{,}500 \text{ ksi})\pi(9 \text{ in.})(0.25 \text{ in.})^3}{(5.0 \text{ in.})^2} \right)$$
$$= 23.8 \text{ kips} > 22.0 \text{ kips} \quad \rightarrow \quad \text{stabilizer plate not required}$$

Part 1b

The required torsional moment strength due to lap eccentricity is (Thornton and Fortney, 2011)

$$M_{tu} = R\left(\frac{t_w + t_p}{2} \right)$$
$$= (22 \text{ kips})\left(\frac{0.30 \text{ in.} + 0.25 \text{ in.}}{2} \right)$$
$$= 6.05 \text{ kip-in.}$$

The available torsional moment strength is (Thornton and Fortney, 2011)

$$\phi M_t = \left[\phi_v \left(0.6F_{yp}\right) - \frac{R_u}{Lt_p} \right] \left(\frac{Lt_p^2}{2} \right) + \frac{2R_u^2 \left(t_w + t_p\right) b_f}{\phi_b F_{yb} L_s t_w^2}$$
$$= \left[(1.0)(0.6)(36 \text{ ksi}) - \frac{22 \text{ kips}}{(9 \text{ in.})(0.25 \text{ in.})} \right] \left(\frac{(9 \text{ in.})(0.25 \text{ in.})^2}{2} \right) + \frac{(2)(22 \text{ kips})^2 (0.30 \text{ in.} + 0.25 \text{ in.})(6.56 \text{ in.})}{(0.90)(50 \text{ ksi})(28 \text{ ft})(12 \text{ in./ft})(0.30 \text{ in.})^2}$$
$$= 3.33 \text{ kip-in.} + 2.57 \text{ kip-in.}$$
$$= 5.90 \text{ kip-in.} < 6.05 \text{ kip-in.} \quad \rightarrow \quad \text{stabilizer plate is required}$$

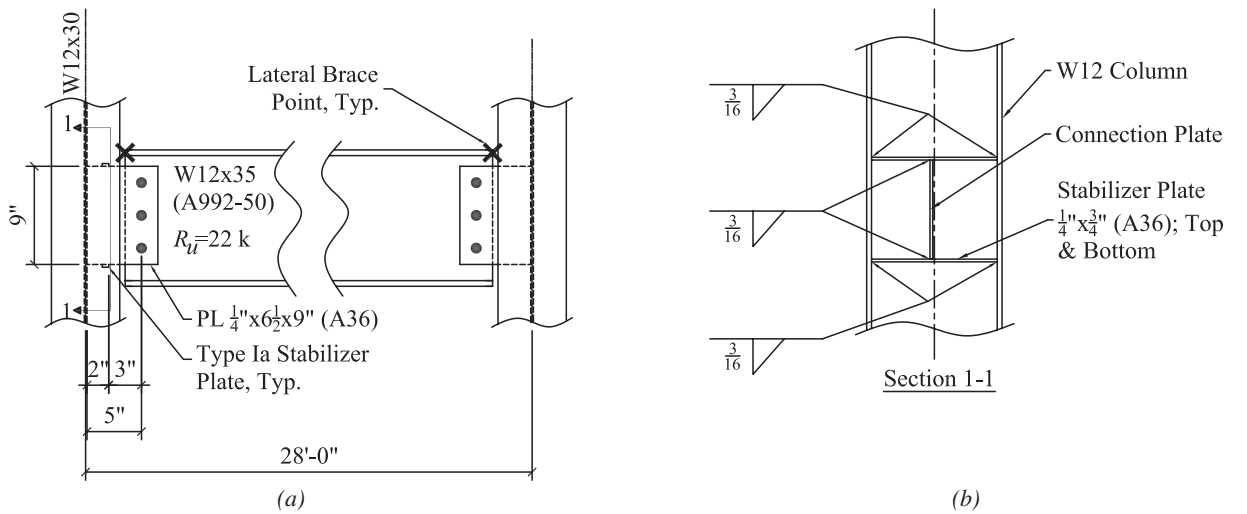

Fig. 5. Single-plate shear connection referenced in Example Problem 1: (a) elevation; (b) final stabilizer plate details.

Part 2

Because a 3⁄16-in. fillet weld is used to attached the stabilizer plate, the width of the plate must be at least (4)(0.1875 in.) = 0.750 in.

Stabilizer plate size based on required axial strength using Equation 3a:

$$A_s = \frac{0.02R_u a}{\phi F_y L}$$
$$= \frac{(0.02)(22 \text{ kips})(5 \text{ in.})}{(0.75)(36 \text{ ksi})(9 \text{ in.})}$$
$$= 0.0091 \text{ in.}^2$$

Assuming the width of the plate is 0.750 in., the required plate thickness is:

$$A_s = wt_s$$
$$0.0091 \text{ in.}^2 = (0.750 \text{ in.})t_s$$
$$t_s = \frac{0.0091 \text{ in.}^2}{0.750 \text{ in.}}$$
$$= 0.012 \text{ in.}$$

Good detailing practice would suggest using at least a ¼-in. plate, which is greater than t_s = 0.012 in. Therefore,

Use a ¼-in. × ¾-in. plate.

Stabilizer plate size based on required axial stiffness using Equation 6a:

$$l_s = \left(d - 2t_f\right)_{column}$$
$$= 12.3 \text{ in.} - (2)(0.44 \text{ in.})$$
$$= 11.4 \text{ in.}$$
$$A_s = \frac{5R_u l_s}{\phi LE}$$
$$= \frac{(5)(22 \text{ kips})(11.4 \text{ in.})}{(0.75)(9 \text{ in.})(29{,}000 \text{ ksi})}$$
$$= 0.006 \text{ in.}^2 < 0.0091 \text{ in.}^2 \quad \rightarrow \quad \text{strength controls over stiffness}$$

Use a ¼-in. × ¾-in. stabilizer plate.

Attachment of Stabilizer Plate to Single-Plate Shear Connection and Column Flange

The required axial force in the stabilizer plate is determined using Equation 1.

$$P_{Su} = \frac{0.02M_{bu}C_d}{L}$$
$$= \frac{(0.02)(22 \text{ kips})(5 \text{ in.})(1.0)}{9.0 \text{ in.}}$$
$$= 0.244 \text{ kips}$$

The width of the stabilizer plate is 0.750 in. Check that a 3⁄16-in. single-sided fillet weld at the connection plate and column flange is sufficient.

$$\phi R_w = 1.392Dnl\left(1+0.5\sin^{1.5}\theta\right)$$
$$= (1.392)(3 \text{ sixteenths})(1)(0.75 \text{ in.})\left(1+0.5\sin^{1.5} 90°\right)$$
$$= 4.70 \text{ kips} > 0.244 \text{ kips} \quad \textbf{OK}$$

Use a 3⁄16-in. fillet weld at the stabilizer plate-to-connection plate and stabilizer plate-to-column flange interfaces.

Note that if one were to choose not to attach the stabilizer plate to the column flanges, the stabilizer plate would need to be checked for (1) bearing against the column flanges and (2) buckling on the compression side of the stabilizer plate.

See Figure 5b for a sketch of the details of the stabilizer plate and its attachments.

Type Ib Stabilizer Plates

Type Ib Plate Geometry

The type Ib stabilizer plate is similar to the type Ia plate in that it is assumed that the stabilizer plate does not play a role in transferring the beam end reaction to the support. Therefore, as with the type Ia configuration, the single-plate shear connection design procedure of *Manual* Part 10 applies. With the type Ia stabilizer plate, a welded connection is required at the stabilizer-to-connection plate interface. An attachment at this location is not required with the type Ib plate. As can be seen in Figure 6, the type Ib plate is notched around the connection plate, and the required lateral bracing of the connection plate is achieved through bearing of the connection plate on the notched portion of the stabilizer plate. A weld is used to transfer the axial load in the stabilizer plate to the column flange. Both ends of the stabilizer plate are welded to the column flange so, regardless of the direction of the P_s load, the tension side of the stabilizer plate will provide the entire brace force. Thus, stabilizer buckling does not need to be checked.

The height of the notch, h_n, should be sufficient to transfer the P_s force in bearing and also provide vertical clearance such that the connection plate does not contact the stabilizer during simple beam end rotation. The height of the contact area between the connection plate and the stabilizer, h_p, will be driven by what is required for bearing. The authors recommend a vertical clearance of 0.5 times the thickness of the connection plate, t_p.

The width of the notch, w_n, should be wide enough to provide horizontal clearance of the connection plate but not so wide as to allow undesirable lateral movement of the connection plate. The authors recommend a notch width of t_p + 1⁄16 in.

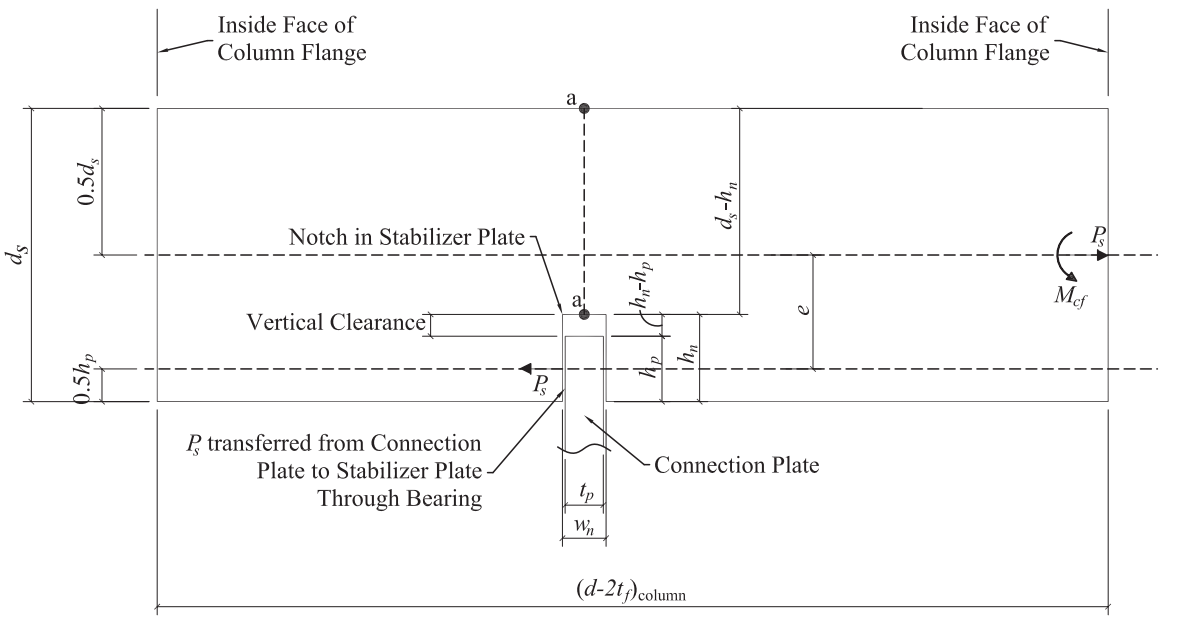

Fig. 6. Type Ib stabilizer plate.

The total height of the stabilizer, d_s, should be sufficient to transfer the axial force, P_s, and the moment, M_{notch}, present at section a-a (see Figure 6 and 7). Section a-a is the critical section for bending and axial load (discussed later). The authors recommend a stabilizer height, d_s, equal to or greater than 2 times the height of the notch, h_n.

For design, trial geometry of the notch can be assumed to have height $h_n = 2$ times the thickness of the connection plate ($h_n = 2t_p$) and the height of the contact area of the connection plate with the stabilizer plate to be $h_p = 0.75$ times the height of the notch ($h_p = 1.5t_p$).

Type Ib Plate Analysis and Design

At the connection plate–stabilizer plate interface, the brace force is transferred at the center of the contact area of the two plates. At the stabilizer–column flange interface, the load is transferred at mid-depth of the stabilizer plate. As can be seen in Figure 6, the two forces act along two different lines of action. Thus, an eccentricity, e, exists. This eccentricity is resolved by splitting the stabilizer vertically at section a-a located at mid-width ($w_n/2$) of the notch. Figures 7 and 8 show the free-body diagrams of the compression side and tension side of section a-a, respectively.

As can be seen in Figure 7, the stabilizer plate is required to transfer the axial load, P_s, and a moment, M_{notch}, at the notch (section a-a). P_s acts at one-half the height of the vertical dimension of the contact surface of the connection plate with the stabilizer (h_p). The P_s force acts on section a-a at the centroid of section a-a. The distance between the two lines of action is $0.5(d_s + h_n - h_p)$. The moment at the notch is

$$\sum M_i = 0 = P_s\left[0.5(d_s + h_n - h_p)\right] - M_{notch}$$

$$M_{notch} = P_s\left[0.5(d_s + h_n - h_p)\right]$$

Referring to Figure 8, it can be seen that the stabilizer-to-column flange interface must transfer the required axial force, P_s, and a moment, M_{cf}. The distance between these two lines of action is $0.5h_n$. The moment at the face of the column is

$$\sum M_{cf} = 0 = -P_s(0.5h_n) + M_{notch} - M_{cf}$$

$$M_{cf} = M_{notch} - 0.5h_nP_s$$

Comparing the moments, M_{notch} and M_{cf}, it can be deduced that the moment M_{notch} will always be larger than M_{cf} ($M_{cf} = M_{notch} - 0.5h_nP_s$). The height of the stabilizer at section a-a is smaller than at the face of the column. Thus, section a-a is the critical section for bending. The axial force, P_s, acts at both section a-a and at the face of the column. Because section a-a has a smaller cross-sectional area, section a-a is the critical section for axial load. Thus, the combination of bending and tension yield will be checked at section a-a. This check will be done by checking tension yield for a force, N_{Tot}, equal to the sum of P_s plus the equivalent normal force of the moment, M_{notch}. The weld at the face of the column will be sized for the combination of axial load, P_s, and moment, M_{cf}.

Checks at Section a-a

The total equivalent axial force acting on section a-a is

$$N_{Tot} = P_s + N_{eq}$$

where

$$N_{eq} = \frac{4M_{notch}}{d_s - h_n}$$

$$N_{Tot} = P_s + \frac{4M_{notch}}{d_s - h_n} \quad (9)$$

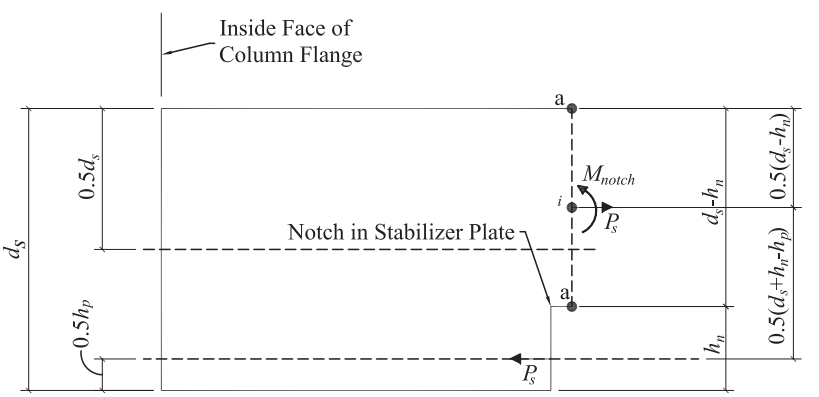

Fig. 7. Type Ib stabilizer plate—free-body diagram: compression side.

The required plate thickness, t_s, for tension yield is

$$\phi T_n = \phi F_y (d_s - h_n) t_s = N_{Tot}$$

$$t_s \geq \frac{N_{Tot,u}}{\phi F_y (d_s - h_n)} \qquad \text{(LRFD)} \qquad (10a)$$

$$\frac{T_n}{\Omega} = \frac{F_y (d_s - h_n)}{\Omega} = N_{Tot,a}$$

$$t_s \geq \frac{\Omega N_{Tot,a}}{F_y (d_s - h_n)} \qquad \text{(ASD)} \qquad (10b)$$

In Equations 10a and 10b, $\phi = 0.90$, $\Omega = 1.67$.

Bearing Check at the Notch

The plate provides lateral bracing through bearing of the stabilizer-connection plate bearing. Thus, the required contact area of the plate is given by Equation J7-1 of the *Specification*.

$$R_n = 1.8 F_y A_{pb}$$

Taking A_{pb} as the contact height, h_p, times the thickness of the stabilizer plate, t_s, the nominal bearing strength is

$$R_n = 1.8 F_y h_p t_s$$

Thus, the required plate thickness based on bearing is

$$\phi R_n = 1.8 F_y h_p t_s \geq P_{su}$$

$$t_s \geq \frac{P_{su}}{\phi 1.8 F_y h_p} \qquad \text{(LRFD)} \qquad (11a)$$

$$\frac{R_n}{\Omega} = \frac{1.8 F_y h_p t_s}{\Omega} \geq P_{sa}$$

$$t_s \geq \frac{\Omega P_{sa}}{1.8 F_y h_p} \qquad \text{(ASD)} \qquad (11b)$$

In Equations 11a and 11b, $\phi = 0.75$, $\Omega = 2.00$, and F_y is the smaller of the yield strengths of the stabilizer and connection plates.

Weld at the Column Flange

The weld is designed for the combination of axial load, P_s, and moment, M_{cf}. As discussed in other parts of the paper, the weld is sized for a total axial load equal to the sum of P_s plus N_{eq}, where N_{eq} is equal to $4M_{cf}/d_s$.

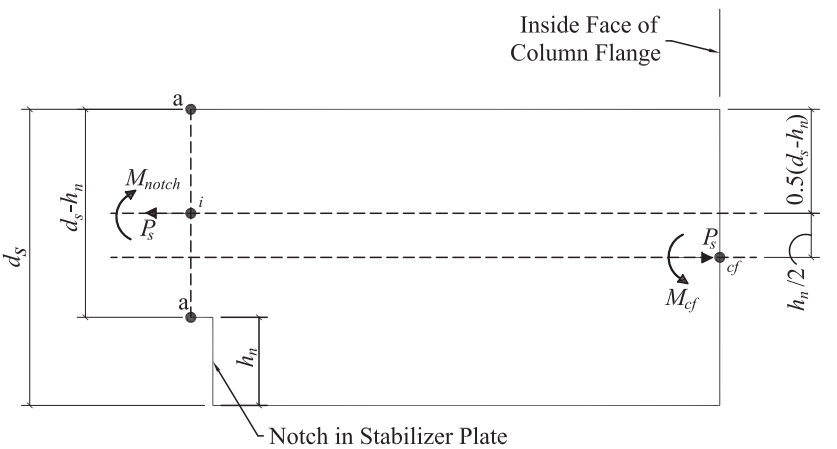

Fig. 8. Type Ib stabilizer plate—free-body diagram: tension side.

Example Problem 2—Type Ib Stabilizer Plate

Figure 9a shows a W16×26 framing to the web of a W14×90 column. The required beam end reaction is R_u = 50 kips. Checks for connection plate lateral torsional buckling and lap eccentricity show that the connection plate is sufficiently strong for these checks without the need of stabilizer plates. However, a type Ib plate is used with the connection. Assume the height of the notch is ¾ in.

1. Generate trial stabilizer and notch dimensions.

2. Determine the required thickness of the type Ib plate.

3. Determine the weld size required at the stabilizer-to-column flange interfaces.

All material is Grade 50.

Solution

Part 1

The length of the stabilizer plate, l_s, is

$$\begin{aligned} l_s &= (d - 2t_f)_{column} \\ &= [14.0 \text{ in.} - (2)(0.71 \text{ in.})] \\ &= 12.6 \text{ in.} \end{aligned}$$

The connection plate thickness, t_p, is 0.375 in. Assume the height of the notch, h_n, is

$$\begin{aligned} h_n &= 2t_p \\ &= (2)(0.375 \text{ in.}) \\ &= 0.75 \text{ in.} \end{aligned}$$

The width of the notch, w_n, is

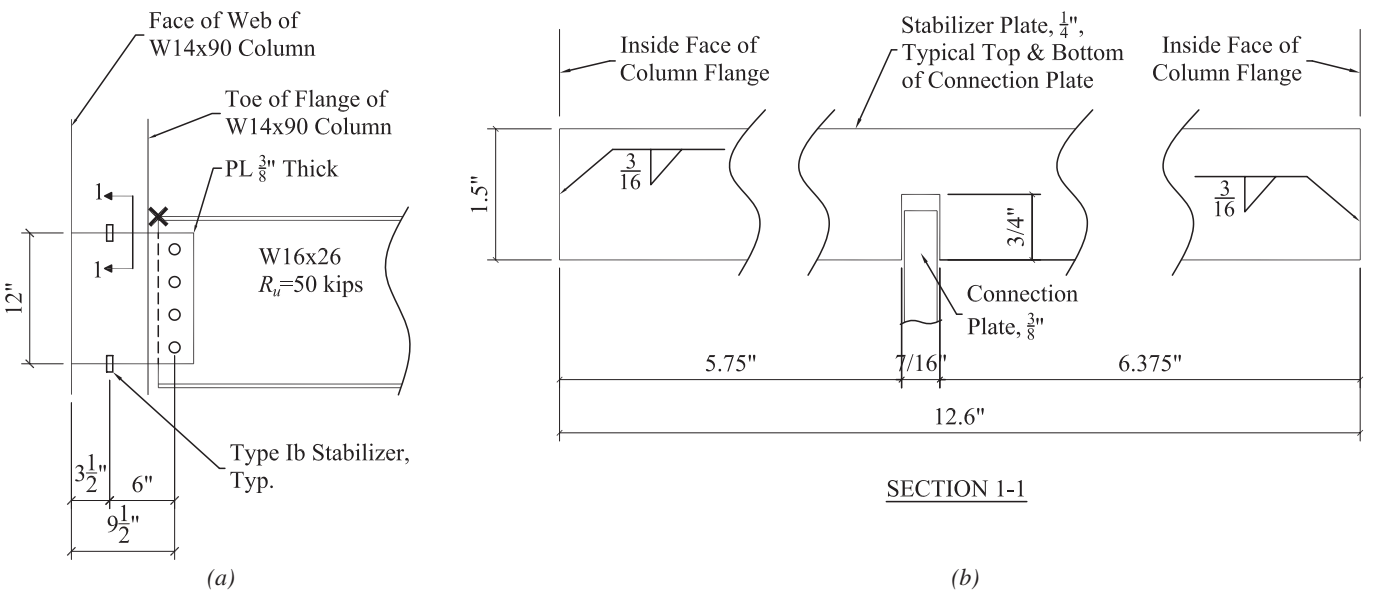

Fig. 9. Connection and details for Example Problem 2: (a) elevation; (b) final details of stabilizer plate.

$$w_n = t_p + 1/16 \text{ in.}$$
$$= 0.375 \text{ in.} + 0.0625 \text{ in.}$$
$$= 0.4375 \text{ in.}$$

Assume the height the contact area of the stabilizer with the connection plate, h_p, is

$$h_p = h_n - 0.5t_p$$
$$= 0.75 \text{ in.} - (0.5)(0.375 \text{ in.})$$
$$= 0.563 \text{ in.}$$

The depth of the stabilizer is estimated to be 2 times the notch depth, h_n. The depth, d_s, is estimated as

$$d_s = 2h_n$$
$$= (2)(0.75 \text{ in.})$$
$$= 1.5 \text{ in.}$$

Try a 1.5-in.-deep stabilizer with a ¾-in.-high × 7/16-in.-wide notch.

Part 2

The required axial force in the stabilizer is given by Equation 1 as

$$P_{su} = \frac{0.02M_{bu}C_d}{L}$$
$$= \frac{(0.02)(50 \text{ kips})(9.50 \text{ in.})(1.0)}{12.0 \text{ in.}}$$
$$= 0.792 \text{ kips}$$

Checks on Section a-a

The stabilizer thickness required for tension yield is (see Equation 10a)

$$M_{notch,u} = P_s\left[0.5(d_s + h_n - h_p)\right]$$
$$= (0.792 \text{ kips})\left[(0.5)(1.5 \text{ in.} + 0.75 \text{ in.} - 0.563 \text{ in.})\right]$$
$$= 0.666 \text{ kip-in.}$$

$$N_{eq} = \frac{4M_{notch}}{d_s - h_n}$$
$$= \frac{(4)(0.666 \text{ kip-in.})}{1.5 \text{ in.} - 0.75 \text{ in.}}$$
$$= 3.55 \text{ kips}$$

$$t_s \geq \frac{N_{Tot,u}}{\phi F_y (d_s - h_n)}$$
$$\geq \frac{0.792 \text{ kips} + 3.55 \text{ kips}}{(0.9)(50 \text{ ksi})(1.5 \text{ in.} - 0.75 \text{ in.})}$$
$$\geq 0.129 \text{ in.}$$

Check at Notch

The stabilizer thickness required for bearing is

$$t_s \geq \frac{P_{su}}{\phi 1.8 F_y h_p}$$
$$\geq \frac{0.792 \text{ kips}}{(0.75)(1.8)(50 \text{ ksi})(0.75 \text{ in.})}$$
$$\geq 0.0156 \text{ in.}$$

Tension yield on section a-a controls; required t_s is greater than or equal to 0.129 in. Use a minimum plate thickness of 0.25 in.

Provide a ¼-in. × 1½-in. × 12⅝-in. stabilizer with a 7⁄16-in. × ¾-in. notch.

Part 3

The weld at the column flange must transfer the required axial force, $P_{su} = 0.792$ kips, and the required moment, M_{cfu}, equal to

$$M_{cfu} = M_{notch,u} - 0.5 h_n P_{su}$$
$$= 0.666 \text{ kip-in.} - (0.5)(0.75 \text{ in.})(0.792 \text{ kips})$$
$$= 0.369 \text{ kip-in.}$$

The total required force for the design of the weld is

$$N_{Tot} = P_{su} + \frac{4 M_{cfu}}{d_s}$$
$$= 0.792 \text{ kips} + \frac{(4)(0.369 \text{ kip-in.})}{1.5 \text{ in.}}$$
$$= 1.78 \text{ kips}$$

The weld size required is

$$D_{req} = \frac{N_{Tot}}{1.392 l \mu n}$$
$$= \frac{1.78 \text{ kips}}{(1.392)(1.5 \text{ in.})(1.5)(1)}$$
$$= 0.568 \text{ sixteenths of an inch}$$

Provide a minimum 3⁄16-in. fillet weld at the column flanges.

The final details of the stabilizer and the welds are shown in Figure 9b.

Type II Stabilizer Plates

Figure 2c shows a type II stabilizer plate. Type II is a variation of the type I with three primary differences: (1) the type II plate has a significantly larger cross-sectional area than what would be required based on the stabilizer plate's required strength and stiffness; (2) the type II plate will qualitatively provide more stiffness to the beam connection than will type I; and (3) the length of the weld at the stabilizer plate to the connection plate is longer, potentially producing a couple that should be considered in the design of the connection and, therefore, acting as part of the load path for transporting beam end shear to the support.

If the type II plate is permitted to float, the design procedure of the single-plate shear connection should be in accordance with the procedure shown in Part 10 of the *Manual*. If not permitted to float and the ends of the stabilizer are welded to the column flanges, the stabilizer will participate in the transfer of the beam end connection to the support. In this case, the *Manual* Part 10 procedure can be adjusted to use "*g*" in place of "*a*." Additionally, the minimum plate

thickness requirement for extended shear plate connections as well as the $(\frac{5}{8})t_p$ weld requirement for both conventional and extended shear plate connections can be ignored.

For the following methodology, refer to Figures 10, 11, and 12. Figure 10 shows a generalized free-body diagram of single-plate shear connection in the presence of a stabilizer plate along with the distribution of shear and moment over the span of the connection plate. Figure 11 shows a specific solution when the bolt group is designed for a moment equal to $M_b = Ra$, while Figure 12 shows a specific solution when the bolt group is designed for a moment $M_b = Rg$.

A Generalized Solution

Refer to Figure 10 for the following discussion.

Shear and Moment at the Bolt Group

Referring to the shear and moment acting on the bolt group,

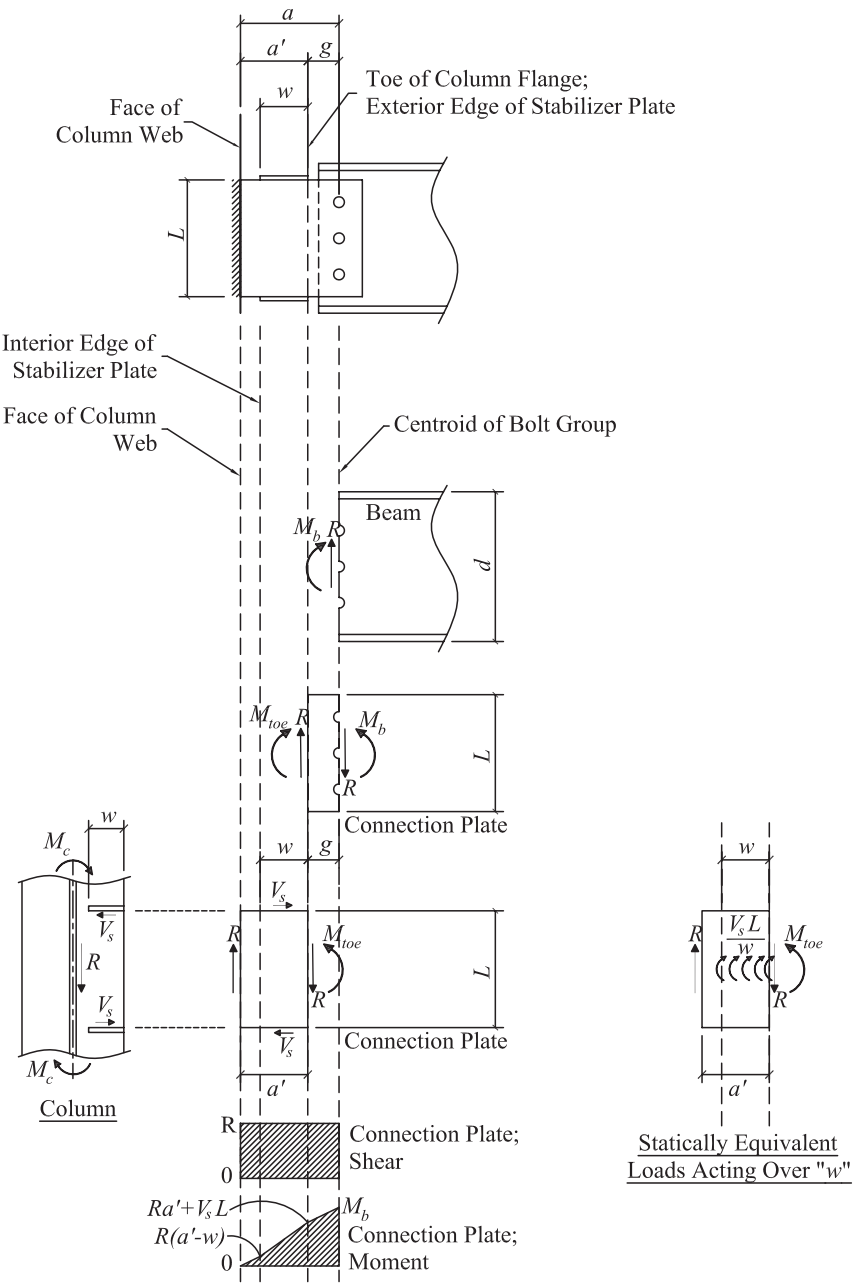

Fig. 10. Generalized free-body diagram of the connection plate in the presence of a stabilizer plate.

the shear in the bolt group, R, is considered to be the beam end reaction. The moment acting on the bolt group is given as M_b.

Shear and Moment on Connection Plate Over the "g" Distance

The shear and moment acting on the bolt group location is R and M_b, respectively. The shear acting on the left edge of the plate (at the toe of the column flange) by inspection is R. The moment, M_{toe}, at the left edge of the plate is

$$\Sigma M_{toe} = 0 = Rg - M_b + M_{toe}$$
$$M_{toe} = M_b - Rg \tag{12}$$

Shear and Moment on Connection Plate Over the "a′" Distance

The shear acting on the left edge of the plate (at the face of the web) by inspection is R. Because it is assumed that only shear is delivered to the support, the moment at this location is considered to be zero. The horizontal shear acting at the stabilizer plate-to-connection plate interface, V_s, is

$$\sum M_{web} = 0 = -M_{toe} + Ra' + \frac{2V_sL}{2}$$
$$V_s = \frac{M_{toe} - Ra'}{L} \tag{13}$$

Loads Acting on Column

The loads acting at the connection plate-to-column web and stabilizer plate-to-connection plate interfaces are transferred to the column. As can be seen in Figure 8, the column web is subjected to a vertical shear equal to R, and the column is subjected to a weak-axis bending moment equal to V_sL.

Shear and Moment Distribution in Connection Plate

Figure 8 shows the resulting shear and moment distribution along the span of the connection plate. The shear is constant with a magnitude of R over the span of the connection from the face of the web to the bolt group. The moment at the face of the web is zero. The moment at the interior side of the stabilizer plate is

$$M_{s,i} = R(a' - w) \tag{14}$$

and is distributed linear at a slope equal to R.

The moment at the interior side of the stabilizer plate is $R(a' - w)$ and increases over the interval of w to the exterior edge of the stabilizer plate to a magnitude, M_{toe}, equal to

$$M_{toe} = R(a' - w) + V_sL + Rw$$
$$M_{toe} = Ra' - Rw + V_sL + Rw$$
$$M_{toe} = Ra' + V_sL \tag{15}$$

and is distributed linearly at a slope equal to $V_sL/w + R$.

The moment acting on the plate at the bolt group is equal to

$$M_b = Ra' + V_sL + Rg \tag{16}$$

and is distributed linearly at a slope equal to R.

***Specific Solution for Bolt Group Moment* $\mathbf{M_b = Ra}$**

Refer to Figure 11 for the following discussion.

In conventional, extended, single-plate shear connections, and in the absence of a stabilizer plate, the bolt group is designed assuming the bolt group carries a moment equal to R times the full eccentricity—that is, a moment $M_b = Ra$. If the bolt group is designed for that "full" moment (i.e., $M_b = Ra$), then substituting this into Equation 16 gives

$$M_b = Ra = Ra' + V_sL + Rg \tag{17}$$

Recognizing that $a' + g = a$, it can be deduced that the relationship shown in Equation 17 can only be true when $V_s = 0$ (recognizing that, practically, R, a', g, and L cannot be taken as zero). If $V_s = 0$, it can be deduced that the presence of the stabilizer plate has no load at the stabilizer-to-connection plate interface parallel to the connection plate, is not part of the load path, and plays no role in the transfer of the beam end reaction to the support; thus, the force distribution is no different than that of a connection with no stabilizer plate. Equally important, it also suggests that the presence of the stabilizer plate does cause the connection to impart rotational demand to the column. Figure 11 shows the force distribution through the connection when the bolt group is designed for a moment equal to $M_b = Ra$.

***Specific Solution for Bolt Group Moment* $\mathbf{M_b = Rg}$**

Refer to Figure 12 for the following discussion.

Suppose the bolt group is designed to transfer the beam end reaction from the bolt group to the toe of the stabilizer plate (i.e., a moment equal to $M_b = Rg$). Setting $M_b = Rg$ and substituting into Equation 16 gives

$$M_b = Rg = Ra' + V_sL + Rg \tag{18}$$

Upon inspection of Equation 18, it can be seen that V_s is a non-zero quantity. In other words, there is a shear force acting parallel to the plate at the stabilizer-to-connection plate interface. The shear force, V_s, can be described by rearranging Equation 18 and solving for V_s given by

$$V_s = \frac{Rg - Ra' - Rg}{L} = -\frac{Ra'}{L} \tag{19}$$

Multiplying both sides of Equation 19 by L gives

$$V_s L = -Ra' \tag{20}$$

It can be seen that, in this case, the magnitude of the moment at the toe of the stabilizer plate is zero by substituting $M_b = Rg$ into Equation 9 giving

$$M_{toe} = M_b - Rg = Rg - Rg = 0 \tag{21}$$

The change in moment from the face of the column web to the interior edge of the stabilizer plate is not affected by

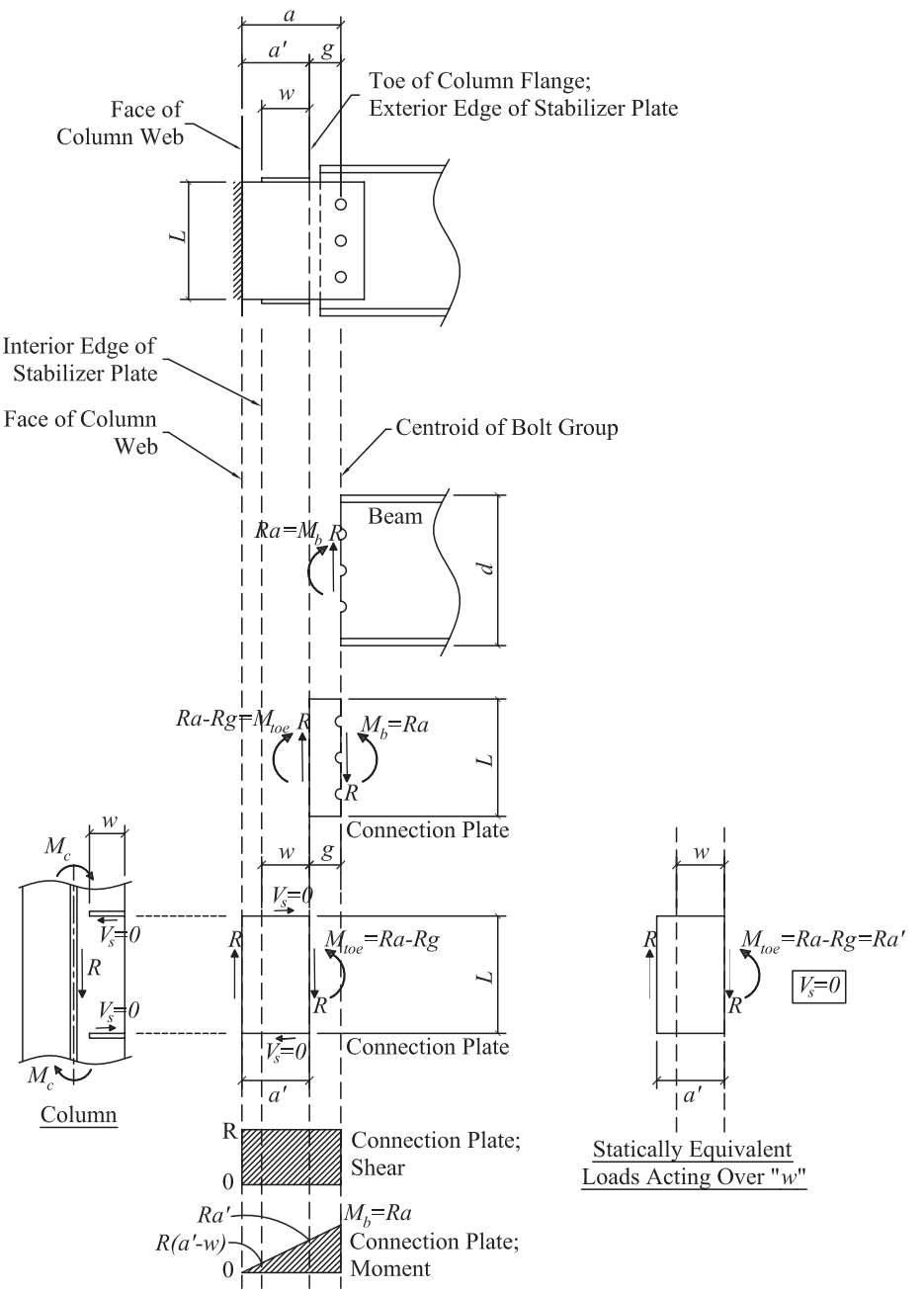

Fig. 11. Theoretical free-body diagram of connection plate with or without presence of a stabilizer plate; bolt group designed for full eccentricity, $M_b = Ra$.

the stabilizer force and is $R(a' - w)$. The change in moment from the interior edge of the stabilizer to the toe of column flange is the sum of the moments caused by the V_s force plus the area under the shear distribution. Thus, the moment at the toe of the column is

$$M_{toe} = R(a' - w) + Rw + \frac{V_s L}{w} w$$

$$M_{toe} = Ra' - Rw + Rw + V_s L \tag{22}$$

Substituting Equation 20 into Equation 22 gives

$$M_{toe} = Ra' - Rw + Rw + \frac{-Ra'}{L} L$$

$$M_{toe} = Ra' - Rw + Rw - Ra' = 0 \tag{23}$$

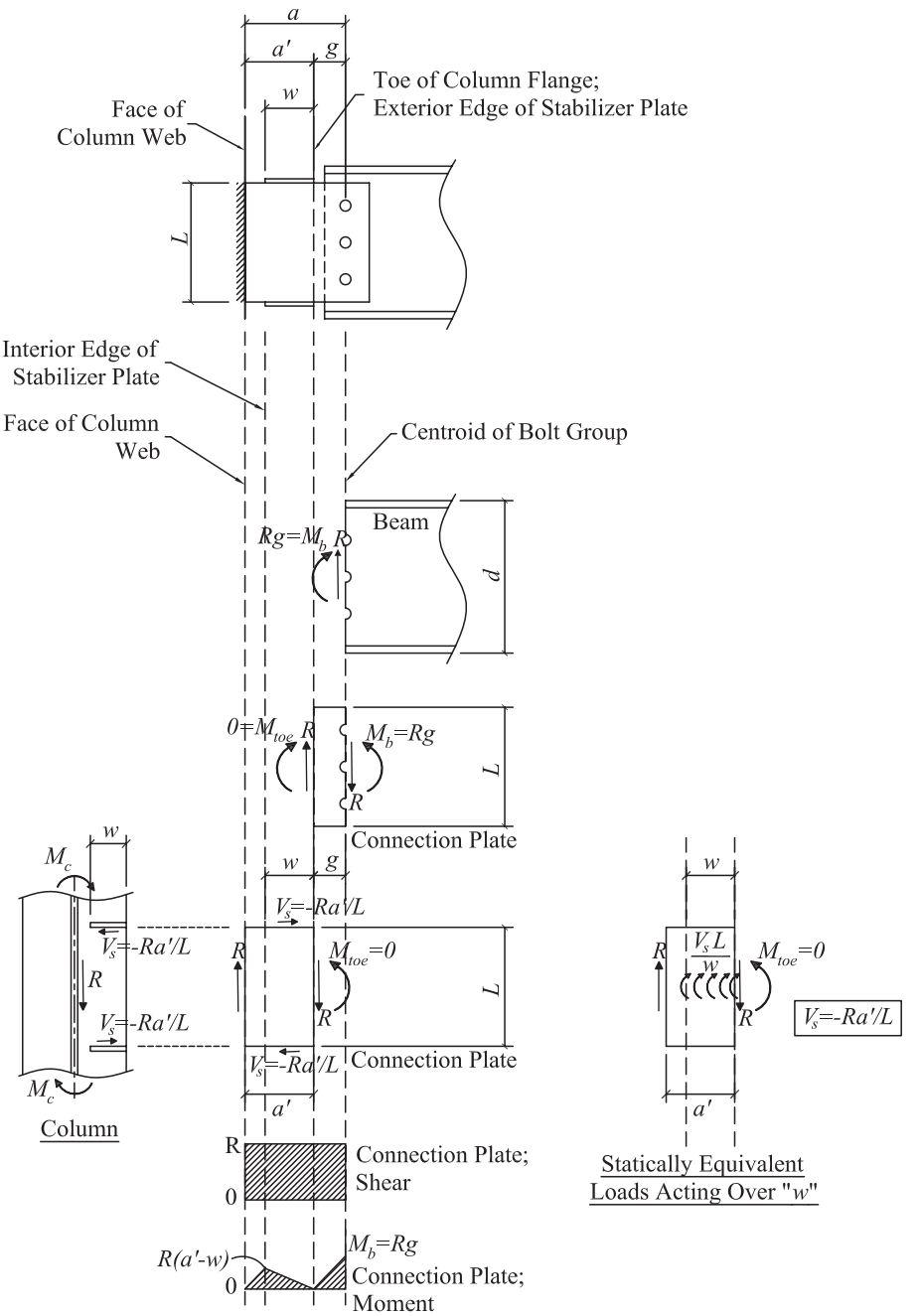

Fig. 12. Free-body diagram of connection plate in presence of a stabilizer plate; bolt group designed for eccentricity equal to g, $M_b = Rg$.

The force distribution, load path, and distribution of shear and moment when $M_b = Rg$ is shown in Figure 12. Several observations can be made when referring to Figure 12: (1) The shear demand on the connection plate is the same regardless of whether or not a stabilizer plate is present and regardless of the bolt group being designed for $M_b = Ra$ or the reduced $M_b = Rg$; (2) the moment demand on the plate is reduced when $M_b = Rg$ relative to $M_b = Ra$; and (3) because the magnitude of V_s is non-zero, a rotational demand is imparted to the column.

$M_b = Ra$ versus $M_b = Rg$

In the preceding discussion, it has been shown with statics that the presence of a stabilizer plate does not impart a rotational demand to the column if the bolt group is designed for a moment equal to $M_b = Ra$; when the bolt group is designed for a moment equal to $M_b = Rg$, a rotational demand is imparted to the column. On face value, it might be surmised that it is advantageous to design the bolt group for the full eccentricity from the bolt group to the weld line. However, we must recognize that stiffness attracts load.

Statically it seems that $V_s = 0$ when $M_b = Ra$. However, the attachment of the stabilizer plate to the connection plate—and, ultimately, connecting the stabilizer plate to the flanges of the columns—is going to produce a condition in which the stabilizer plate becomes part of the load path for transferring the beam end reaction to the column support. The weld at the stabilizer-to-connection plate will carry load (V_s not equal to zero), which will indeed impart a rotational demand to the column, M_c. The authors caution designers to carefully consider the impact on the behavior of the connection and the rotational demands on the support in the presence of a type II or type III stabilizer plate. Ultimately, the stabilizer plate will participate in the load transfer and impart a rotational demand to the column. Consequently, the authors suggest the following:

1. Only use a stabilizer plate when all other alternatives, such as changing the geometry and proportioning of the connection, have been exhausted to no avail. Stabilizer plates are rarely required in this type of connection (see Thornton and Fortney, 2011).
2. In the unlikely event that a stabilizer plate is required, recognize that the plate will play a role in load transfer. As such, the bolt group only need be designed for a moment $M_b = Rg$, and the weak axis rotational demand imparted to the column, M_c, should be accounted for when sizing the column. For typical connections, the rotational demand on the produced by the V_s force will be relatively small; however, because it is a weak axis rotational demand, it may require consideration.

Design of Type II Stabilizer Plates

In addition to the required axial strength and stiffness of the stabilizer plate, a type II stabilizer plate would have to be checked for shear and bending as shown in the shear and bending distribution presented in Figure 13. The authors recognize that the V_s force is not located directly at the center of the stabilizer plate, offset from the center by $(t_w + t_p)/2$, but, for simplicity, it is assumed to be. Shear rupture of the stabilizer plate beneath the weld of the stabilizer plate to the connection plate also needs to be checked.

The cross-sectional dimensions of a type II stabilizer plate, based on the required shear, V_s, are given in Equation 24.

$$\phi V_n = V_u = \frac{V_{su}}{2}$$

$$\phi 2\left(0.6F_y\right)A_s = V_{su}$$

$$A_s = \frac{V_{su}}{\phi 1.2F_y} \qquad \text{(LRFD)} \tag{24a}$$

$$\frac{V_n}{\Omega} = \frac{V_{sa}}{2}$$

$$\frac{0.6F_yA_s}{\Omega} = \frac{V_{sa}}{2}$$

$$A_s = \frac{\Omega V_{sa}}{1.2F_y} \qquad \text{(ASD)} \tag{24b}$$

In Equations 24a and 24b, $\phi = 1.00$ and $\Omega = 1.50$.

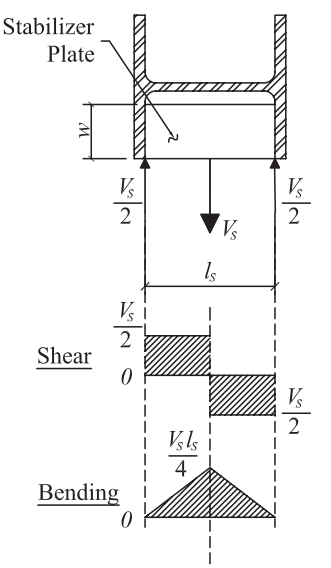

Fig. 13. Shear and bending in stabilizer plate.

The required thickness of a type II stabilizer plate, based on the required bending, $V_s l_s/4$, are given in Equation 25.

$$\phi M_n = \frac{V_{su} l_s}{4}$$

$$\phi F_y Z_s = \frac{\phi F_y t_s w^2}{4} = \frac{V_{su} l_s}{4}$$

$$\phi F_y t_s w^2 = V_{su} l_s$$

$$t_s \geq \frac{V_{su} l_s}{\phi F_y w^2} \qquad \text{(LRFD)} \qquad (25a)$$

$$\frac{M_n}{\Omega} = \frac{V_{sa} l_s}{4}$$

$$\frac{F_y Z_s}{\Omega} = \frac{F_y t_s w^2}{4\Omega} = \frac{V_{sa} l_s}{4}$$

$$\frac{F_y t_s w^2}{\Omega} = V_{sa} l_s$$

$$t_s = \frac{\Omega V_{sa} l_s}{F_y w^2} \qquad \text{(ASD)} \qquad (25b)$$

In Equations 25a and 25b, $\phi = 0.90$ and $\Omega = 1.67$.

The thickness, t_s, of the stabilizer plate based on shear rupture beneath the weld of the stabilizer plate to the connection plate is determined as follows.

$$\phi R_n = \phi(0.6F_u) w t_s = \frac{V_{su}}{2}$$

$$t_s = \frac{V_{su}}{\phi 2(0.6F_u) w} \qquad \text{(LRFD)} \qquad (26a)$$

$$\frac{R_n}{\Omega} = \frac{(0.6F_u) w t_s}{\Omega} = \frac{V_{sa}}{2}$$

$$t_s = \frac{V_{sa} \Omega_s}{2(0.6F_u) w} \qquad \text{(ASD)} \qquad (26b)$$

In Equation 26a and 26b, $\phi = 0.75$, $\Omega = 2.00$.

The weld at the stabilizer plate to the connection plate is sized for the force, V_s, and the weld at the stabilizer plate to the column flanges is sized for $V_s/2$.

Example Problem 3—Type II Stabilizer Plate

Problem Statement

Figure 14a shows a single-plate shear connection used as a beam end connection for a W30×90 framing to the web of a W12×152 column. The required shear force for the design of the connection is $R_u = 150$ kips. For the given geometry, an evaluation of the lateral torsional buckling capacity of the single-plate connection and the effect of lap eccentricity indicate that a stabilizer plate is not required. However, the engineer of record has implemented a design parameter requiring all single-sided connections to be supported with a stabilizer plate with a width approximately equal to $b_f/2 - k_1$. Additionally, the bolt group in the single-plate shear connections must be designed for a moment equal to $M_b = Ra$.

1. Demonstrate that a stabilizer plate is not required based on:
   a. Lateral torsional buckling of the plate.
   b. The effect of lap eccentricity.
2. Determine the required cross-sectional dimensions of the type II stabilizer plate, assuming $M_b = Ra$.
3. Determine fillet weld sizes required for attaching the stabilizer plate assuming $M_b = Ra$.

Assume all material is GR 50.

Solution

Part 1a

The lateral torsional buckling strength of the plate is

$$\phi R_n = \phi \frac{1{,}500\pi L t^3}{a^2}$$
$$= (0.9)\frac{(1{,}500 \text{ ksi})\pi(24 \text{ in.})(0.50 \text{ in.})^3}{(9 \text{ in.})^2}$$
$$= 157 \text{ kips} > 150 \text{ kips} \rightarrow \text{stabilizer plate not required}$$

Part 1b

The required torsional moment strength due to lap eccentricity is

$$M_{tu} = R\left(\frac{t_w + t_p}{2}\right)$$
$$= (150 \text{ kips})\left(\frac{0.47 \text{ in.} + 0.50 \text{ in.}}{2}\right)$$
$$= 72.8 \text{ kip-in.}$$

The available torsional moment strength is

$$\phi M_t = \left[\phi_v\left(0.6F_{yp}\right) - \frac{R_u}{Lt_p}\right]\left(\frac{Lt_p^2}{2}\right) + \frac{2R_u^2\left(t_w + t_p\right)b_f}{\phi_b F_{yb} L_s t_w^2}$$
$$= \left[(1.0)(0.6)(50 \text{ ksi}) - \frac{150 \text{ kips}}{(24 \text{ in.})(0.50 \text{ in.})}\right]\left(\frac{(24 \text{ in.})(0.50 \text{ in.})^2}{2}\right) + \frac{(2)(150 \text{ kips})^2(0.47 \text{ in.} + 0.50 \text{ in.})(10.4 \text{ in.})}{(0.90)(50 \text{ ksi})(28 \text{ ft})(12 \text{ in./ft})(0.47 \text{ in.})^2}$$
$$= 52.5 \text{ kip-in.} + 136 \text{ kip-in.}$$
$$= 188 \text{ kip-in.} > 72.8 \text{ kip-in.} \rightarrow \text{stabilizer plate not required}$$

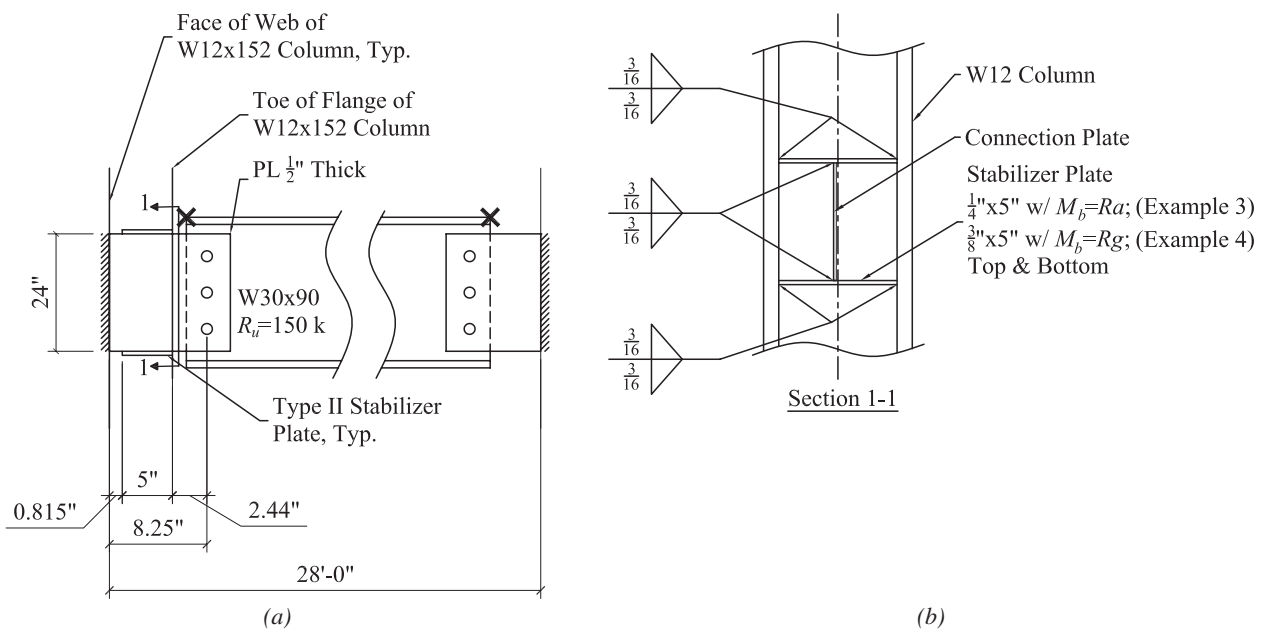

Fig. 14. Single-plate shear connection—examples 3 and 4: (a) elevation; (b) final stabilizer plate details.

Part 2

In Part 1 of this solution, it is demonstrated that a stabilizer plate is not required. However, the problem statement requires a stabilizer plate with a width of $w = (b_f/2) - k_1$ be provided regardless of the outcome of Part 1.

The width, w, of the stabilizer plate is half the flange width of the column minus k_1.

$$\begin{aligned} w &= \frac{b_f}{2} - k_1 \\ &= \frac{12.5 \text{ in.}}{2} - 1.25 \text{ in.} \\ &= 5.00 \text{ in.} \end{aligned}$$

Take $w = 5.00$ in.

Stabilizer plate size based on required axial strength using Equation 3a.

$$\begin{aligned} A_s &= \frac{0.02 R_u a}{\phi F_y L} \\ &= \frac{(0.02)(150 \text{ kips})(8.25 \text{ in.})}{(0.75)(50 \text{ ksi})(24.0 \text{ in.})} \\ &= 0.0275 \text{ in.}^2 \end{aligned}$$

Given the width of the plate is 5.0 in., the required plate thickness is

$$\begin{aligned} t_s &= \frac{0.0275 \text{ in.}^2}{5.0 \text{ in.}} \\ &= 0.006 \text{ in.} \end{aligned}$$

Stabilizer plate size based on required axial stiffness using Equation 6a.

$$\begin{aligned} l_s &= \left(d - 2t_f\right)_{column} \\ &= 13.7 \text{ in.} - (2)(1.40 \text{ in.}) \\ &= 10.9 \text{ in.} \end{aligned}$$

$$\begin{aligned} A_s &= \frac{5 R_u l_s}{\phi L E} \\ &= \frac{(5)(150 \text{ kips})(10.9 \text{ in.})}{(0.75)(24.0 \text{ in.})(29{,}000 \text{ ksi})} \\ &= 0.016 \text{ in.}^2 < 0.0275 \text{ in.}^2 \quad \rightarrow \quad \text{strength controls over stiffness} \end{aligned}$$

The required axial force in the stabilizer plate is determined using Equation 1.

$$\begin{aligned} P_{su} &= \frac{0.02 M_{bu} C_d}{L} \\ &= \frac{(0.02)(150 \text{ kips})(8.25 \text{ in.})(1.0)}{24.0 \text{ in.}} \\ &= 1.03 \text{ kips} \end{aligned}$$

To determine the transverse shear and bending on the stabilizer plate, the force V_s is required. From the previous discussion, when the bolt group is designed for a moment $M_b = Ra$, the force $V_s = 0$. To demonstrate this, the moment at the exterior edge of

the stabilizer (equal to the moment at the toe of the column flange because the stabilizer is flush with the toe, i.e., $a' + g = a$) is given by Equation 12:

$$M_{toe} = M_b - Rg = Ra - Rg = Ra'$$

$$M_{toe} = (150 \text{ kips})(8.25 \text{ in.} - 2.44 \text{ in.})$$
$$= 872 \text{ kip-in.}$$

Substituting the value for M_{toe} into Equation 13 shows that $V_s = 0$ when $M_b = Ra$.

$$V_{su} = \frac{M_{toe} - Ra'}{L}$$
$$= \frac{872 \text{ kip-in.} - (150 \text{ kips})(5.815 \text{ in.})}{24.0 \text{ in.}}$$
$$= 0$$

Because $V_s = 0$, there are no transverse loads on the stabilizer plate. Thus, transverse shear and bending of the stabilizer plate do not apply. The stabilizer and its attachments only need be based on the axial force, P_{su}.

Axial strength controls (t_s greater than 0.006 in.).

Use a ¼-in. × 5.0-in. stabilizer with 3⁄16-in. fillets welds.

Part 3

Weld at Connection Plate to Stabilizer Plate

The force to be transferred by the weld is the axial force P_s = 1.03 kips. Assuming a 5-in.-long × 3⁄16-in. fillet weld is provided on both sides of the connection plate, and on both sides of the stabilizer at the column flanges, the weld strength provided is

$$\theta = 90°$$
$$\mu = 1.0 + 0.5\sin^{1.5}(90°) = 1.50$$
$$\phi R_w = 1.392 Dl n\mu$$
$$= (1.392)(3 \text{ sixteenths})(5.0 \text{ in.})(2)(1.50)$$
$$= 62.6 \text{ kips} > 1.03 \text{ kips} \quad \textbf{OK}$$

Provide a 5-in.-long × 3⁄16-in. fillet weld on both sides of the connection plate. The final details of the stabilizer plate and welds are shown in Figure 14b.

Example Problem 4—Type II Stabilizer Plate

Problem Statement

For the connection given in Example 3, it was required that a stabilizer plate be provided and that the bolt group be designed for a moment equal to $M_b = Ra$. As discussed previously, in the presence of a stabilizer plate, attached with welds at the connection plate and the column flanges, there will be a moment imparted to the column regardless of the statics discussion supporting Equation 17. Considering that imparting a moment to the column is inevitable in the presence of a stabilizer, the cost of providing the stabilizer plates can be offset, somewhat, by reducing the moment for which the bolt group is designed ($M_b = Rg$). A force V_s not equal to zero will be present.

For the connection shown in Example 3, size the stabilizer plate and welds assuming the bolt group is designed for a moment equal to $M_b = Rg$.

1. Describe the how the approach to the design would differ from the solution given in Example 2.

2. Size the stabilizer plate and welds assuming the bolt group is designed for a moment equal to $M_b = Rg$.

3. Draw the shear and moment distribution along the span of the connection plate (from the face of the support to the centroid of the bolt group). This is a special case of Figure 12.

Solution

Part 1

The column moment, M_c, will be $V_sL/2$ or V_sL (see Figure 12), depending on whether the column is continuous or discontinuous at the connection location, respectively.

When the bolt group is designed for a moment $M_b = Ra$, statics dictates that $V_s = 0$, but the presence of the stabilizer plates will induce a non-zero statically indeterminate V_s force due to simple beam end rotation. The authors believe that it would be better to consider the V_s force and its effect on the column. A statically determinate force V_s can be calculated when the bolt group can be designed for the shear, R, and the moment, $M_b = Rg$. Because $g < a$, a more economical bolt group will result, and the effect of the stabilizer plate on the column can be easily evaluated.

Part 2

When the bolt group is designed for a moment $M_b = Rg$, the transverse force on the stabilizer is not zero. From Equation 23, when $M_b = Rg$, the moment at the exterior edge of the stabilizer (toe of the column in this example) is $M_{toe} = 0$.

From Equation 20, when $M_b = Rg$, the transverse force, V_s, is given as

$$V_s = -\frac{Ra'}{L}$$
$$= -\frac{(150 \text{ kips})(5.815 \text{ in.})}{24.0 \text{ in.}}$$
$$= -36.3 \text{ kips}$$

Stabilizer plate area based on shear yielding strength is determined using Equation 24a.

$$A_s = \frac{V_{su}}{\phi 1.2F_y}$$
$$= \frac{36.3 \text{ kips}}{(1.00)(1.2)(50 \text{ ksi})}$$
$$= 0.605 \text{ in.}^2$$

The required thickness for shear yield of the 5.0-in.-wide plate is

$$t_s = \frac{0.605 \text{ in.}^2}{5.0 \text{ in.}}$$
$$= 0.121 \text{ in.}$$

Stabilizer plate thickness based on bending strength is determined using Equation 25a.

$$t_s = \frac{V_{su}l_s}{\phi F_y w^2}$$
$$= \frac{(36.3 \text{ kips})(10.9 \text{ in.})}{(0.90)(50 \text{ ksi})(5.0 \text{ in.})^2}$$
$$= 0.352 \text{ in.}$$

Stabilizer plate thickness based on shear rupture is determined using Equation 26a.

$$t_s = \frac{V_{su}}{\phi 2(0.6F_u)w}$$
$$= \frac{36.3 \text{ kips}}{(0.75)(2)(0.6)(65 \text{ ksi})(5.0 \text{ in.})}$$
$$= 0.124 \text{ in.}$$

Bending controls the required plate size.

Provide a ⅜-in. × 5-in. stabilizer plate.

Weld at Connection Plate to Stabilizer Plate

The force to be transferred by the weld is the shear force $V_s = 36.3$ kips and $P_s = 1.03$ kips. Assuming a 5-in.-long × 3⁄16-in. fillet weld is provided on both sides of the connection plate, the weld strength provided is

$$R = \sqrt{(1.03 \text{ kips})^2 + (36.4 \text{ kips})^2}$$
$$= 36.4 \text{ kips}$$
$$\theta = \tan^{-1}\left(\frac{1.03 \text{ kips}}{36.4 \text{ kips}}\right)$$
$$= 1.62^\circ$$
$$\mu = 1.0 + 0.5\sin^{1.5}(1.62^\circ)$$
$$= 1.00$$
$$\phi R_w = 1.392Dln\mu$$
$$= (1.392)(3 \text{ sixteenths})(5 \text{ in.})(2)(1.00)$$
$$= 41.8 \text{ kips} > 36.3 \text{ kips} \qquad \textbf{OK}$$

Provide a 5-in.-long × 3⁄16-in. fillet weld on both sides of the connection plate.

Weld at Stabilizer Plate to the Column Flange

The required force to be transferred by the weld is one-half of the shear force, $V_s/2 = 36.3 \text{ kips}/2 = 18.2$ kips, and $P_s = 1.03$ kips. Assuming a 5-in.-long × 3⁄16-in. fillet weld is provided on both sides of the stabilizer plate, the weld strength provided is

$$R = \sqrt{(1.03 \text{ kips})^2 + (18.2 \text{ kips})^2}$$
$$= 18.2 \text{ kips}$$
$$\theta = \tan^{-1}\left(\frac{1.03 \text{ kips}}{18.2 \text{ kips}}\right)$$
$$= 3.24^\circ$$
$$\mu = 1.0 + 0.5\sin^{1.5}(3.24^\circ)$$
$$= 1.01$$
$$\phi R_w = 1.392Dln\mu$$
$$= (1.392)(3 \text{ sixteenths})(5 \text{ in.})(2)(1.01)$$
$$= 42.2 \text{ kips} > 18.2 \text{ kips} \qquad \textbf{OK}$$

Provide 5-in.-long × 3⁄16-in. fillet weld on both sides of the stabilizer plate.

Figure 12b shows the final details of the stabilizer plate when the bolt group is designed for a moment $M_b = Rg$.

Part 3

In this case, the bolt group is designed for a moment, M_{bu}, equal to

$$M_{bu} = R_u g$$
$$= (150 \text{ kips})(2.44 \text{ in.})$$
$$= 366 \text{ kip-in.}$$

The moment at the interior edge of the stabilizer plate, $M_{s,i}$, is

$$M_{s,iu} = R_u(a' - w)$$
$$= (150 \text{ kips})(8.815 \text{ in.} - 0.815 \text{ in.})$$
$$= 122 \text{ kip-in.}$$

The moment at the exterior edge of the stabilizer plate ($M_{toeu} = M_{s,eu}$) is $M_{s,iu}$ plus the area under the shear distribution over the interval "w" (5.0 in.) plus the moment associated with the stabilizer shear force, V_{su}, and is

$$M_{toe} = 122 \text{ kip-in.} + (150 \text{ kips})(5.0 \text{ in.}) - (36.3 \text{ kips})(24 \text{ in.})$$
$$\approx 0$$

The moment at the bolt group is

$$M_{bu} = M_{toe,u} + R_u g$$
$$= 0 + (150 \text{ kips})(2.44 \text{ in.})$$
$$= 366 \text{ kip-in.}$$

The free-body diagram and distribution along the span of the connection plate is shown in Figure 15.

Type III Stabilizer Plates

Type III stabilizer plates are not only connected to the column flanges, but also to the column web. The discussion presented for type II stabilizer plates are applicable to type III stabilizer plates as well, with the exception that the flexure in the plate can be neglected. The stabilizer plate would need to be checked for shear rupture at the connection plate-stabilizer plate and column flange-stabilizer plate interfaces for a shear equal to $V_s/2$.

The design approach given in the *Manual* Part 10 for conventional and extended single-plate shear connections does not apply in the presence of this type of stabilizer plate. Therefore, the maximum plate thickness criterion and the $(5/8)t_p$ weld criterion do not apply.

Example Problem 5—Type III Stabilizer Plate

Problem Statement

The connection given in Example 4 is used. In that example, the bolt group is designed for the combination of the required shear, R_u, and a moment equal to $M_b = Rg$. In lieu of the type II plate used in Example 4, a type III plate is required.

Describe how the approach to the design would differ from the solution given in Example 4.

Solution

For this type of stabilizer plate, the bolt group is designed for a moment equal to $M_b = Rg$. Because the type III plate is attached to the column web as well as the column flanges, shear yielding and bending due to the V_s force are not applicable. The following applicable limits states and considerations apply. Also, because the V_s force acts over the entire distance from the face of the web to the exterior edge of the stabilizer, the moment in the connection plate over that interval is zero (i.e., the connection plate is in pure shear over the interval).

1. Shear rupture of the stabilizer at the stabilizer-to-connection plate weld.

2. Axial tension due to the required P_s bracing force.

3. Presence of the type III stabilizer plate as it plays the role of a continuity plate for the moment connection(s) framing into the column flanges. The welds of the continuity plate to the column are sized based on the requirements for the moment connection(s). The load from the P_s force must be included with the moment connection requirements when determining the required continuity plate-to-column web/flanges welds.

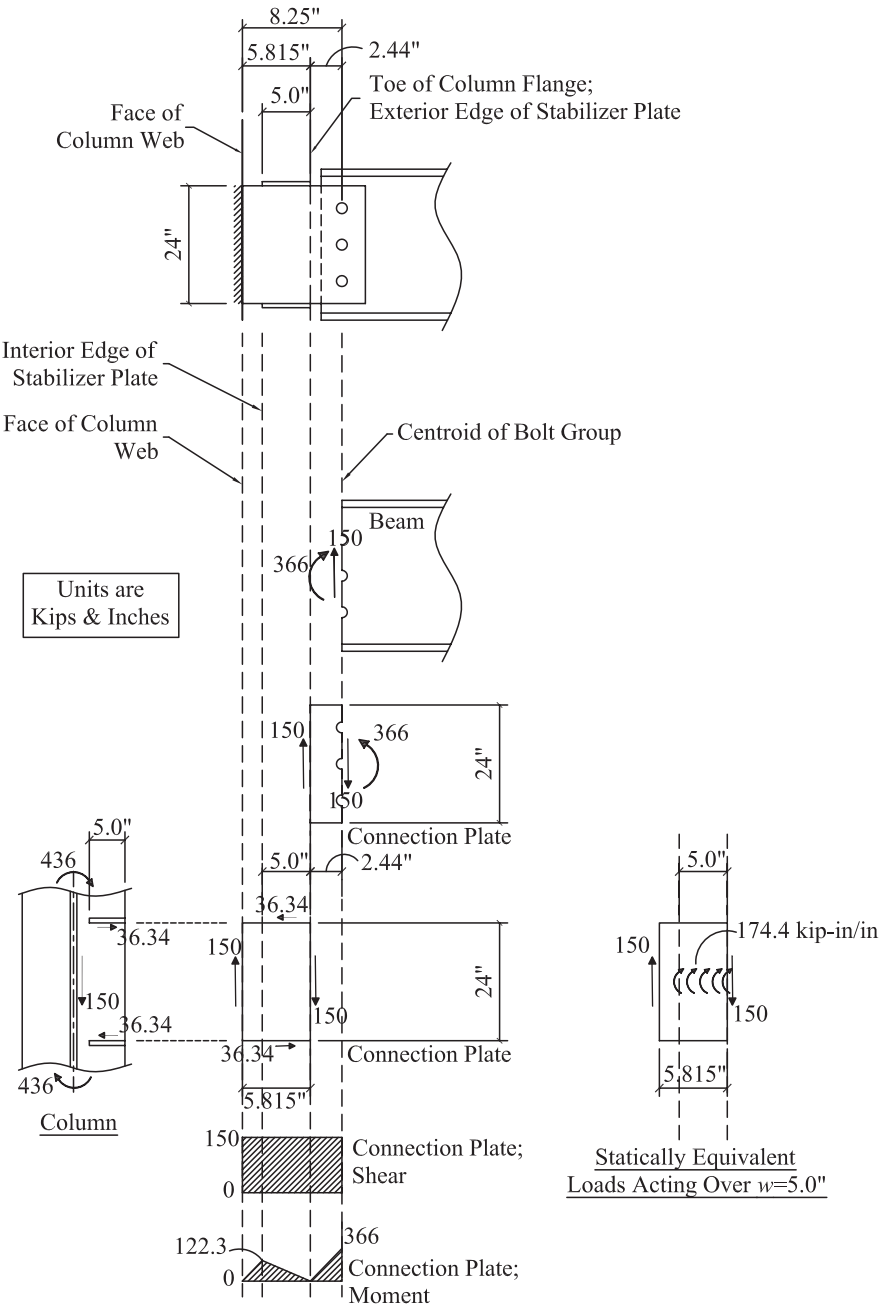

Fig. 15. Free-body diagram of force distribution for Example 4.

SUMMARY

Only after all attempts to proportion the geometry and hardware of a single-plate shear connection to have adequate lateral torsional buckling and lap eccentricity strength, without the use of a stabilizer plate, have been exhausted, can a stabilizer plate be considered as an option.

Three types of stabilizer plates are discussed in this paper: types I, II, and III. Types I and II may be used when members framing in from the perpendicular direction require only simple shear connections or moment connections with no continuity plates. The type III connection is applicable when the perpendicular member framing into the joint is a moment connection that requires continuity plates.

For each type of stabilizer plate, the analysis and design of the beam end connection, and the loads imparted on the support, need to be considered. However, one option for eliminating a need for reevaluation of the connection design and the impact on the support is to allow the stabilizer plate to "float" inside the column flanges. If this option is used, the stabilizer plate cross-section need only satisfy axial strength and stiffness requirements, in addition to bearing at the column flange and buckling on the compression half of the stabilizer plate.

The analysis of the stabilizer plate involves an evaluation of the required axial strength and stiffness assuming the stabilizer plate provides nodal bracing to the connecting plate. When the stabilizer plate is welded to the column flanges, the weld needs to be designed for the required axial force, P_s, imposed on the tension half of the stabilizer plate and the shear force, V_s, if present.

For type I stabilizer plates, it is assumed that the stabilizer plate is flexible enough such that the plate goes along for the ride during beam end rotation and that no shear or bending is imposed on the stabilizer plate. The type Ia plate is presented only for the purpose of generating a generalized analysis and design procedure. If a type I plate is desired, the type Ib plate would be more practical with regard to surviving transportation and erection. Recommendations have been made on the dimensions of the notch and attachment of the stabilizer plate to column flanges. It is recommended that the connection plate not be attached to the stabilizer plate, but rather allow simple beam end rotation by permitting the connection plate to float within the notch. This also ensures that the type Ib stabilizer plate does not become part of the load path for transferring the beam end reaction.

For type II stabilizer plates, it is assumed that the plate provides stiffness that would require an evaluation of the shear and bending imposed on the stabilizer plate. Type III stabilizer plates need only be evaluated for required axial stiffness and strength assuming the stabilizer plate has two pinned ends and two free sides. Shear and bending in a type III stabilizer plate are not applicable. However, shear rupture beneath the connected interfaces should be evaluated.

The design of the bolt group is also an important consideration. For type II stabilizer plates, if the bolt group in the beam end connection is evaluated as if the stabilizer plate is not present (i.e., design bolt group for $M_b = Ra$), statics suggest that no moment is imparted to the support. However, the stiffness provided by the weld at the stabilizer plate-to-column flange will attract load, forcing the stabilizer plate to become part of the load path and ultimately imparting rotational demand on the support. It is recommended that if a type II plate is used, and not permitted to float, the bolt group should be designed for a moment $M_b = Rg$. This reduces the moment demand on the bolt group and reduces the moment demand on the connecting plate. A moment generated by the V_s force will be imparted to the column in this condition.

When the bolt group is designed for a moment $M_b = Rg$, the moment would need to be considered when evaluating the strength of the column. Regardless of the moment considered in the bolt group, the presence of the stabilizer plate, if not permitted to float between the column flanges, alters the behavior of the connection and reduces the eccentricity on the bolt group. In this condition, the weld of the connection plate to the support can be sized based on the required shear while neglecting the ductility checks that require a minimum weld size equal to ⅝ times the thickness of the connection plate and a maximum plate thickness.

SYMBOLS

A_s	Gross cross-sectional area of stabilizer plate
E	Young's modulus (29,000 ksi)
F_y	Nominal specified yield strength
F_u	Nominal specified tensile strength
L	Length of single-plate connection (vertical dimension)
M_b	Moment in bolt group
M_b	Moment in single-plate shear connection
M_c	Moment imparted to column by stabilizer plate force, V_s
M_n	Nominal moment strength
$M_{s,i}$	Moment in connection plate at the interior edge of the stabilizer plate
M_{toe}	Moment in connection plate at toe of column flange when exterior edge of stabilizer plate is aligned with toe of column flange ($M_{s,e} = M_{toe}$ in this condition)
P_s	Nominal required axial force in stabilizer plate
R	Required shear strength; R_a for ASD; R_u for LRFD

R_n Nominal shear strength

R_w Nominal weld strength

a Distance from face of support to centroid of the bolt group

a' Distance from face of support to exterior edge of stabilizer plate

d Depth of beam

g Distance from centroid of bolt group to exterior edge of stabilizer plate

h_n Height of notch in a type Ib stabilizer plate

h_p Vertical dimension on contact area between connection plate and stabilizer in a type Ib stabilizer plate

l_s Length of stabilizer plate

t_f Thickness of beam or column flange

t_p Thickness of connection plate

t_s Thickness of stabilizer plate

w Width of stabilizer plate

w_n Width of notch in a type Ib stabilizer plate

Ω ASD strength reduction factor

β_s Nominal required stabilizer plate stiffness

ϕ LRFD strength reduction factor

REFERENCES

AISC (2010), *Specification for Structural Steel Buildings*, ANSI/AISC 360-10, American Institute of Steel Construction, Chicago, IL.

AISC (2011), *Steel Construction Manual*, 14th ed., American Institute of Steel Construction, Chicago, IL.

Thornton, W.A., and Fortney, P.J. (2011), "On the Need for Stiffeners for and the Effect of Lap Eccentricity on Extended Shear Tabs," *Engineering Journal*, AISC Vol. 48, No. 2, pp. 117–125.

Connection Design Recommendations for Improved BRBF Performance

KEITH D. PALMER, CHARLES W. ROEDER and DAWN E. LEHMAN

ABSTRACT

Numerous component tests on buckling-restrained braces (BRBs) have demonstrated their approximately symmetric tension and compressive capacities, stable cyclic behavior and large (component) ductility prior to core fracture. These properties make them suitable ductile fuses for seismic design. Experiments on buckling-restrained braced frame (BRBF) systems show that the inelastic axial deformation capacity of BRBs may be compromised by system performance demands. Damage including significant yielding, local buckling, twisting and fracture of the beams and columns, tearing of the gusset plate welds to framing members, and out-of-plane movement of the BRB have been observed in BRBF tests. Prior test results are reviewed, and an analytical study using high-resolution models, which were validated with prior test results, is used to develop mitigation strategies for the damage. Design recommendations to mitigate damage and improve system performance are developed. The study reveals that damage to the beams and columns at a corner gusset-plate connection is related to the ratio of the component web thickness to the gusset plate thickness, suggesting a modest design change that will significantly improve BRBF performance.

Keywords: buckling-restrained braced frames, ductile fuse, gusset-plate connection, core fracture.

INTRODUCTION

Buckling-restrained braced frames (BRBFs) are concentrically braced frames (CBFs) that utilize buckling-restrained braces (BRBs) to provide stiffness, strength and energy dissipation during an earthquake. Developed in Japan in the 1970s, BRBs are proprietary members that have become increasingly popular in the United States. As the name implies, a BRB prevents the brace from buckling in compression and, therefore, provides nearly symmetric force-displacement behavior in tension and compression. This results in superior energy dissipation capacity for the BRB component relative to a conventional buckling brace. A BRB consists of a steel core, which resists the axial load demands, and is placed inside a steel tube filled with a cementitious material to prevent buckling. Additional material is placed between the steel core and the cementitious fill to debond the steel core from the filled tube restrainer and limit transfer of axial load to the tube (Figure 1).

Keith D. Palmer, Structural Engineer, Simpson Gumpertz & Heger Inc., San Francisco, CA. E-mail: kdpalmer@sgh.com

Charles W. Roeder, Professor, Department of Civil and Environmental Engineering, University of Washington, Seattle, WA (corresponding). Email: croeder@u.washington.edu

Dawn E. Lehman, Associate Professor, Department of Civil and Environmental Engineering, University of Washington, Seattle, WA

Paper No. 2014-08R

The primary difference in design for different BRBFs lies in the connections as shown in Figure 2. Figure 2a shows a bolted connection of the cruciform shape of the BRB outside of the restraining tube for one BRB type. Figure 2b shows a clevis that is welded to an end plate, which in turn is welded to the BRB core and used to connect the BRB to the gusset plate. The pinholes in the gusset plate and clevis are reinforced to prevent a bearing failure, and this brace-to-gusset connection approaches a true pin about an axis perpendicular to the plane of the frame. In most cases, the beam is continuous between the faces of the two columns, but some BRBF connections have a beam moment release adjacent to the gusset as shown in Figure 2b to limit potential damage in the connection region. The connection of Figure 2c has a plate welded to the core end plate that is slotted to fit over the gusset plate and is welded to the gusset plate on four sides. Some connections have a collar that wraps around the BRB restrainer to add stability to the core extension beyond the filled steel casing, as shown in Figures 2b and 2c.

The design and testing of BRBs in the United States is governed by the AISC *Seismic Provisions* (AISC, 2010). These provisions focus on the tensile and compressive inelastic deformations of the BRBF under the design earthquake. The BRB must be designed, tested and detailed to accommodate expected deformations associated with a story drift of at least 2% of the story height or two times the design story drift, whichever is larger, in addition to the brace deformations associated with frame deflection due to gravity loading. BRBs must pass qualifying cyclic brace component and subassemblage tests as specified in Section K3 of the *Seismic Provisions*. The component test consists

of cyclic uniaxial loading, but the subassemblage test also simulates connection rotational demands on the BRB caused by frame action. The BRB must achieve a cumulative inelastic deformation capacity of 200 times the yield deformation or greater in the component test.

Recent experiments on BRBF systems suggest that the BRB may reach its expected strength and deformation capacity, but the *system* deformation capacity may be limited by damage to other components or by unintended system response mechanisms (Palmer et al., 2014). As a consequence, the BRBF system performance is often more complex than suggested by current design methods.

SUMMARY OF PRIOR RESEARCH RESULTS

Experimental Research

Numerous component tests (e.g., Black et al., 2004; Merritt et al., 2003; Romero et al., 2007) have been performed on BRBs in the United States, and these tests demonstrate the ability of the BRB component to achieve ductility and cumulative inelastic deformation greater than demands expected during the design basis and the maximum considered earthquakes.

Uriz (2005) tested three large-scale, partial, two-story, one-bay, planar BRBFs, and Christopolus (2005) tested five full-scale, single-story, one-bay, planar BRBFs. The BRB ductility values achieved during these tests ranged between 14 and 22, which are comparable to those achieved in BRB component tests. Additionally, the cumulative ductility values achieved in these BRBF experiments exceeded the minimum value of 200 required by the *Seismic Provisions* for BRB component tests. However, significant column and/or beam yielding and local buckling and tearing of flanges, welds and gusset plates occurred in these tests such as illustrated in Figure 3a. In many cases, out-of-plane rotation of and plastic hinge formation in the BRB core plate outside of the restrainer occurred at story drift ratios less than 2.5% as illustrated in Figure 3b. This plastic hinge formation was likely a consequence of a combination of frame yielding and deformation and the stiffness of the gusset plate and unrestrained BRB core.

Fahnestock et al., (2007) tested a 0.6-scale, four-story, planar, one-bay BRBF, in which the frame beam fixity was released at the gusset plate connections through a web-only connection similar to that shown in Figure 2b. The maximum ductility achieved by the BRBs ranged between 18 and 26, and the cumulative ductility ranged between 388 and 453, which are much larger than the 200 required by the *Seismic Provisions*. No undesirable behaviors were observed during the experiment prior to BRB fracture, and this may be at least partially attributed to the beam-moment release connection detail (see Figure 2b).

A large-scale, two-story, one-bay by one-bay, three-dimensional BRBF was tested (Palmer, 2012). The BRBs were placed in two orthogonal bays, with a single BRB in

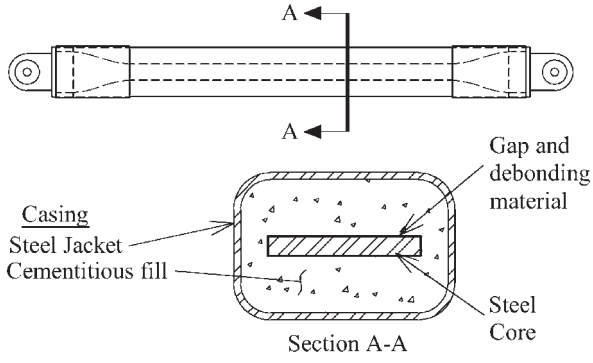

Fig. 1. Typical design of BRB.

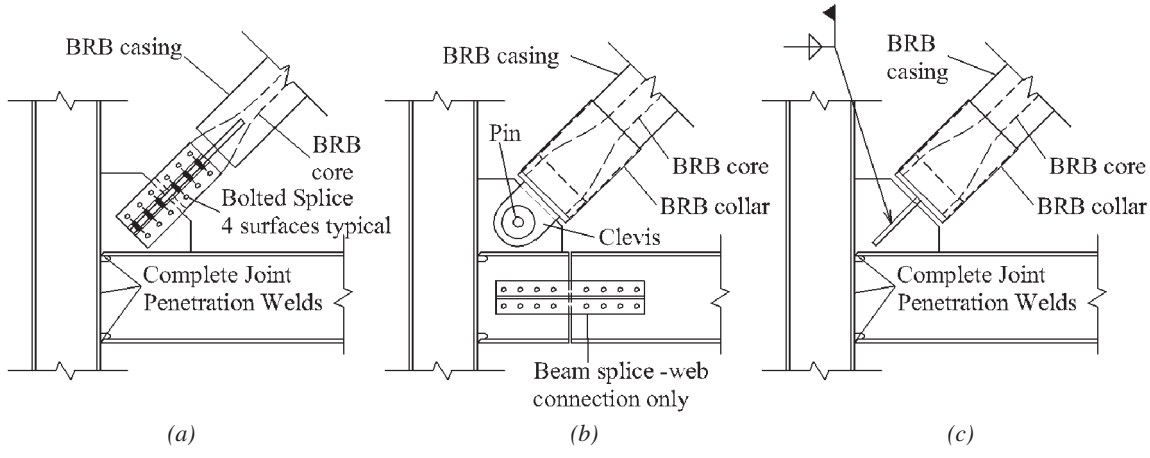

Fig. 2. BRB connection types: (a) bolted BRB, fixed beam; (b) pinned BRB, pinned beam; (c) welded BRB, fixed beam.

each story (Figure 4a); the remaining bays were designed and detailed as gravity frames. The floor system consisted of intermediate beams and composite slab on metal deck on the first level, to simulate the strength and stiffness of the floor system, and a reinforced concrete slab on the second level, to also transfer loads to the frame from the actuators. A bi-directional, cyclically increasing displacement history was applied to the top floor of the system. In the braced bays, the beam flanges and webs were attached to the columns with complete-joint-penetration (CJP) welds. The gusset plates were attached to the beams and columns with fillet welds sized according to the uniform force method (with interface moments included) and the *Seismic Provisions* (AISC, 2005, 2010) using overstrength factors corresponding to 3% story drift. The welds were performed by AISC-certified welders and visually inspected afterward. The beams and columns were checked to ensure that they passed the web crippling and web yielding checks. The dimensions and member sizes of the south frame (frame 1) are shown in Figure 4b. Additional information may be found elsewhere (Palmer, 2012).

Significant BRBF damage concentrated adjacent to the beam-column-gusset plate connections was observed (Palmer et al., 2014), and very little damage was observed at joints without gusset plates. Tearing of the gusset plate–column interface welds occurred when the brace was in compression, and these tears propagated the total length of the weld in three locations by story drifts ranging between 2.3 and 2.9%, as illustrated in Figure 3c. The BRBs were still performing well after these tears, and no other negative behaviors were observed due to these tears. Local flange and web buckling occurred at the base of two braced frame columns and in the beams adjacent to the gusset plate corner connections at approximately 2.5% story drift. Extensive beam flange and web tearing and fracture occurred at approximately 3.5% story drift. Column flange and web tearing also occurred in one location (second floor in the right

(a) *(b)* *(c)* *(d)*

Fig. 3. Damage noted in prior BRBF test results: (a) yielding of beams and columns; (b) out-of-plane movement of BRB; (c) gusset weld fracture; (d) fracture through column flange and web.

column in Figure 4b) and initiated in the column k-region at the CJP weld connecting the braced frame beam bottom flange to the column as shown in Figure 3d. The bolts in the column web are for the transverse gravity beam connection. The second-story BRBs fractured at 4.2 and 3.6% story drift in frames 1 (in foreground) and B (on right), respectively.

Analytical Research

Accurate simulation of BRBFs cannot be accomplished with simple line-element modeling because these models do not capture the complex nonlinear interaction among BRBs, other framing members and their connections. Most researchers have used continuum models, which simulate nonlinear performance but have limitations in modeling tearing and fracture of welds or steel. Fracture due to ultra-low-cycle fatigue occurs after a relatively small number of cycles at large inelastic strains, and therefore, both cyclic and maximum strain indices have been considered by researchers to implicitly predict fracture or tearing (Palmer, 2012).

Wigle and Fahnestock (2010) used ABAQUS to simulate the BRBF tested by Fahnestock et al., (2007). The third story of the test frame, including the BRB, was modeled with shell elements. The BRB casing was modeled using a flexurally stiff and axially flexible line element for the casing element that was connected to the nodes of the BRB core shell element. This approach prevented buckling of the core and minimized the axial load in the restrainer. The beams and columns in the lower two stories of the frame were modeled using line beam-column elements with lumped plastic hinges at the ends, and the BRBs were modeled as nonlinear axial springs. The simulated BRB response matched the global experimental response for the drift ranges simulated. The model was used to study the effect of bolted, pinned and welded BRB end connections; fully restrained and moment release beam end conditions; and gusset plate thicknesses [0.25 and 1.0 in. (6.35 and 25.4 mm)]. The results indicated that the type of BRB-to-gusset plate connection did not significantly affect the force-deformation behavior or local strain demands in the gusset plate connection region. Thicker gusset plates induced larger plastic strain demands at the interface of the gusset plate with the beams and columns but did not affect the global response.

This brief summary of prior research shows that the excellent component behavior measured for BRBs does not necessarily translate to equivalent system behavior. BRBF system performance often fell short of the expected performance based on the component results. Experiments on BRBF systems can be used to evaluate mechanisms to improve the system response, but experiments are too costly for evaluation of all critical parameters. Therefore, this paper describes the use of robust, high-resolution numerical simulation for this purpose.

FE MODELING APPROACH

The ABAQUS analysis platform (ABAQUS, 2010) was used to accurately simulate the global and local responses of the BRBF test specimen shown in Figure 4 and summarized

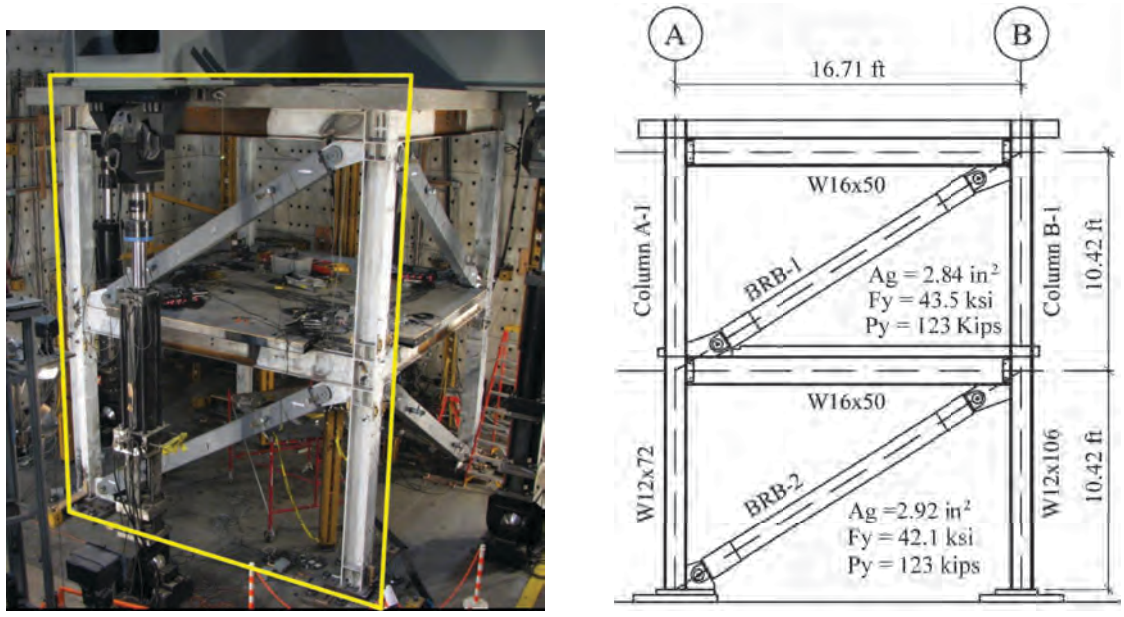

(a) *(b)*

Fig. 4. BRBF used for finite element simulations: (a) experimental frame; (b) frame elevation (Palmer, 2012).

earlier (Palmer, 2012). Variations on that basic model were then made to study selected parameters. The test specimen had two orthogonal and adjacent braced bays, but the ABAQUS model simulated only one planar braced frame as highlighted in the foreground in Figure 4a and shown schematically in Figure 4b.

Beams, columns, slabs and connections were modeled using three- and four-node quadrilateral shell elements as shown in Figure 5. The shell elements had six degrees of freedom per node. First-order (linear-interpolation) elements with reduced integration and hourglass control were used to reduce runtime and prevent locking and zero-energy deformation modes. Transverse shear stiffness was included in the formulation of the shell sections, which had five layers through the thickness and were numerically integrated during the analysis to calculate cross-sectional behavior.

The BRBs were modeled using nonlinear truss elements because of the complications and computational expense involved in modeling the core, end collars, steel tube restrainer, infill grout, contact and friction between these elements, and higher-mode core buckling. Greater modeling accuracy, using shell elements for the BRB and a line-element casing model following Wigle and Fahnestock (2010), was deemed unnecessary in this study as BRB performance was secondary to frame behavior caused by BRB forces. The truss element was calibrated to measured BRB behavior and provides accurate simulation of the local and global performance of the BRBF system.

The base of each column was fully restrained in the three orthogonal directions as shown in Figure 5. Out-of-plane restraint was provided to the braced frame beams at midspan where transverse floor beams framed into them in the

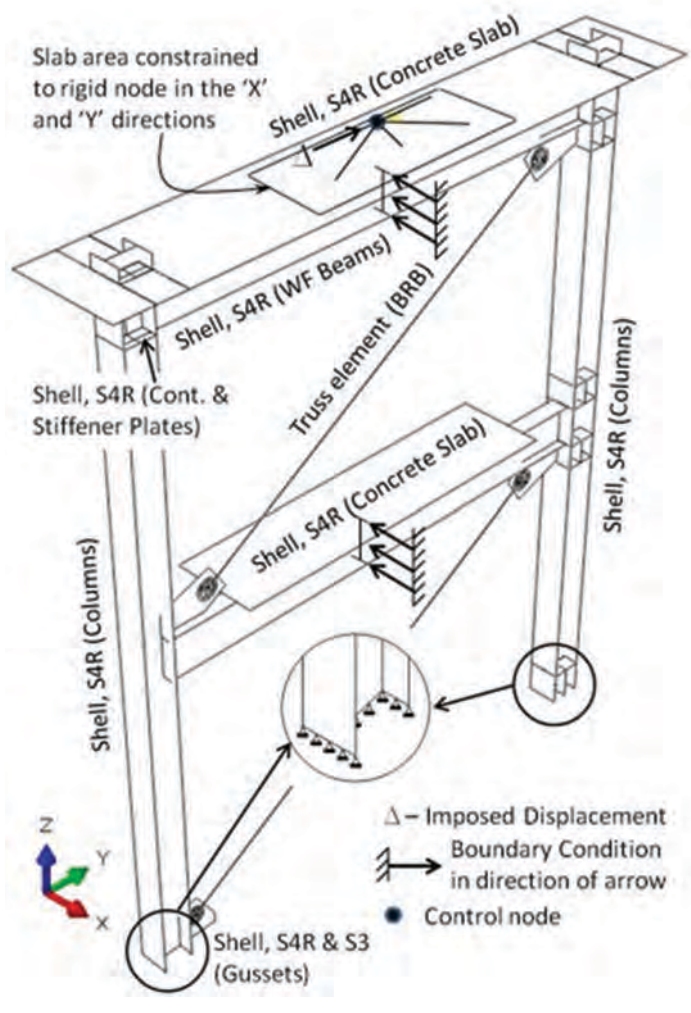

Fig. 5. BRBF finite element model with element types and boundary conditions (see Figure 3b for component sizes and frame dimensions).

Table 1. Material Yield Strengths from 3D BRBF Experiment (Palmer, 2012)		
	Measured Properties	
Shape	F_y ksi (MPa)	F_u ksi (MPa)
W12×106	55.5 (386)	73.4 (510)
W12×72	56.5 (393)	72.4 (503)
W12×45	56.5 (393)	71.4 (496)
W16×50	52.5 (365)	68.5 (476)
W16×31	54.5 (379)	68.5 (476)
W14×22	54.5 (379)	67.5 (469)
BRB-1 core	43.0 (299)	62.7 (436)
BRB-2 core	41.7 (290)	64.5 (448)

test frame. In the laboratory, the displacement history was applied to the test specimen through a large, strong, and stiff crosshead attached to the floor slab. In the analysis, a rigid control node was used to apply the displacement history of the frame (shown at the top of the frame in Figure 5). The movement of the third floor slab was constrained to the movement of this control node. The concrete slabs were simulated with shell elements, which were linked to the shell elements of the steel beam to develop composite action. Kinematic coupling constraint tied the top floor slab degrees of freedom in the area outlined in the figure to the control node. The width of the concrete slab was defined by the effective width design rules of the *Seismic Provisions*. The cyclic displacement history for the test frame was bi-directional, and the specific deformations applied to the simulation at the control node of frame 1 are shown in Figure 6.

Geometric nonlinearities were included in the analyses using the updated Lagrangian approach to capture local (and global if it occurs) buckling of the beams, columns and gusset plates. In this approach, the element stiffness is formulated at each step using the nodal coordinates in the current, deformed configuration.

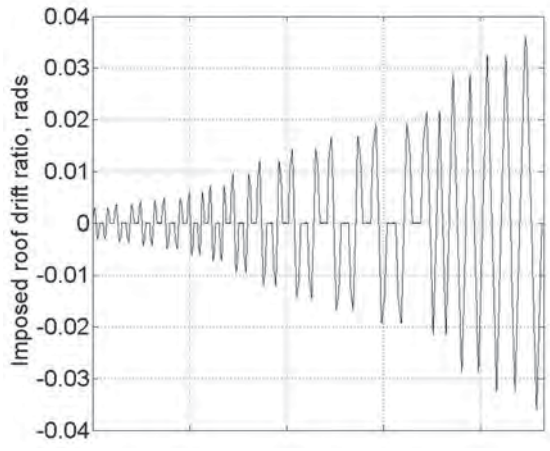

Fig. 6. Imposed cyclic displacement protocol in experiment (Palmer, 2012) and finite element simulation.

The concrete was modeled using a linear, elastic constitutive model because minimal cracking and crushing were observed during the testing. The steel yield strengths were obtained from mill test certificates and test coupons (see Table 1), while the concrete strength and elastic modulus was obtained from cylinder tests. Twenty-eight-day compressive 4×8 cylinder strengths of 6 and 8 ksi (42 and 55 Mpa) were measured for the second and third floor slabs, respectively. Steel material nonlinearities were simulated using the von Mises yield criterion with an associative flow rule and a combined, nonlinear kinematic and isotropic hardening law.

A mesh refinement study was performed to balance convergence and accuracy with minimizing the run time. Four models with different mesh densities were analyzed, and the average element sizes in the connection region ranged between 0.5 and 2.0 in. (12.7 and 50.8 mm). The results indicated that a mesh size of 1 in. (25.4 mm) was needed in the connection regions. A 2-in. (50.8-mm) mesh size was used in regions away from the connection regions (Palmer, 2012). The connection regions are defined as the area in the beams and columns that extend approximately three times the depth of the beam in each direction from the intersection of the column and beam centerlines.

Fracture is not simulated directly by the ABAQUS computer program. El-Tawil et al., (2000) and Kanvinde and Deierlein (2006) showed that tearing and fracture can be predicted using FEA and a micromechanics-based approach. That approach uses the strain at ductile fracture initiation according to Hancock and Mackenzie (1976), which is a function of a material constant and the stress triaxiality ratio. This strain is then divided by the cumulative equivalent plastic strain (PEEQ) multiplied by

the material constant needed to define a rupture index. This rupture index is used as an indicator of the susceptibility of the material to fracture. Studies confirm the accuracy of this approach (e.g., Chao et al., 2006), but this method requires very small, eight-noded brick elements with dimensions on the order of the characteristic length of the material [0.1 in. (0.3 mm) for structural steel], which results in a large computational expense.

Yoo (2006) investigated and validated the use of strain indices in shell element models for predicting initial gusset plate weld tearing as part of a prior study on special concentrically braced frames (SCBFs). Two indices were investigated: the equivalent plastic strain (PE) and the PEEQ. The simulation results of concentrically braced frame (CBF) systems experiments indicated a strong correlation between the PE with the first instance of observed tearing in the hollow structural section (HSS) braces and gusset plate, and this approach was used in this study.

MODEL VALIDATION

The model was validated using three categories of metrics: (1) global response, (2) observed damage modes and (3) local deformation measures.

Global response depends on accurate simulation of the BRB. BRB response is not completely symmetric because the compression overstrength and isotropic hardening vary with axial strain and history. However, a truss element with the von Mises yield criterion provides symmetric behavior. As a result, the BRB truss element was calibrated to (1) reach the average of the maximum tension and compression strengths, (2) match the initial yield load, (3) match the total energy dissipated and (4) match the residual load at zero displacement.

The simulated and measured force-displacement responses of the second-story BRB at four different story drift levels are shown in Figure 7a. At small story drifts, the elastic and inelastic behavior is accurately captured. At large inelastic deformations, the simulated tensile resistance and hardening slope are larger than the measured slope, while the compressive resistance and hardening slope are underestimated. However, the ultimate objective of the analytical study was to provide relative comparisons between different connection designs. Relative differences among the models are independent of the BRB material model (Palmer, 2012); therefore, this approximate simulation of the strength was deemed appropriate.

Figure 7b shows the total base shear as a function of the average story drift of the top of the frame. There is excellent agreement between the measured experimental results and the simulation. Fracture was not simulated, and therefore, the loss in strength resulting from BRB fracture is not captured in the FE model.

Figures 7c and 7d compare the experimental and simulated third-floor beam deformation within the gusset plate connection region at approximately 3.5% story drift. The figures show excellent agreement of the local flange buckling and out-of-plane web deformation at this location. Similarly, excellent agreement is observed in the simulated and tested models at the base of column A-1, as shown in Figures 7e and 7f. This buckling mode occurred at the base and not at the elevated gusset plate. The difference in the buckling modes at these two locations results from the difference in the boundary conditions. These comparisons show that the ABAQUS model provides accurate local and global simulation of the true BRBF behavior.

PARAMETRIC STUDY OVERVIEW

After verification of the accuracy of the basic model, that model was expanded to investigate salient parameters that affect the BRBF response and to evaluate potential improvements to BRBF design. Approximately 50 different models were analyzed to study the effects of:

1. Gusset plate thickness.
2. Gusset plate taper.
3. Gusset plate edge reinforcement.
4. Beam reinforcement at the joint, including web doubler plates (see Fig. 8) and flange stiffeners.
5. Column size and reinforcement at the joint, including web doubler plates (see Fig. 8) and continuity plates.
6. Beam fixity at joint region.
7. Variations in modeling the interface weld connecting the gusset plate to the beams and columns.
8. Strength and stiffness of BRB.

The reference model for the parameter study was the three-dimensional test frame model described earlier. All other analyses had well-defined variations from the reference model to evaluate the parameter in question. Comparisons and evaluations were based upon three performance metrics.

1. *Global force-displacement and local moment-displacement relationships* were compared to establish relative stiffness, resistance and initiation of strength degradation for a given model. Early strength degradation clearly represents substandard performance.
2. *The computed von Mises stress distributions and deformed shapes* were compared in critical regions (including gusset plates, beams and columns adjacent to the gusset) to identify potential locations of concern (see Figures 7d and 7f for an example).

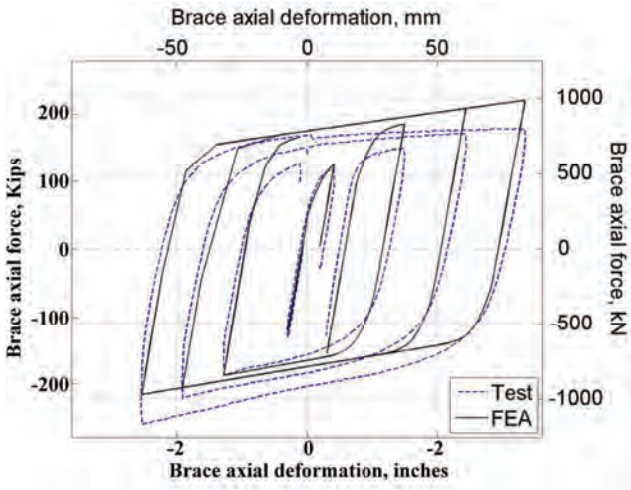

(a)

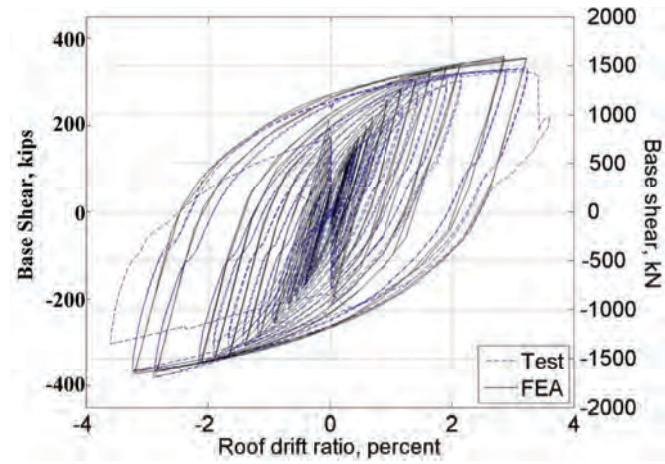

(b)

(c)

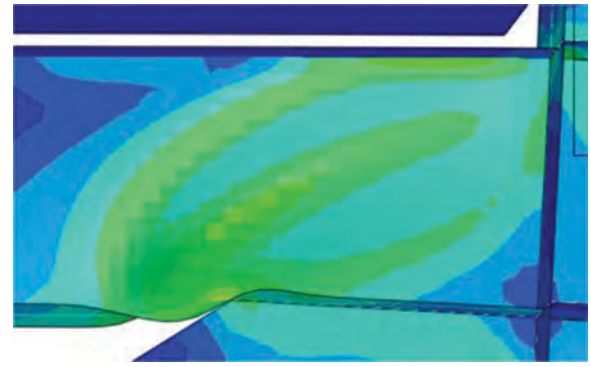

(d)

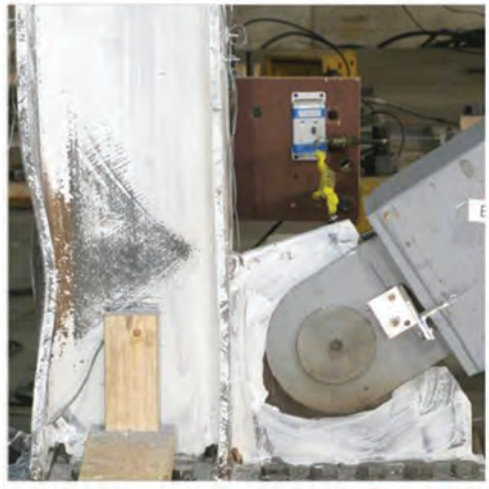

(e)

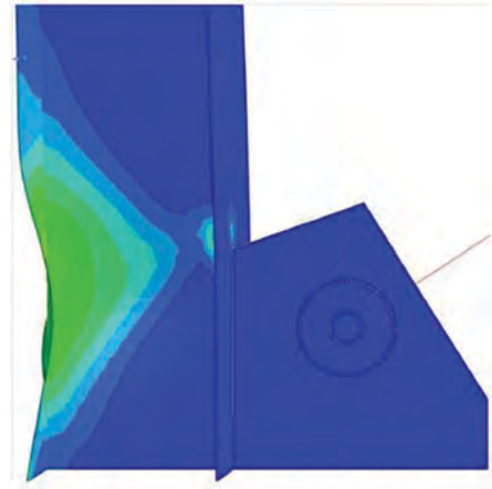

(f)

Fig. 7. Reference model validation: (a) BRB force-deformation response; (b) global base shear-story drift response; (c) observed beam yielding and local buckling; (d) simulated beam yielding and local buckling: (e) observed column yielding and local buckling; (f) simulated column yielding and local buckling.

3. *Local strains along the gusset plate interfaces with the beams and columns* were compared to identify weld yielding and potential crack initiation or fracture. The PE and PEEQ values were compared as approximate indicators of potential crack initiation and fracture (Yoo, 2009).

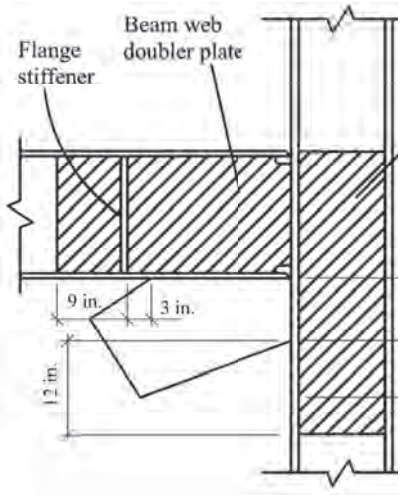

Fig. 8. Finite element model details: beam and column reinforcement.

These performance indices were evaluated at story drift levels of 2 and 3.5% because these drift levels approximate the design basis and the maximum considered earthquake demands, respectively (Chen et al., 2008). The stresses and strains sampled in the beams and columns at gusset plate interfaces were the average of the two elements simulating fillet welds on either side of the gusset plate. The gusset plate stresses and strains were sampled from single elements that occurred at the interface, as shown in Figure 9a. Typical plots of the PEEQ as a function of distance along the edge of the gusset from the intersection of the beam and column flanges (corner of the gusset) are illustrated in Figure 9b, and maximum PEEQ values in the beam, column and the edges of the gusset plate at 2% story drift are listed in Table 2. The table also lists the peak base shear and peak moment at the top of the right column in the second story. The maximum PEEQ invariably occurred at locations shown in Figure 9b.

ANALYSIS RESULTS

The initial stiffness values of all models were within 5% of each other; this is logical because the BRB provides the main contribution to elastic stiffness. The columns (W12×106 and W12×72) used in the test frame were larger than required by current seismic provisions (due to multiple tests performed on the frame), so smaller permissible columns (W12×50)

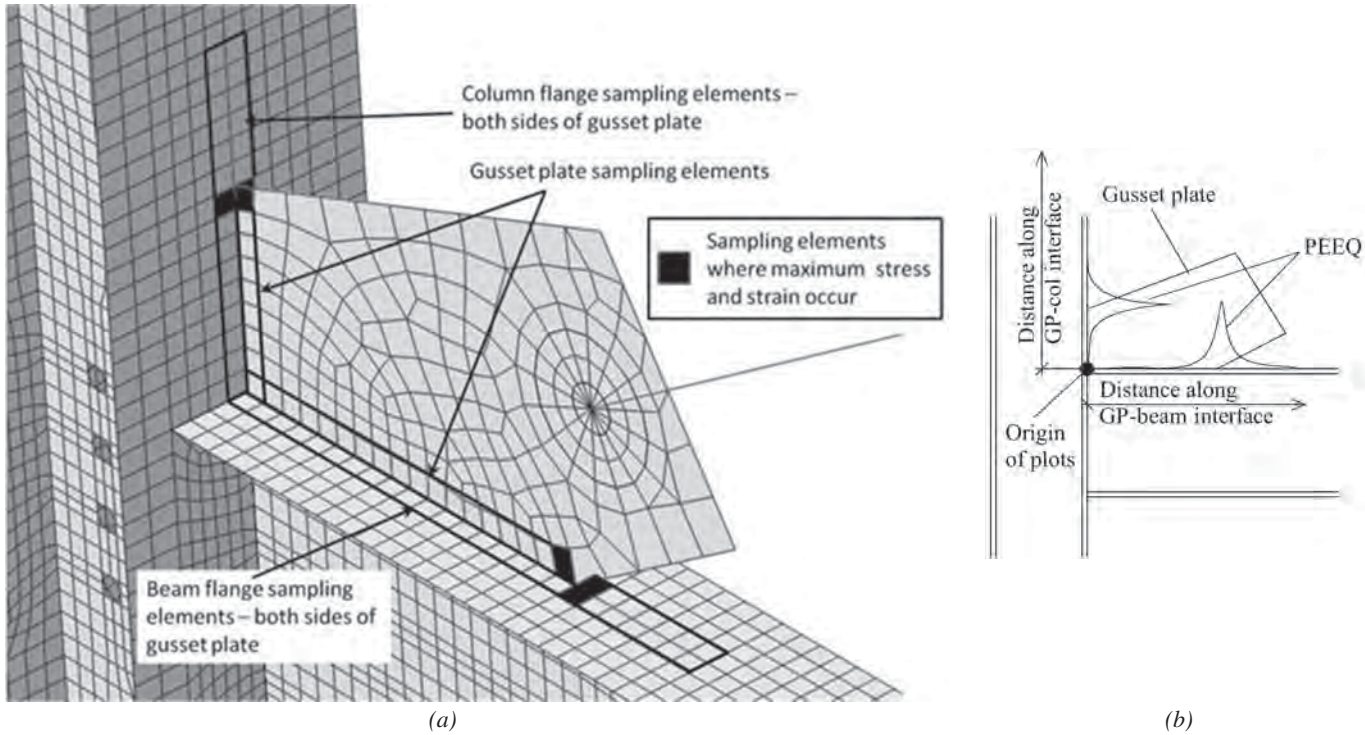

(a) *(b)*

Fig. 9. Finite element simulation performance indicator sampling regions: (a) elements sampled within connection region; (b) schematic description of plots used in comparisons.

were investigated along with potential reinforcement to critical areas of the smaller columns. The peak base shears were similar for all models with the same columns, but models with the smaller columns developed a base shear force that was 9 to 15% less than the reference model. The smaller column resisted approximately half the shear of the larger column in the reference model.

Reinforcement of Beam and Column Webs

While some columns were larger than required in the three-dimensional test specimen, significant damage was noted in nearly all beams and columns adjacent to gusset plates in test frames. This raises logical questions as to how the specimen would have performed if the minimum permissible column were employed and how damage can be reduced in the beam and column locations without excessively increasing beam and column sizes. Figure 10 plots the envelope of the cyclic moment-story drift response, where the moment is measured at the top of the column of the second story for four different models. The analysis shows that the reference model (test specimen) provided somewhat larger base shear resistance than the model with weaker columns because of the larger column shear resistance provided as noted earlier. The figure also shows that deterioration in resistance occurred with both the reference model and the reduced column model due to the inelastic damage in the beam and column, which included local buckling, but the deterioration and damage were significantly greater with the smaller column. The figure shows that the addition of web reinforcement (a doubler plate to the column web to create a column web thickness of 75% of the gusset plate thickness) eliminated the deterioration of resistance and reduced column damage for both the reference column and the smaller column specimen. While

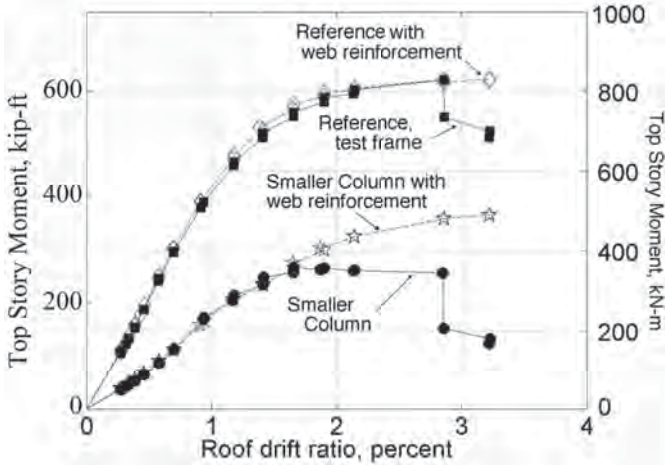

Fig. 10. Moment-story drift backbone at top of second-story column.

the addition of column web reinforcement reduced damage to the column, it invariably increased damage to the beam unless comparable measures were taken for the beam web.

Comparison of analytical results in Figure 11 amplifies these observations and also shows the effect of local damage to the beam. Figure 11a shows the extensive damage to the beam and lesser damage to the column for the reference specimen at 3.5% story drift for one connection in the frame. It must be emphasized that the ABAQUS model does not directly include cracking, tearing or fracture, and prior discussion has demonstrated extensive cracking and fractures in beams, columns and gussets at deformations well below this level. Figure 11c shows the increased damage to the column web and reduced damage to the beam if the lighter column is employed. Figure 11b shows the reduced damage to the beam web if the web of the reference model is reinforced as noted earlier, while comparison of Figure 11c and 11d shows the reduced damage and stress levels in the column when the web of the smaller column is reinforced. Finally, Figure 11e shows that the reduced damage to both the beam and the column webs is reinforced with the model with the lighter column section. These comparisons show that the addition of web reinforcement to create a total effective thickness of 75% of the gusset plate thickness eliminated all damage to the beam and the columns and significantly changed and reduced local stress demands in the beam and column webs.

Extensive beam and column damage was observed in the experiment, and the comparisons in Figures 10 and 11 suggest that the relative thickness of the gusset plate to beam and column web thickness is a contributing cause of this damage. In the experiments, the relatively thicker gusset plates sustained minimal yielding in contrast to the extensive yielding in the relatively thin beam and column webs. In addition, the gusset plate welds sustained damage. This is logical when considering that the webs of the W16×50 beam, W12×72 column and W12×106 column were 0.38, 0.43 and 0.61 in. (9.7, 11 and 15.5 mm) thick, respectively, while the gusset plates were 1 in. (25.4 mm) thick. The stress in the gusset plate has a direct path into the beam and column web, so a BRB that requires a thick gusset plate should also require a relatively thick beam and column web. This situation is aggravated with BRBs as compared to buckling braced frames because brace buckling reduces stress demands on the gusset although increasing deformation demands on the gusset.

Analyses were performed to evaluate this observation. Stresses in the beam and column webs may be reduced by increasing the thickness of the beam and column web by the addition of web reinforcement, decreasing the thickness of the gusset plate, or changing the connection configuration to alleviate the problem.

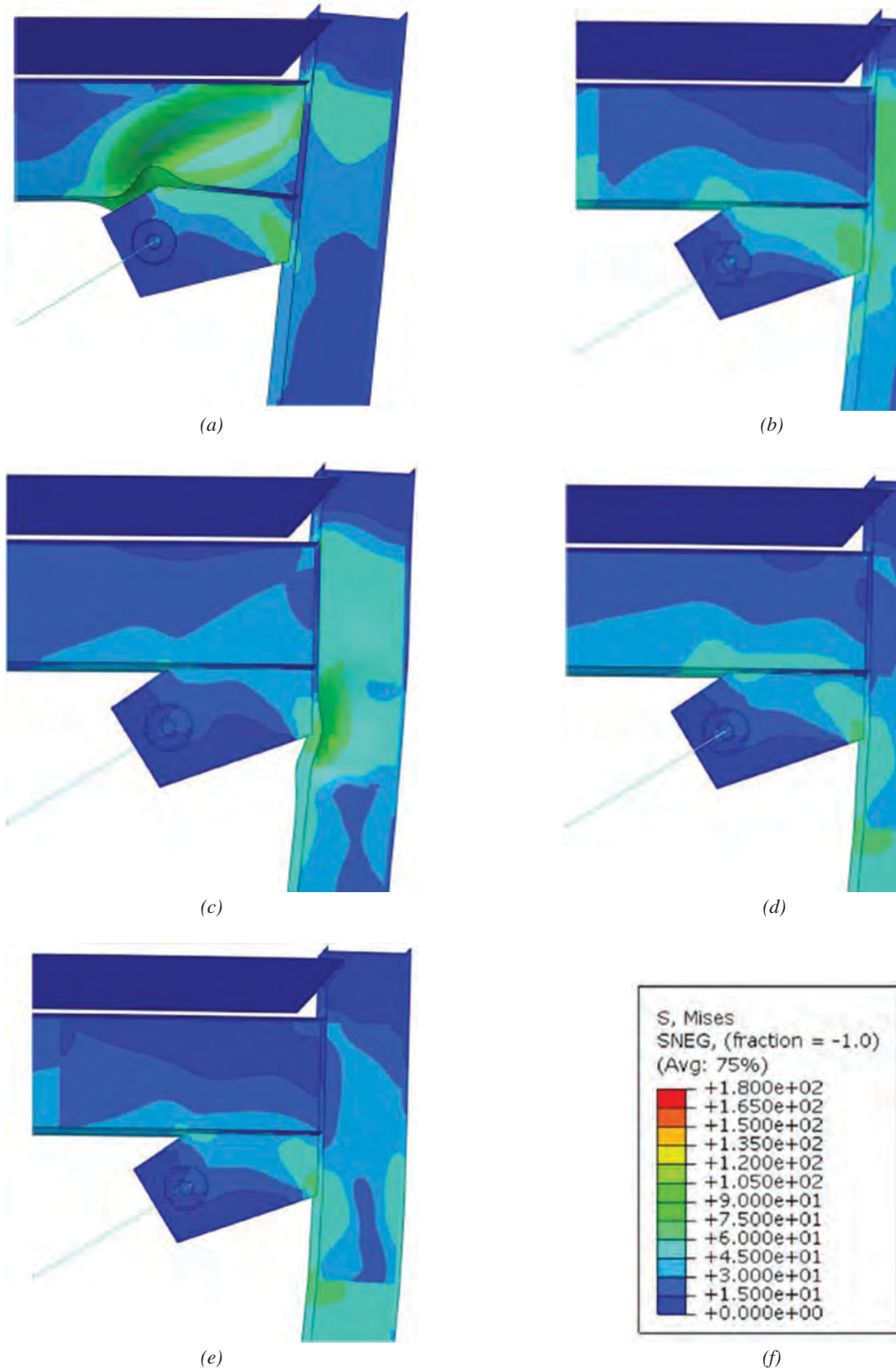

Fig. 11. Simulation results stress contours and deformed shape at 3.5% story drift (typical for deformed shapes): (a) reference model; (b) reference with 75% beam web stiffener; (c) small column model; (d) small column model with 75% column web stiffener; (e) small column model with 75% beam and column stiffeners; (f) contour legend.

Table 2. Parametric Study Response Values						
Model	Peak Base Shear, kips (kN)	Peak Moment,* kip-ft (kN-m)	Maximum PEEQ at Connection Interface (see Figure 9)			
			Beam	Column	Gusset Plate at Beam	Gusset Plate at Column
Reference	347.2 (1545)	611.8 (830)	0.286	0.106	0	0.143
Reference with 1-in. gusset plate	346.7 (1543)	612.5 (831)	0.318	0.166	0	0.055
Reference with 0.75-in. gusset plate	345.2 (1536)	578.6 (785)	0.256	0.046	0.023	0.565
Reference with 0.625-in. gusset plate	343.8 (1530)	570.5 (774)	0.233	0.03	0.047	0.689
Reference with 0.5-in. gusset plate	344.9 (1535)	542.5 (736)	0.196	0.017	0.097	0.818
Reference with 0.75-in. gusset plate and edge stiffener	344.9 (1535)	609.6 (827)	0.277	0.089	0.027	0.12
Reference with 0.5-in. gusset plate and edge stiffener	345.8 (1539)	580.1 (787)	0.208	0.03	0.112	0.354
Reference with 75% beam web stiffener	369.7 (1645)	612.5 (831)	0.087	0.114	0	0.157
Reference with 50% beam web stiffener	364.7 (1623)	614 (833)	0.175	0.11	0	0.148
Smaller column	303.4 (1350)	263.1 (357)	0.04	0.297	0	0
Smaller column with column web stiffener	312.8 (1392)	361.2 (490)	0.082	0.08	0	0.031
Smaller column with beam and column web stiffener	320 (1424)	375.9 (510)	0.026	0.08	0	0.09
* Moment in column B-1 at gusset plate edge at top of second story.						

Reducing Gusset Plate Thickness

Because the relative thickness of the gusset plate to the beam and column web affects the frame damage, it is logical to think that slightly thinner gusset plates may be beneficial. The reference frame had a 1-in. (25.4-mm) gusset plate thickness, but a number of factors, including pin bearing stress, were considered in the selection of that thickness, so thinner plates may be possible. Four modifications to the reference frame were made with 0.5-, 0.625-, 0.75- and 1.25-in. (12.7-, 15.9-, 19.1- and 38.1-mm) gusset plate thickness. The 0.75- and 1.25-in. (19.1- and 38.1-mm) gusset plate satisfied all AISC *Steel Construction Manual* (2005) design limit states. The 0.5- and 0.625-in. (12.7- and 15.9-mm)-thick gusset plates did not satisfy the standard buckling expression but were included in the analysis for completeness and to assess the effectiveness of this design expression. Thinner gusset plates clearly reduced the damage and stress levels in the beam and column webs. Table 2 shows that the maximum PEEQ demand in the beam was 0.196 and 0.286 with the 0. and 1.0-in. (12 and 25-mm)-thick gusset plates, respectively. Larger reductions were noted in the column, where the maximum PEEQ was 0.017 and 0.106 with the 0.5- and 1.0-in. (12.7- and 25-mm)-thick gusset plates, respectively. These reductions in PEEQ reflect reduced strain demand and inelastic damage to the beam and the column, but there was a corresponding increase in damage to the thinner gusset plates. Buckling of the gusset plate occurred in the analysis of models with 0.5-, 0.625- and 0.75-in. (12.7-, 15.9- and 19.1-mm)-thick gusset plates. These instabilities occurred at story drifts less than 1% for the 0.5- and 0.625-in. (12.7- and 15.9-mm)-thick gusset plates and at approximately 2.5% for the 0.75-in. (19.1-mm)-thick gusset plate.

Edge stiffeners were added to thinner gusset plates along the long edge to prevent extreme deformation of the gusset, and these stiffeners reduced the damage to the gusset and correspondingly increased the damage to the beam and

column so that it approximated the damage of the thicker gusset plates. This can be seen by comparison of PEEQ values in Table 2. With this evaluation, it is clear that thinner gusset plates are unlikely to be effective in reducing unwanted damage in BRBs because BRBs have large strain hardening and increasing brace forces compared to buckling brace frames.

Continuity Plates

A model with column continuity plates added at the second floor of the W12×72 column was analyzed to assess the impact on the column flange demands at the beam bottom flange. As previously discussed, the column flange was damaged at this location in a similar manner to the damage observed in moment frame columns in the 1994 Northridge earthquake (see Figure 3d). Figure 12 shows the plastic strain demand in the column flange in the elements on either side of the beam bottom flange for the models with and without the continuity plates. The continuity plate thickness was equal to one-half the beam flange thickness. The maximum strain demand occurs in the center of the column at the web location, and the demands in the column without the continuity plates are three times the demands in the column with the continuity plates, indicating a much higher likelihood of flange tearing when continuity plates are not provided.

Beam Moment Releases

Beam moment releases such as illustrated in Figure 2 and employed by Fahnestock and colleagues in a prior test program (2007) were also evaluated in a separate model. This detail dramatically reduces the demands on both the beam and columns. It effectively eliminates the need for beam and column web stiffeners and reduces the demands on the gusset plates. However, there are some consequences of this choice. In particular, a significant rotation must be permitted in the floor beam at the edge of the gusset plate connection. Allowances in the design of the floor slab may be required to permit this rotation. More research needs to be performed on this type of connection to assess the effect of the slab before recommendations can be made regarding the use of this.

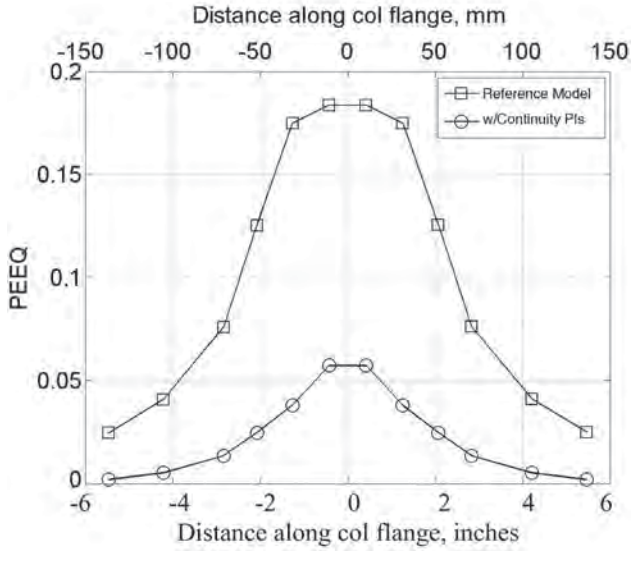

Fig. 12. Strain demand in column A-1 flange at second-floor bottom beam flange.

Welds Joining Gusset to Beam and Column

Weld fracture was noted in the test frame, and one model explicitly investigated the weld cracking. This model was basically the reference model, but it explicitly modeled the geometry of the fillet welds joining the gusset to the beam and column. This was accomplished by using a weld-specific constitutive model and shell elements modeling the weld geometry at the interface. The thickness assigned to the shell elements was total throat thickness of the fillet welds (⅜-in. fillets were used on both sides of the gusset plate).

The constitutive model was calibrated to match the force-normalized deformation (p) response given by Equation 1 (AISC, 2005).

$$P = 0.60F_{EXX}(1.0 + 0.5\sin^{1.5}\theta)\,[p(1.9 - 0.9p)]^{0.3} \qquad (1)$$

where P is the nominal strength of the weld segment at a deformation Δ, F_{EXX} is the weld electrode strength (70 ksi), θ is the load angle measured relative to the weld longitudinal axis and p is the ratio of element deformation Δ to its deformation at maximum stress, Δ_{max}, given by Equation 2. A load angle, θ, of 50 degrees was used because the simulations showed that the stress perpendicular to the weld was a larger component than shear. This angle results in a weld strength increase of 35% relative to a longitudinally loaded weld. The strength increase for a weld that is loaded at 90 degrees is 50%.

$$\Delta_{max} = 1.087w(\theta + 6)^{-0.65} \leq 0.17w \qquad (2)$$

where w is the weld size.

In the test frame, initial tearing was observed in the gusset plate welds at a roof story-drift ratio of approximately 2.3%. The PEEQ, PE and elongation of the shell element modeling the weld were sampled in the elements at the edge of the gusset plates at this drift level, and they are listed in Table 3. Also listed are the mean values for each index and the standard deviation and the coefficient of variation (COV). The PE and PEEQ are commonly used as indicators of crack initiation and fracture, and Table 3 shows that these parameters are extremely large when the fillet welds designed by the uniform force method are considered. PEEQ

Table 3. Weld Tearing Analysis Results					
	With Weld Model			Without Weld Model	
Gusset Plate	PEEQ	PE	Elongation, in. (mm)	PEEQ	PE
2nd floor column A-1	3.6	0.23	0.0041 (0.105)	0.125	0.011
3rd floor column B-1	3.04	0.17	0.0025 (0.064)	0.149	0.0131
2nd floor column B-1	2.68	0.134	0.0019 (0.048)	0.071	0.005
Mean	3.11	0.178	0.0028 (0.072)	0.115	0.001
Standard deviation	0.463	0.049	0.0011 (0.029)	0.04	0.005
COV (%)	14.9	27.4	40.7	34.8	46.4

had the smaller COV and was used as a better indicator of weld cracking in the test frame. Cracking was observed at an average PEEQ of 3.11. Figure 13 shows the variation of the PEEQ at the three different gusset plates as a function of story drift. PEEQ is increasing rapidly at larger drift levels

A second simulation was performed with welds sized to develop the plastic tensile capacity of the gusset plate (⅞-in. fillet welds). Figure 13 also shows the PEEQ values for this model. PEEQ is dramatically smaller with the increased weld size, and crack initiation in the welds would not be expected even until deformations have increased beyond 3.25% drift. This analysis shows that the likelihood of weld tearing is significantly reduced or eliminated when the welds are designed for the strength of the plate.

DESIGN AND DETAILING RECOMMENDATIONS

Based on the experimental work and simulations described earlier, the following recommendations are made for the corner connection region of BRBF systems.

Beam

1. Beam web reinforcement should be placed at the corner gusset plate locations and extend at least to the larger of $0.75d_b$ and 12 in. (300 mm) beyond the gusset plate edge, as shown in Figure 14. This reinforcement should be placed as close to the column face as possible and will be limited by the beam web connection plates or angles. The web reinforcement should increase the total web

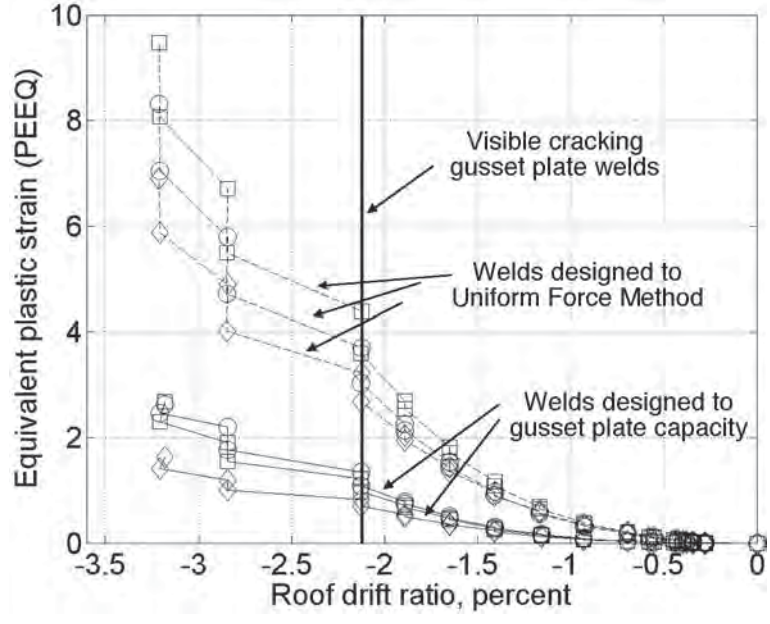

Fig. 13. Plastic strain demands at gusset plate edge.

thickness to 75% of the gusset plate thickness. This ratio may be reduced given further experimental verification.

2. Backing bars should be removed at the beam bottom flange CJP connection to the column, as they are required in special moment frames per the *Seismic Provisions*, unless there is a gusset plate connection to the column and bottom flange of the beam.

Column

3. Column web reinforcement should be installed in the panel zone and within the gusset region and extend at least to the larger of $0.75d_c$ and beyond the gusset plate edge as shown in Figure 14. The web reinforcement should increase the total web thickness to 75% of the gusset plate thickness.

4. Continuity plates should be provided in the column at the beam flanges according to the *Seismic Provisions* when the beam flanges are connected to the column and expected to behave as a partially or fully restrained connection (Figure 14).

Gusset Plate

5. The current LRFD gusset plate design limit states should be used, except all welds connecting the gusset plate to the beams and columns should be CJP welds or fillet welds with a strength equal to the yield capacity of the gusset plate. The expected yield strength of the plate, R_yF_y, should be used in this calculation.

SUMMARY AND CONCLUSIONS

BRBFs are a commonly used seismic resisting system. However, most studies have focused on the BRB and neglected its interaction with the adjacent components. Recent tests indicate that unwanted damage modes are sustained by BRBFs, including local buckling of the beams and tearing of the interface weld. To improve the response and mitigate these mechanisms, an analytical study was undertaken. The study used an experimental study of a two-story frame as its basis. Using high-resolution modeling techniques, a validated model was developed. This model was then used to perform a parametric study. The primary objectives of the study were to quantify the effects of various parameters on the demands and behaviors of the joint region and develop verified design and detailing recommendations to improve the performance of these systems.

The study resulted in the following conclusions:

1. Reducing the gusset plate thickness reduced the demands in the beam and column at the gusset interfaces. However, buckling of the gusset plate limits how thin these can be. Therefore, this is not an effective way of reducing component demands in the connection region of BRBFs. This is different than recommendations for SCBFs because buckling braces are a softening system after brace buckling, while BRBFs continue to sustain large increases in brace force after yielding of the BRB.

2. Analyses shows that designing the weld for the strength of the plate significantly reduces the local strain demand in the connection and is expected to reduce crack initiation and prevent weld tearing and fracture until much larger story drifts. Therefore, weld connecting the

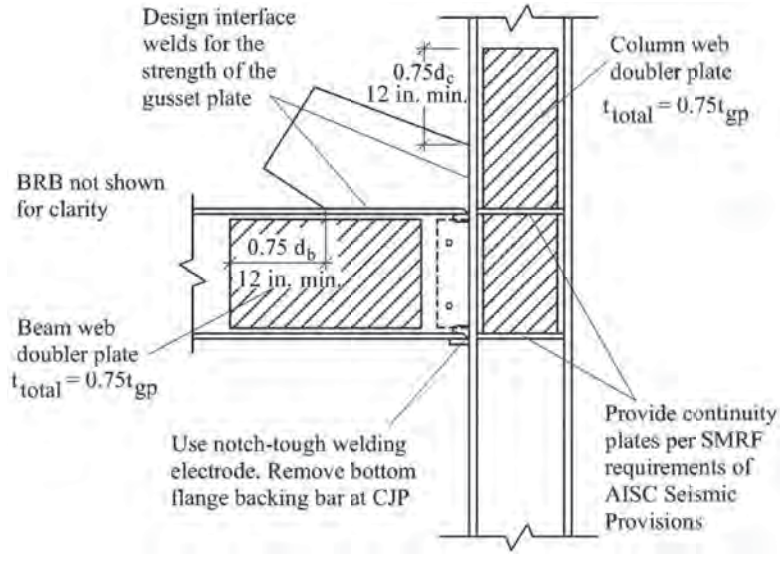

Fig. 14. Recommended detailing at corner connection region of BRBF.

gusset plate to the beam and column should be sized to meet the strength of the gusset plate to mitigate weld tearing.

3. A smaller column reduced the demands in the beam, including local web and flange deformation at all drift levels. However, the demand and deformation in the column was increased. Adding column web reinforcement within the gusset region mitigated these demands and deformations, and while this caused a slight increase in beam demands, the resulting beam demands were still considerably less than those seen in the reference model and had negligible impact on the behavior and performance of the beam. In lieu of adding doubler plates, it may be more economical to increase the column or beam shape to a size that has an appropriate web thickness but may be overdesigned for flexure and axial load.
4. The demands and local deformation in the beams and columns within the connection region were shown to be inversely proportional to the ratio of the beam web thickness to the thickness of the gusset plate. In other words, for a given beam or column size, a thick gusset plate will increase the demands on these elements relative to a thinner gusset plate. These demands are also dependent on other factors, such as the relative beam and column size and the mechanism used to accomplish the target thickness ratio (e.g., thin gusset plate versus adding a web reinforcement). Given that there is a limit on how thin a gusset plate can be due to potential buckling, adding beam web reinforcement is a more appropriate solution to mitigate damage. Adding beam web reinforcement such that the web to gusset plate thickness ratio was 0.75 is recommended.

ACKNOWLEDGMENTS

The authors gratefully acknowledge the support of the National Science Foundation's Network for Earthquake Engineering Simulation (Grant No. CMS-619161) and the American Institute of Steel Construction. The opinions and findings expressed here are those of the authors alone and do not necessarily reflect the views of the sponsoring agencies.

REFERENCES

ABAQUS (2010), *ABAQUS version 6.10 documentation*, Simulia.

AISC (2005), *Steel Construction Manual,* 13th ed., American Institute of Steel Construction, Chicago, IL.

AISC (2010), *Seismic Provisions for Structural Steel Buildings,* ANSI/AISC 341-10, American Institute of Steel Construction, Chicago, IL.

Black, C., Makris, N. and Aiken, I. (2004), "Component Testing, Seismic Evaluation and Characterization of Buckling-Restrained Braces," *Journal of Structural Engineering*, Vol. 130, No. 6, pp. 880–894.

Chao, S.H., Khandelwal, K. and El-Tawil, S. (2006), "Ductile Web Fracture Initiation in Steel Shear Links," *Journal of Structural Engineering*, Vol. 132, No. 8, pp. 1192–1200.

Chen, C., Lai. J. and Mahin, S. (2008), "Seismic Performance Assessment of Concentrically Braced Steel Frame Buildings," *Proceedings of the 14th World Conference on Earthquake Engineering*, Beijing, China.

Christopolus, A.S. (2005), "Improved Seismic Performance of Buckling Restrained Braced Frames," M.S. Thesis, University of Washington, Seattle, WA.

El-Tawil, S., Mikesell, T. and Kunnath, S.K. (2000), "Effect of Local Details and Yield Ratio on Behavior of FR Steel Connections," *Journal of Structural Engineering*, Vol. 126, No. 1, pp. 79–87.

Fahnestock, L.A., Ricles, J.M. and Sause, R. (2007), "Experimental Evaluation of a Large-Scale Buckling-Restrained Braced Frame," *Journal of Structural Engineering*, Vol. 133, No. 9, pp. 1205–1214.

Hancock, J.W. and Mackenzie, A.C. (1976), "On the Mechanics of Ductile Failure in High-Strength Steel Subjected to Multi-Axial Stress States," *Journal of Mechanical and Physical Solids*, Vol. 24, pp. 147–169.

Kanvinde, A. and Deierlein, G. (2006), "Void Growth Model and Stress Modified Critical Strain Model to Predict Ductile Fracture in Structural Steels," *Journal of Structural Engineering*, Vol. 132, No. 12, pp. 1907–1918.

Meritt, S., Uang, C. and Benzoni, G. (2003), "Subassemblage Testing of Star Seismic Buckling-Restrained Braces," Report No. TR-2003/04, University of California, San Diego, La Jolla, CA.

Palmer, K.D. (2012), "Seismic Behavior, Performance and Design of Steel Concentrically Braced Frame Systems," Ph.D. Dissertation, University of Washington, Seattle, WA.

Palmer, K.D., Christopulos, A.S., Lehman, D.E. and Roeder, C.W. (2014), "Experimental Evaluation of Cyclically Loaded, Large-Scale, Planar and 3-D Buckling-Restrained Braced Frames," submitted for publication review, *Journal of Constructional Steel Research,* Elsevier.

Romero, P., Reaveley, L., Miller, P. and Okahashi, T. (2007), "Full Scale Testing of WC Series Buckling-Restrained Braces," Final Report to Star Seismic, University of Utah, Salt Lake City, UT.

Uriz, P. (2005), "Towards Earthquake Resistant Design of Concentrically Braced Steel Structures," Ph.D. Dissertation, University of California, Berkeley.

Wigle, V.R. and Fahnestock, L.A. (2010), "Buckling-Restrained Braced Frame Connection Performance," *Journal of Constructional Steel Research*, Vol. 66, pp. 65–74.

Yoo, J. (2006), "Analytical Investigation on the Seismic Performance of Special Concentrically Braced Frames," Ph.D. Dissertation, University of Washington, Seattle, WA.

Finite Element Modeling of Steel Moment Connections with Fracture for Structural Fire Analyses

MINA SEIF, THERESE MCALLISTER, JOSEPH MAIN and WILLIAM LUECKE

ABSTRACT

Performance-based methodologies to evaluate the fire performance of structures are needed to move beyond the prescriptive procedures currently in use, which cannot be used to determine actual structural performance in fire. Analytical methods are needed for simulating the performance of structural systems, including connections, subject to realistic fire effects. Framing connections may be subject to large, unanticipated deformations and loads during fire events, and connection failure may lead to other failures or local collapse. This paper presents the development of detailed finite element models of typical moment connections for steel-framed structures. These detailed models incorporate temperature-dependent material models that have been calibrated against available test data from tensile coupons, including the modeling of necking behavior and fracture. The detailed connection models are loaded to failure to identify the applicable failure mechanisms. Connection performance at ambient and elevated temperatures is evaluated, and dominant failure modes are identified.

Keywords: plastic strain, fracture, erosion strain, finite element analysis, material modeling, structural fire effects.

INTRODUCTION

There is a lack of tools for modeling the response of structural system response, including connections, to realistic, uncontrolled fires. Fire protection of steel structures is usually provided through prescriptive requirements based on the standard fire test (ASTM, 2011), which has changed little since it was introduced in 1917. Such tests typically characterize heat transmission through elements and subsystems but do not provide information about structural performance in real fire. A fuller understanding of the problem will lead to the development of analytical tools and design standards that explicitly consider realistic fire loading for both the design of new buildings and the assessment and retrofit of existing ones. Development of design tools for evaluating fire effects usually requires detailed finite element (FE) analyses that consider all failure modes, including local buckling, at elevated temperatures.

M. Seif, Research Structural Engineer, National Institute of Standards and Technology (NIST), Gaithersburg, MD (corresponding). Email: mina.seif@nist.gov

T. McAllister, Research Structural Engineer, National Institute of Standards and Technology (NIST), Gaithersburg, MD. Email: therese.mcallister@nist.gov

J. Main, Research Structural Engineer, National Institute of Standards and Technology (NIST), Gaithersburg, MD. Email: joseph.main@nist.gov

William Luecke, Materials Research Engineer, National Institute of Standards and Technology (NIST), Gaithersburg, MD. Email: william.luecke@nist.gov

Paper No. 2014-17

During exposure to fire, large axial compressive and/or tensile forces may develop in floor beams and their connections. A number of researchers have studied the effects of fire on connections, though most of the literature addresses shear connections and semi-rigid connections. Sarraj et al., (2007) developed detailed solid element models for shear tab connections with bolts to evaluate bolt shear and bearing behavior. Yu et al., (2009) performed an experimental investigation of the behavior of shear tab connections subjected to vertical shear and tensile forces at elevated temperatures and measured the moment-rotation capacity of the shear tab connections. Seif and McAllister (2013) discussed failure modes of shear tab connections at elevated temperatures. Yang et al., (2009) conducted tests of welded moment connections where connections and members immediately adjacent to the connection were heated to 550 °C to 650 °C and then loaded to failure under an applied moment (top flange in tension and bottom flange in compression). Yielding, necking, fracture, bolt elongation (shear) and local buckling were observed, and a reduction of member stiffness to 25% of ambient values was reported. Al-Jabri et al., (2006) studied the moment–rotation–temperature characteristics of the end plate moment connections subjected to a concentrated load and elevated temperatures. Quiel and Garlock (2010) conducted detailed finite element analyses of shear and moment connections for two- and three-dimensional building frames. Their results indicate that thermal gradients can produce significant changes in the deflection mechanics and plastic *P-M* limit-state behavior.

This paper presents a study employing FE analysis with geometric and material nonlinearities, using solid elements to model the failure modes of a steel moment connection

under axial loading at elevated temperatures. Recently developed temperature-dependent material models for different types of steels used in connections are implemented. FE analyses of coupon models are performed to verify the implementation of these material models. Results are presented that illustrate the detailed modeling of the connection and the failure modes under varying load and temperature conditions. While these results apply to a particular type of moment connection under axial loading, the modeling approach is quite general and could be used to analyze other types of steel connections under more realistic thermal and structural loading scenarios. The analysis results presented in this paper will be used in formulating reduced connection models for FE analyses of structural systems at ambient and elevated temperatures.

PROTOTYPE BUILDING DESIGNS

As described in Lew et al., (2013), the National Institute of Standards and Technology (NIST) worked with a panel of practicing structural engineers across the United States to develop a number of prototype steel-frame building designs for use in assessing the robustness of structural systems. The buildings were designed according to the American Society of Civil Engineers 7-02 standard (ASCE, 2002) and its referenced material design standards, including the American Institute of Steel Construction's *Load and Resistance Factor Design Specification for Structural Steel Buildings* (AISC, 1999) and *Seismic Provisions for Structural Steel Buildings* (AISC, 2002). These prototype buildings are considered representative of typical construction, and a moment connection from one of the prototype buildings, shown in Figure 1, was selected for analysis in this study.

The moment connection shown in Figure 1 is a welded unreinforced flange, bolted web (WUF-B) connection, which is one of the prequalified steel connections listed in FEMA 350 (FEMA, 2000). The WUF-B connection in Figure 1 is taken from the second-floor level of a seismically designed intermediate moment frame (IMF) in a 10-story prototype building designed for Seismic Design Category C. The number and size of the ASTM A490 bolts varied for the WUF-B connections within the moment frames, as did the thickness and height of the shear tabs. ASTM A992 structural steel ($F_y = 50$ ksi [345 MPa]) was used in all beams and columns. ASTM A36 steel ($F_y = 36$ ksi [250 MPa]) was used for the shear tabs and continuity plates at the beam-column connections.

CONNECTION FINITE ELEMENT MODELING

Detailed nonlinear FE analyses were conducted to simulate the failure modes of moment connections under elevated temperatures. In each analysis, the connection was subjected to a monotonically increasing axial displacement,

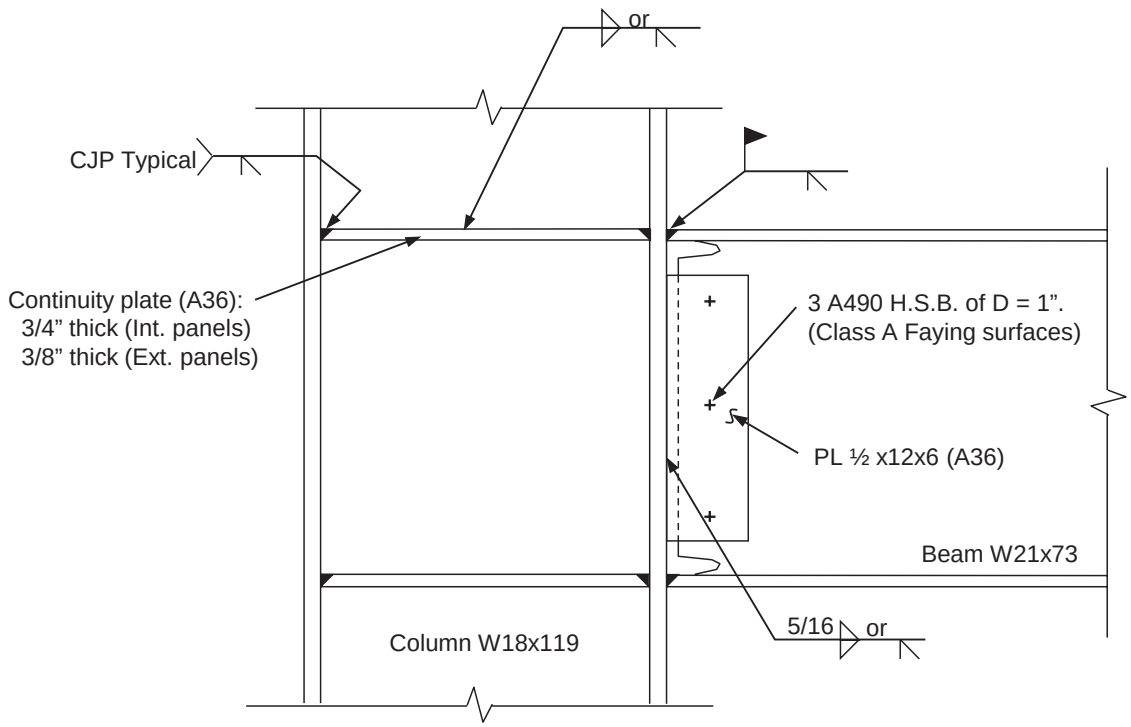

Fig. 1. Details of WUF-B moment connection.

either tensile or compressive. Analyses were performed using explicit time integration in LS-DYNA (LSTC, 2012), and the prescribed displacements were applied gradually to ensure that dynamic effects were negligible (i.e., to ensure quasi-static loading conditions). Both compressive and tensile loading conditions are of interest because they represent the types of loading imposed on connections in the heating and cooling phases of a fire, respectively.

While the displacements imposed on a connection in a realistic fire depend on the temperature distribution within the structural elements and the thermal restraint imposed by the structural configuration, the controlled loading protocol considered (see Figure 2) enabled investigation of the behavior, failure modes and ultimate capacities of the connections at different temperatures. Analyses under prescribed displacements were performed at four temperatures (20 °C, 400 °C, 500 °C and 600 °C), with the temperature in each analysis being uniform and constant. With constant temperature throughout each analysis (i.e., temperatures were not ramped up from the ambient temperature), no stresses due to restraint of thermal expansion were present in the analyses. Future research will consider more realistic thermal restraints, loads and fire scenarios.

The WUF-B connection shown in Figure 1 was modeled using finely meshed three-dimensional solid elements for the beam, bolts and shear tab, as shown in Figure 3. Fully integrated eight-node solid elements were used. A typical element size of 0.12 in. (3 mm) was used for the beam and the shear tab. A finer mesh with a typical element size of 0.06 in. (1.5 mm) was used for the bolts. Contact was defined between the bolts, shear tab and beam web to model the transfer of forces through the bolted connection, including friction, with a value of 0.3 assumed for both the static and dynamic coefficients of friction. No pretension in the bolts was considered in the analyses. All degrees of freedom were restrained for nodes on the welded ends of the shear tab and the beam flanges.

The temperature-dependent material models used for FE analysis of the moment connections at elevated temperatures are discussed in the following section. ASTM A572 Grade 50 steel, with an ambient-temperature yield strength of F_{y0} = 50 ksi (345 MPa), is used for the beam and column; ASTM A36 steel, with F_{y0} = 36 ksi (250 MPa), is used for the shear tab; and steel with F_{y0} = 70 ksi (485 MPa) is used for the welds. ASTM A490 bolts, with F_{y0} = 130 ksi (896 MPa), are used for the WUF-B connection (see Figure 1 for connection details).

TEMPERATURE-DEPENDENT MATERIAL MODELING

A key issue in evaluating the response of structural systems to fire effects is the representation of material behavior at elevated temperatures. In addition to stress-strain behavior, modeling of fracture is required to capture failure modes such as tear-out in connection plates and bolt shear. The use of explicit finite element software packages allows for modeling of sequential failures, including fracture. Fracture can be simulated using element erosion, in which elements are removed from the analysis when specified failure criteria are satisfied. However, the basis for determining and implementing material failure criteria at elevated temperatures is not well established in the literature. This section presents a finite element material modeling methodology for structural steels at elevated temperatures, including erosion-based

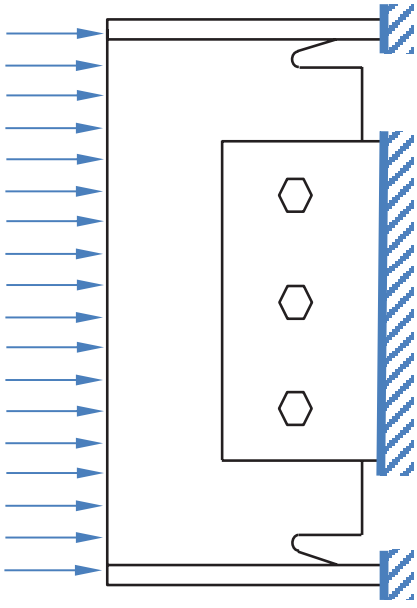

Fig. 2. Schematic of compressive axial displacements imposed on a WUF-B connection.

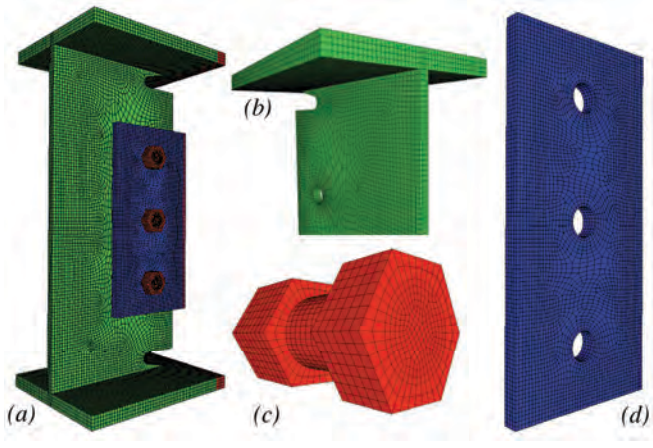

Fig. 3. Detailed model of the WUF-B connection: (a) full model, (b) beam, (c) bolt, and (d) shear tab.

modeling of fracture. A recently developed temperature-dependent material model for structural steels is combined with a plastic strain-based failure criterion for element erosion. Using finite element models of tensile coupons, this failure criterion is calibrated against experimental data on elongation at fracture, and the influence of temperature and mesh size on the failure criterion is investigated.

Seif et al., (2015) developed an empirical model that provides temperature dependent material models for any structural steel. The model is based on experiments conducted at NIST and published data from numerous experiments reported in the literature. The model accounts for the change in yield strength and post-yield strain hardening with temperature. However, the model does not account for creep effects. Equations for true stress and true strain, discussed later, are required to define material models in LS-DYNA analyses. However, as discussed subsequently, detailed finite element models of tensile coupons are used to obtain engineering stress-strain curves for comparison with experimental measurements, particularly regarding the post-ultimate behavior, including necking and fracture.

Experimental data to support temperature-dependent material properties for structural bolts are more limited than for structural steel, particularly data regarding the temperature-dependence of deformations or elongations at fracture. Much of the available experimental data for bolt shear tests is influenced by deformation of the shear loading assembly, making it difficult to isolate the bolt performance. Given these limitations, an interim approach for modeling the temperature-dependent nonlinear material behavior and fracture of bolts is described later.

Structural Steel

For structural steel (beams, columns and shear tabs), the temperature-dependence of the yield strength F_y is expressed as:

$$F_y(T) = F_{y0} \cdot \left[r_5 + (1 - r_5) \cdot \exp\left(-\frac{1}{2}\left(\frac{\Delta T}{r_3} \right)^{r_1} - \frac{1}{2}\left(\frac{\Delta T}{r_4} \right)^{r_2} \right) \right] \quad (1)$$

where F_{y0} is the yield strength at ambient temperature, ΔT (in °C) is the increase in temperature above the ambient temperature and r_1 through r_5 are coefficients depending on the type of steel. For rolled structural steel, $r_1 = 7.514$, $r_2 = 1.000$, $r_3 = 588$ °C, $r_4 = 676$ °C and $r_5 = 0.090$.

The elastic modulus E (in GPa) is expressed a function of the temperature T (in °C) as follows:

$$E(T) = E_0 \cdot \left[\exp\left(-\frac{1}{2}\left(\frac{\Delta T}{e_3} \right)^{e_1} - \frac{1}{2}\left(\frac{\Delta T}{e_4} \right)^{e_2} \right) \right] \quad (2)$$

where $E_0 = 206$ GPa (2987 ksi) is the value at ambient temperature and e_1 through e_4 are coefficients depending on the type of steel. For rolled structural steel, $e_1 = 3.768$, $e_2 = 1.000$, $e_3 = 639$ °C and $e_4 = 1650$ °C.

The true stress, σ_{true}, is expressed as a function of true strain, ε_{true}, as follows:

$$\sigma_{true} = \begin{cases} E(T)\varepsilon_{true} & \text{for } \varepsilon_{true} < \dfrac{F_y(T)}{E(T)} \\ \left(F_y(T) + \left(1006 - 0.759F_{y0}\right) \exp\left(-\left(\dfrac{T}{540} \right)^{7.82} \right) \left(\varepsilon_{true} - \dfrac{F_y(T)}{E(T)} \right)^{0.503} \right) & \text{for } \varepsilon_{true} \geq \dfrac{F_y(T)}{E(T)} \end{cases} \quad (3)$$

where it is noted that E and F_y depend on temperature according to Equations 1 and 2. Figure 4 shows the true stress-strain curves for the A572 steel, generated using this temperature-dependent material model. The point corresponding to the ultimate engineering stress (also referred to as the tensile strength) for each temperature is indicated by a red dot, and the true stress-strain curves are extended linearly beyond this point, as discussed subsequently.

Equation 3 was calibrated to match available experimental data up to the tensile strength, and special care is needed in modeling the post-ultimate material behavior, including necking and fracture. Seif et al., (2015) developed an approach for modeling the post-ultimate behavior of structural steel at elevated temperatures by using element erosion to represent fracture. The onset of erosion was calibrated to match available experimental data of fracture in coupons at elevated temperatures. Because the simulation of post-ultimate necking and fracture depends on the model mesh size, the coupon models had the same mesh size as the connection model for the calibration procedure. The calibration is invalid if the mesh sizes between the coupon and the model are different. The stress-strain relationship computed from Equation 3 was used up to the ultimate engineering stress, after which the post-ultimate stress associated with necking and fracture was modeled with a tangential extension from the ultimate stress.

The failure criterion used for element erosion is based on the effective plastic strain, a scalar measure of plastic strain that incorporates its various tensor components. Element erosion is activated when the effective plastic strain in any element (i.e., the local plastic strain in a section or component) exceeds a specified critical value, called the erosion strain, ε_{er}. The erosion strain can be significantly larger than the engineering strain at fracture because the engineering strain represents an average strain over the gauge length, and the local plastic strain in the necked region can significantly exceed this average value. Analyses of detailed,

Table 1. Engineering and Erosion Strain Values at Fracture for Structural Steel		
Temperature (°C)	**Engineering Strain at Fracture**	**Erosion Strain at Fracture**
20	0.47	0.70
400	0.38	0.35
500	0.35	0.40
600	0.46	1.40

three-dimensional solid element models tensile coupons were conducted to calibrate the erosion strain values against available experimental data on elongation of tensile coupons, including data for ASTM A992 steel from Hu and Morovat (2009) and data for ASTM A572 Grade 50 steel from Luecke et al., (2005). Temperature-dependent values of the erosion strain were used in order to achieve the best agreement with the experimental data.

As the value of ε_{er} increases, the computed engineering strain at fracture also increases. For instance, at 400 °C, when $\varepsilon_{er,}$ increases from 0.70 to 0.90, the engineering strain at fracture, $\varepsilon_{eng,f}$, increases by about 10% from 0.45 to 0.50. To determine the appropriate value of erosion strain at each temperature, the erosion strain was adjusted until the resulting engineering strain at fracture matched a target value determined from the available experimental data. The target value of the engineering strain at fracture was selected as the mean value of experimental data at each temperature of interest (20 °C, 400 °C, 500 °C and 600 °C), and is plotted along with the experimental data in Figure 5.

The values of erosion strain, ε_{er}, in the FE model that matched the target values of engineering strain at fracture shown in Figure 5 for Grade 50 structural steels are listed in Table 1. Note that beyond 500 °C, the erosion strain greatly increased due to increased plasticity at elevated temperatures. Figure 6 shows engineering stress-strain curves obtained from FE analysis of tensile coupons for the engineering strain at fracture values shown in Figure 5 at

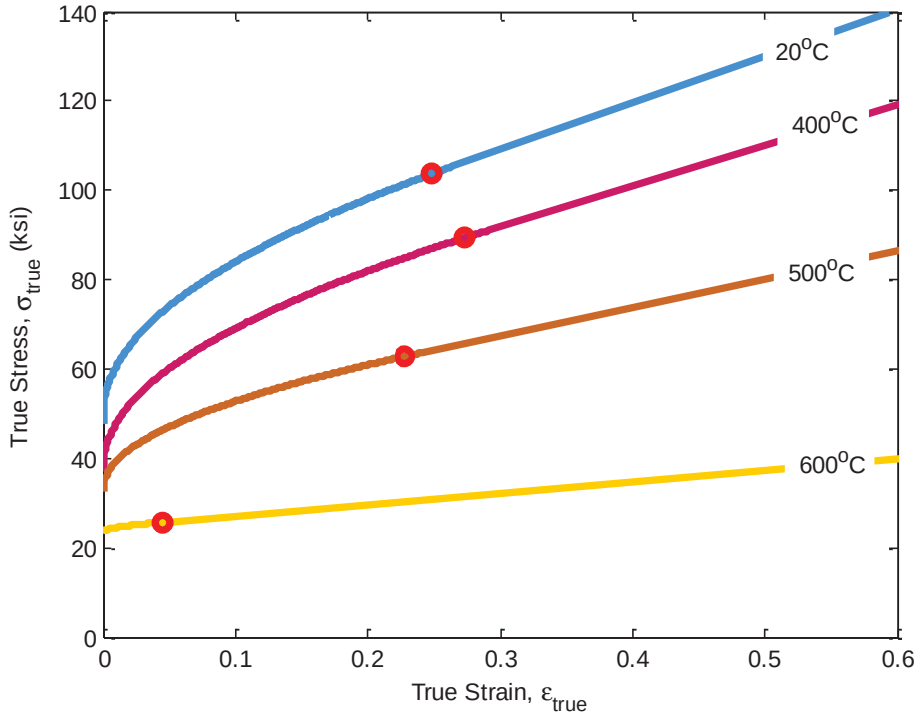

Fig. 4. True stress-strain curves for A572 steel, generated with Seif et al., (2015) temperature-dependent material model (1 ksi = 6.895 MPa).

temperatures of 20 °C, 400 °C, 500 °C and 600 °C. Due to the calibration procedure described earlier, the engineering strain values at fracture in Figure 6 closely match the target values in Figure 5. Note that due to the lack of experimental data in the literature regarding the effect of elevated temperatures on the strain at fracture of mild steel, A36 (of which the shear tabs are typically constructed), the values of ε_{er} were assumed to be equal to those of the A572 steel for the purpose of the analysis. This assumption did not affect the results because no fracture occurred in the shear tab. Similarly, the same values of ε_{er} were used for the weld material. However, because the F_{y0} of the welds was higher than that of the surrounding material, fracture of the welds did not occur.

Bolts

For high-strength bolts (A325 and A490), the temperature-dependence of the yield strength F_y is calculated from Equation 1, with $r_1 = 4.967$, $r_2 = 1.000$, $r_3 = 456$ °C, $r_4 = 2040$ °C and $r_5 = 0.000$. Compared to rolled steel, bolts sustain their F_y value with the increase of temperature up to about 400 °C, after which it drops dramatically. Figure 7 shows the degradation of the normalized yield strength with increasing temperature for ASTM A572 rolled steel and ASTM A325 and A490 bolts. Note that at 400 °C, both rolled steel and bolts sustain about 80% of their yield capacity. At 600 °C, rolled steel sustains about half of its yield capacity, while bolts lost more than 82% of their yield capacity. The ultimate strength, F_u, is calculated by using Equation 1 with the same values of r_1 through r_5 as for the yield strength, but with the ambient-temperature yield strength, F_{y0}, replaced by the ambient-temperature ultimate strength, F_{u0}.

The elastic modulus E for bolts is the same as that for rolled steel, calculated from Equation 2. The stress-strain relationship is not calculated from Equation 3, but rather a trilinear relationship as follows:

$$\sigma_{true} = \begin{cases} E(T)\varepsilon_{true}, & \varepsilon_{true} \le \varepsilon_y(T) \\ F_y(T) + \left[F_u(T) - F_y(T)\right]\dfrac{\varepsilon_{true} - \varepsilon_y(T)}{\varepsilon_u(T) - \varepsilon_y(T)}, & \varepsilon_y(T) < \varepsilon_{true} \le \varepsilon_u(T) \\ F_u(T) + \dfrac{0.08}{100}E(T)\left[\varepsilon_{true} - \varepsilon_u(T)\right], & \varepsilon_u(T) < \varepsilon_{true} \end{cases} \quad (4)$$

where $\varepsilon_y(T) = F_y(T)/E(T)$ is the temperature-dependent yield strain. The temperature-dependent ultimate strain, $\varepsilon_u(T)$, is assumed to have a value of 0.1 at 20 °C and to decrease linearly with temperature to a value of 0.05 at 600 °C. Figure 8 shows the trilinear stress-strain relationship of the A325 bolts at 20 °C, 400 °C, 500 °C and 600 °C. Similar to rolled

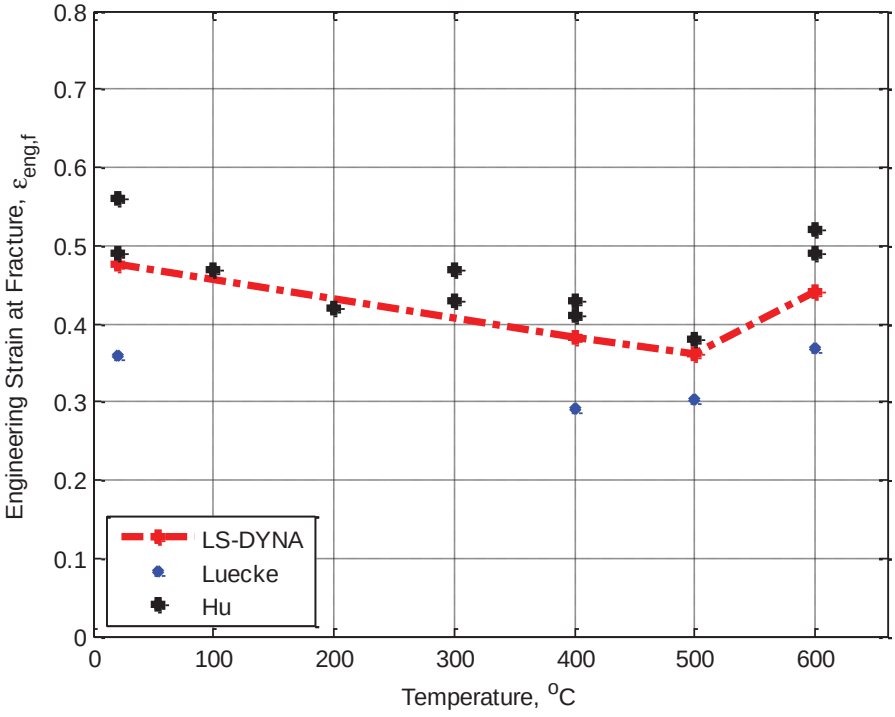

Fig. 5. Target values of engineering strain at fracture determined from experimental data.

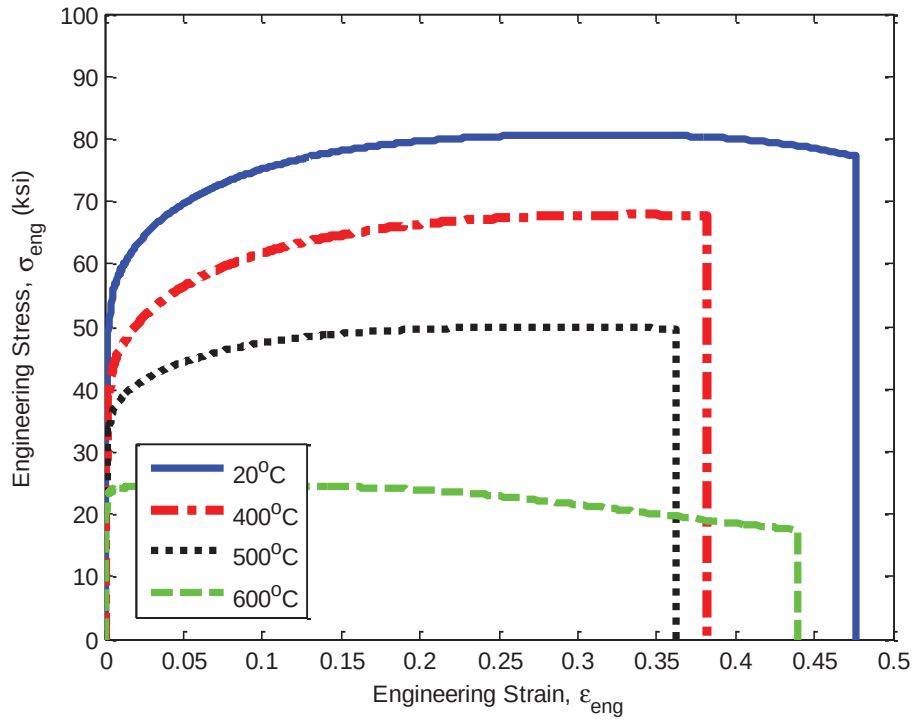

Fig. 6. Engineering stress-strain curves obtained from FE models of tensile coupons at selected temperatures.

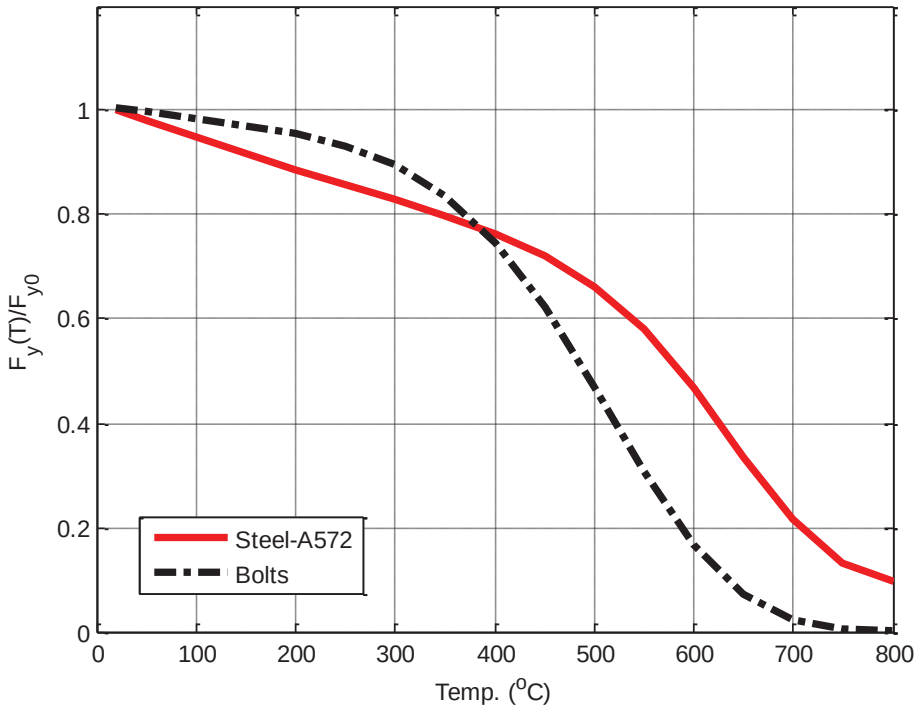

Fig. 7. Degradation of normalized yield strength versus the increase in temperature for rolled structural steel and bolts.

Table 2. Engineering and Erosion Strain Values at Fracture for A325 and A490 Bolts				
	Engineering Strain at Fracture		Erosion Strain at Fracture	
Temperature (°C)	A325	A490	A325	A490
20	0.210	0.16	0.50	0.35
400	0.204	0.16	0.55	0.40
500	0.246	0.19	0.75	0.55
600	0.276	0.22	0.75	0.60

steel, the failure criterion used for element erosion is based on the effective plastic strain. Element erosion is activated when the effective plastic strain in any element exceeds ε_{er}. The erosion strain is temperature dependent and based on analyses of detailed, three-dimensional solid-element models of A325 and A490 steel bolts. The values of ε_{er} were calibrated against available experimental data from Kodur et al., (2012). To determine the appropriate value of erosion strain at each temperature, the erosion strain was adjusted until the resulting engineering strain at fracture matched a target value determined from the available experimental data. Values of engineering strain and erosion strain at fracture for the A325 and A490 bolts reported by Kodur et al., are listed in Table 2. A more detailed discussion of the temperature-dependent models for structural steels at elevated temperatures is provided in Seif et al., (2015).

RESULTS AND DISCUSSION

The discussion in this section focuses on the behavior and failure modes of the WUF-B connection subjected to axial loading, as illustrated in Figure 2. Figure 9 shows the total axial load versus displacement curves for the WUF-B connection under both tensile and compressive loading at different temperatures. The displacement plotted in Figure 9 (and in Figures 10 and 11 subsequently) is the axial displacement imposed at the free end of the beam (the left end in Figure 2). A uniform axial displacement is imposed for the entire cross-section, with out-of-plane displacements unrestrained. Results in Figure 9 show that despite differences in failure modes, the overall capacity of the connection did not differ significantly between tensile and compressive loading conditions for each temperature (differences less

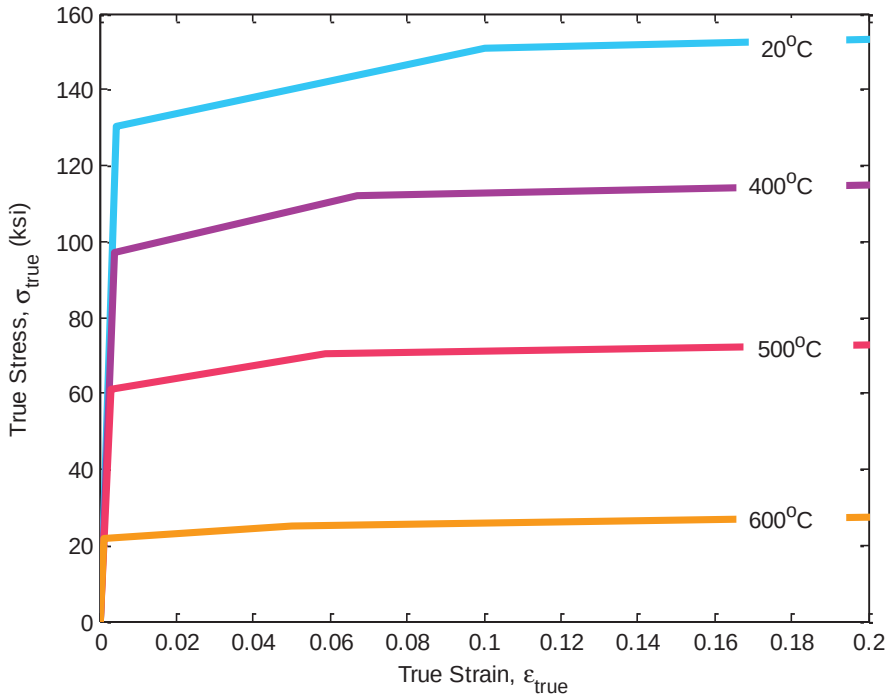

Fig. 8. True stress-strain curves for A325 bolts at 400 °C (1 ksi = 6.895 MPa).

than 5%). Results also show that increasing the temperature from 20 °C to 400 °C reduced the capacity of the connection by only about 20%. However, increasing the temperature from 400 °C to 500 °C reduced the capacity an additional 30%. By 600 °C, the ultimate capacity of the connection has dropped by about 70%.

In developing reduced models to capture the connection behavior at elevated temperatures, it is important to consider the contribution of each component of the connection in resisting axial loads. To this end, the total axial force in the WUF-B connection, as shown in Figure 9, can be decomposed into the axial forces in each of five components of the connection: the two flanges and three bolt rows. The axial force in a single flange can be obtained by summing the reaction forces of all nodes at the welded end of that flange (at the right end in Figure 2). Figure 10 shows a resulting plot of the axial force in a single flange of the WUF-B connection against the axial displacement imposed on the free end of the beam. The axial force in each bolt row can be obtained by defining three sets of nodes at the welded end of the shear tab, corresponding to three strips of the shear tab with equal height, each containing a single bolt. Summing the reaction forces of all nodes corresponding to a single strip then gives the force in that bolt row. Figure 11 shows a resulting plot of the axial force in a single bolt row against the axial displacement imposed on the free end of the beam.

Figures 10 and 11 (note the different scales on the vertical and horizontal axes) show that the flanges of the WUF-B connection have much greater capacity than the bolts and that they can sustain much greater deformations before fracture. The peak values in the total load-displacement curves in Figure 9 correspond to the ultimate load in the bolt rows, while the connection continues to sustain substantial load beyond this point through the contribution of the flanges. Figure 10 shows that at 20 °C, the flange of the WUF-B connection can sustain deformations exceeding 2 in. (51 mm). However, this axial deformation at fracture is about twice as large as what was calculated using a previously developed model of this WUF-B connection (Sadek et al., 2013). The differences are believed to be due partly to the modeling of the k-area of the beam section, where the web thickness increases as it joins the flange. The increased web thickness, which was accounted for by Sadek et al., but not in the present study, forces plastic deformations into a smaller portion of the flange, thus reducing the deformation at fracture. This issue, and other factors that may have contributed to the differences, are currently being investigated.

The failure modes of the WUF-B connection depend on the relative reduction in the yield capacity with the increase in temperature between the rolled steel sections and the bolts. As mentioned previously and shown in Figure 8, both the A572 steel and the A490 bolts sustain 80% of their

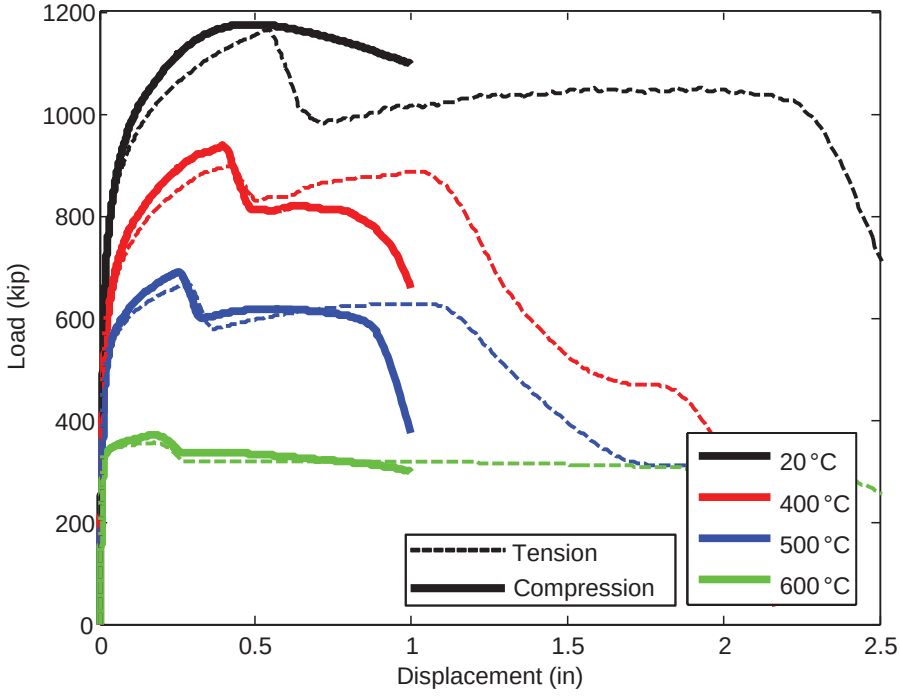

Fig. 9. Load-displacement curves for the WUF-B connection at different temperatures (1 kip = 4.448 kN, 1 in. = 25.4 mm).

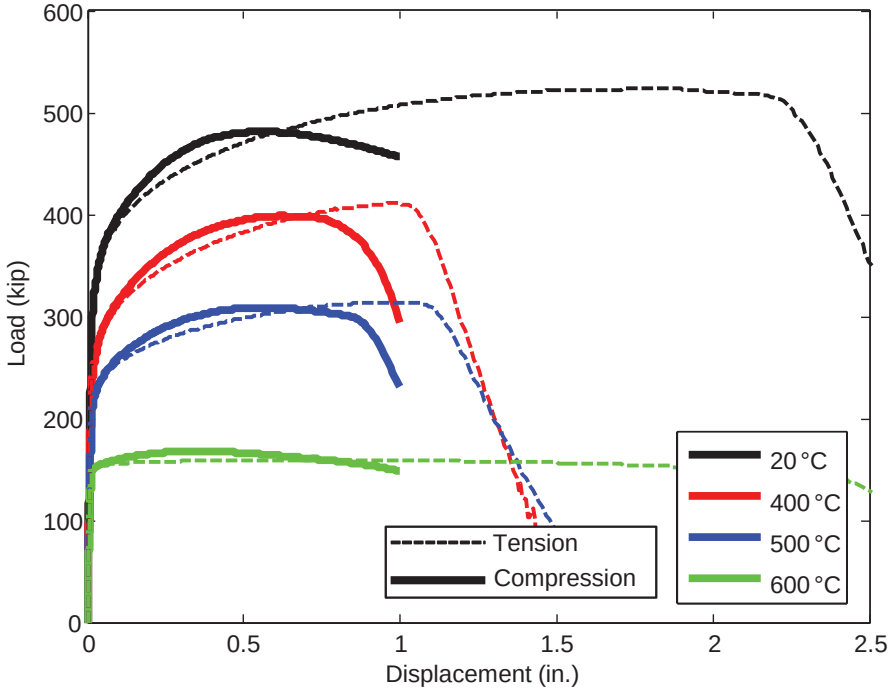

Fig. 10. Load-displacement curves for a single flange of the WUF-B connection at different temperatures (1 kip = 4.448 kN, 1 in. = 25.4 mm).

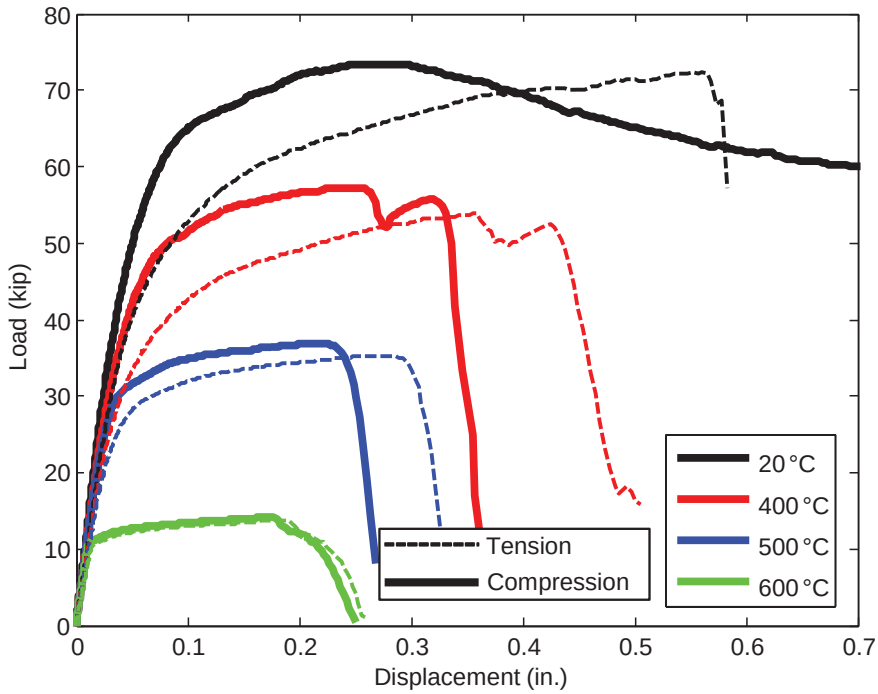

Fig. 11. Load-displacement curves for a single bolt row of the WUF-B connection at different temperatures (1 kip = 4.448 kN, 1 in. = 25.4 mm).

Table 3. Failure Modes Observed in the Computational Models of the WUF-B Connection at Different Temperatures under Tensile and Compressive Loading Conditions		
Temperature	Failure Mode Observed in Computational Model	
	Tension	Compression
20 °C	Shear fracture of bolts, followed by fracture of flanges (Figure 12a).	Beam local buckling, including bending of tab (Figure 13a)
400 °C	Tear-out of beam web, followed by fracture of flanges (Figure 12b)	Shear fracture in bolts, followed by local buckling (Figure 13b)
500 °C	Shear fracture of bolts, followed by fracture of flanges	Shear fracture in bolts, followed by local buckling
600 °C	Shear fracture of bolts, followed by fracture flanges	Shear fracture in bolts, followed by local buckling

yield strength until 400 °C, after which the A490 bolts lose their yield capacity much faster than the A572 steel. Failure modes have a mix of bolt and beam failure up to 400 °C, but only shear fracture failure modes occurred beyond the 400 °C.

The failure modes under tensile loading conditions can be summarized as follows:

1. At 20 °C, failure is due to shear fracture of the bolts, followed by fracture of the flanges, as shown in Figure 12a.
2. At 400 °C, tear-out of the beam web around the bolts is followed by fracture of the flanges, as shown in Figure 12b.
3. At 500 °C and 600 °C, the failure mode was similar to the 20 °C case.

The failure modes under compressive loading can similarly be summarized as follows:

1. At 20 °C, failure is due to local buckling of the beam cross-section. The tab also bends along the deformed beam section, and no fracture is observed, as shown in Figure 13a.
2. At 400 °C, 500 °C and 600 °C, failure is due to shear fracture of the bolts, followed by local buckling of the flanges, as shown in Figure 13b.

All failure modes observed in the computational models of the WUF-B connections at different temperatures under tensile and compressive loading conditions are summarized in Table 3.

CONCLUDING REMARKS

This paper presented a detailed finite element analysis approach to determine the performance and failure modes of steel-framed connections subject to elevated temperatures. Finite element models of typical shear and moment connections have been developed that incorporate temperature-dependent material models. Temperature-dependent material models for structural steel and bolts were supplemented with erosion-based failure criteria to simulate

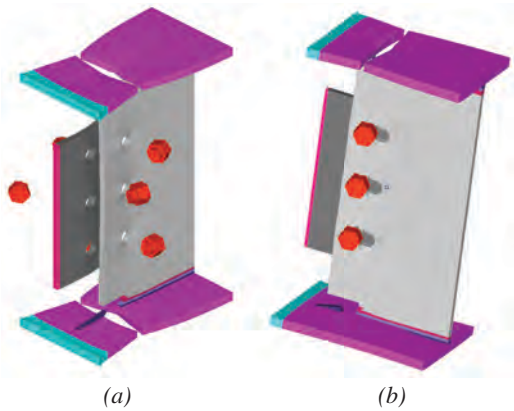

(a) (b)

Fig. 12. Failure modes of the WUF-B connection in tension: (a) shear fracture in bolts; (b) tear-out in beam web.

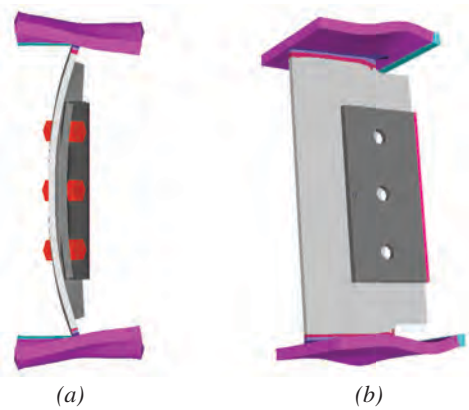

(a) (b)

Fig. 13. Failure modes of the WUF-B connection in compression: (a) local buckling of beam's cross-section; (b) shear fracture of bolts.

fracture. The erosion strains were calibrated by simulating experimental data on elongation of steel coupons at fracture to determine the appropriate local plastic strain value for the model mesh discretization.

The connection models were axially loaded in tension and compression for temperatures of 20 °C, 200 °C, 400 °C and 600 °C to identify primary failure mechanisms as a function of temperature, including fracture of bolts, beam and plate elements, local buckling of beam elements, and tear-out failure at bolt holes.

The effect of elevated temperature on the failure modes of WUF-B connections was presented in this paper. Increasing the temperature from 20 °C to 400 °C reduced the overall connection capacity by about 20% under both tensile and compressive loads. Further increasing the temperature from 400 °C to 500 °C reduced the capacity an additional 30%. By 600 °C, the connection had lost about 70% of its overall capacity.

Primary failure modes under tensile loading conditions were similar, where shear fracture of the bolts was followed by fracture of the beam flanges, except at 400 °C, where tear-out of the bolts through the beam web occurred rather than bolt fracture. Primary failure modes under compressive loading conditions changed between room temperature and temperatures at or above 400 °C. At 20 °C, the primary failure mode was local buckling of the beam cross-section, with no bolt fracture. At 400 °C and above, the failure mode changed to shear fracture of the bolts followed by local buckling of the cross-section.

DISCLAIMER

Certain commercial software or materials are identified to describe a procedure or concept adequately; such identification is not intended to imply recommendation, endorsement or implication by the National Institute of Standards and Technology (NIST) that the software or materials are necessarily the best available for the purpose.

REFERENCES

AISC (1999), *Load and Resistance Factor Design Specification for Structural Steel Buildings*, American Institute of Steel Construction, Chicago, IL.

AISC (2002), *Seismic Provisions for Structural Steel Buildings*, ANSI/AISC 341-02, American Institute of Steel Construction, Chicago, IL.

Al-Jabri, K.S., Seibi, A. and Karrech, A., (2006), "Modelling of Unstiffened Flush End-Plate Bolted Connections in Fire," *Journal of Constructional Steel Research*, Vol. 62, pp. 151–159.

ASCE (2002), *Minimum Design Loads for Buildings and Other Structures*, SEI/ASCE 7-02, American Society of Civil Engineers, Reston, VA.

ASTM (2011), "ASTM Standard E119-11a Standard Test Methods for Fire Tests of Building Construction and Materials," ASTM International, West Conshohocken, PA, 2009, DOI: 10.1520/E0119-11A.

FEMA (2000), "Recommended Seismic Design Criteria for New Steel Moment-Frame Buildings." FEMA 350, SAC Joint Venture and Federal Emergency Management Agency, Washington, DC.

Hu, G. and Morovat, M.A. (2009), "Elevated Temperature Properties of ASTM A992 Steel," *Structures Congress Proceedings*, ASCE, pp. 1067–1076.

Kodur, V., Kand, S. and Khaliq, W. (2012), "Effect of Temperature on Thermal and Mechanical Properties of Steel Bolts," *Journal of Material in Civil Engineering*, Vol. 24, No. 6, pp. 765–774.

Lew, H.S., Main, J.A., Robert, S.D., Sadek, F. and Chiarito, V.P. (2013), "Performance of Steel Moment Connections under a Column Removal Scenario. I: Experiments," *Journal of Structural Engineering*, ASCE, Vol. 139, No. 1, pp. 98–107.

LSTC (2012), "LS-DYNA Keyword User's Manual," Livermore Software Technology Corporation, Livermore, CA.

Luecke, W.E., McColskey, J.D., McCowan, C.N., Banovic, S.W., Fields, R.J., Foecke, T.J., T.A. Siewert, T.A. and Gayle, F.W. (2005), "Federal Building and Fire Safety Investigation of the World Trade Center Disaster, Mechanical Properties of Structural Steels," NIST NCSTAR 1-3D, National Institute of Standards and Technology, Gaithersburg, MD.

Quiel, S.E. and Garlock, M.E.M. (2010), "Parameters for Modeling a High-Rise Steel Building Frame Subject to Fire," *Journal of Structural Fire Engineering*, Vol. 1, No. 2, pp. 115–134.

Sadek, F., Main, J., Lew, H. and El-Tawil, S. (2013), "Performance of Steel Moment Connections under a Column Removal Scenario. II: Analysis," *Journal of Structural Engineering*, ASCE, Vol. 139, No. 1, pp. 108–119.

Sarraj, M., Burgess, I.W., Davison, J.B. and Plank, R.J. (2007), "Finite Element Modeling of Steel Fin Plate Connections in Fire," *Fire Safety Journal*, Vol. 42, pp. 408–415.

Seif, M. and McAllister, T. (2013), "Performance of Steel Shear Tab Connections at Elevated Temperatures." *Proceedings of Structural Stability Research Council Annual Stability Conference*, SSRC 2013, pp. 123–135.

Seif, M.S., McAllister, T.P., Main, J.A. and Luecke, W. (2015), "Finite Element Modeling of Structural Steel Component Failure at Elevated Temperatures," *Structures* (submitted).

Yang, K.C., Chen, S.J. and Ho, M.C. (2009), "Behavior of Beam-to-Column Moment Connections under Fire Load," *Journal of Constructional Steel Research*, Vol. 65, No. 7, pp. 1520–1527.

Yu, H., Burgess, I.W., Davison, J.B. and Plank, R.J. (2009), "Experimental Investigation of the Behavior of Fin Plate Connections in Fire," *Journal of Constructional Steel Research*, Vol. 65, pp. 723–736.

Fatigue Testing and Retrofit Details of High-Mast Lighting Towers

RYAN J. SHERMAN, MATTHEW H. HEBDON and ROBERT J. CONNOR

ABSTRACT

Fatigue cracking has been the cause of a number of high-mast lighting tower (HMLT) failures throughout the United States. In almost every case, forensic evaluations have shown cracking initiates and propagates due to wind-induced fatigue at mainly the base plate–to–tube wall connection detail or the hand-hole weld detail. Subsequent inspections of HMLT inventories have revealed a number of additional cases of fatigue cracking in various stages. Simply replacing the towers is not an economically feasible alternative because thousands of HMLTs are in use along major highways across the United States. As a result, strategies to retrofit existing HMLTs are needed. Results from laboratory testing performed on two HMLT retrofit configurations are presented. Both retrofits provided an increase in fatigue life compared with the as-built HMLTs. The retrofit strategies are employed without removing the pole from the foundation using simple bolting techniques and moderately skilled labor, providing cost savings for owners and increasing safety for the motoring public.

KEY WORDS: high-mast lighting tower (HLMT), fatigue, retrofit, sign structure.

BACKGROUND

Two high-mast lighting towers (HMLTs) near Rapid City, South Dakota, collapsed within five months of each other (November 2005 and April 2006). Both towers were identical hexadecagonal (16-sided), 150-ft-tall galvanized structures. Each pole had a base plate thickness of 1.75 in., tube wall thickness of 0.375 in., base diameter of 29 in., eight anchor rods and a complete-joint-penetration (CJP) weld with backing ring connecting the base plate to the tube wall. Failure in each case occurred at the base plate–to–tube wall connection detail. A forensic evaluation of both poles confirmed the cause of failure was wind-induced fatigue (Sherman et al., 2011). Fatigue cracks of various lengths, including those resulting in total collapse, have been observed in HMLTs around the United States (Connor et al., 2011). The two failures in South Dakota prompted a statewide inspection effort of approximately 140 towers. Cracking was discovered in both welded through-socket and full-penetration weld connection types: 14 instances and 3 instances, respectively. This resulted in 11 additional towers being removed from service. Sketches of these connection details can be found in Figure 1.

Fatigue of HMLTs typically has been a direct result of wind-induced vibration. HMLTs are flexible structures and can, therefore, experience rapid accumulation of damaging fatigue cycles. It is well established that there are two types of wind phenomenon that must be considered during the fatigue design of HMLTs: natural wind gusts and vortex shedding (AASHTO, 2013). Natural wind gusts cause the pole to move parallel to the direction of wind flow, while vortex shedding is a complex aero-elastic phenomenon. When wind flows past the pole at a steady rate, vortices are formed that create a wake. The force of the wake drives the pole back and forth perpendicular to the direction of the wind. When the pole is moving transverse to the direction of the wind flow, it is referred to as vortex shedding, which can produce a large number of stress cycles in a short period of time (Kaczinski et al., 1998; Ahern and Pucket, 2010).

From a survey conducted during a recent National Cooperative Highway Research Program (NCHRP) study (Connor et al., 2011) more than 10,000 HMLTs have been installed across the country. As such, robust, cost-effective retrofit strategies are needed because it is not economically feasible to replace all poles susceptible to fatigue cracking. One concept, referred to as "jacketing," has been developed. Retrofit jackets installed at the base plate and lowest portion of the pole shield the details commonly susceptible to fatigue crack growth: the base plate–to–tube weld connection detail and the hand-hole detail (Koob, 2007; Roy et al., 2011; Callahan and Connor, 2011). Comprised of multiple pieces, the jackets can be installed without removing the HMLT from service. The jacketing concept has been successfully installed

Ryan J. Sherman, Ph.D. Candidate, School of Civil Engineering, Purdue University, West Lafayette, IN (corresponding). Email: rjsherma@purdue.edu

Matthew H. Hebdon, Ph.D., P.E., Assistant Professor, The Charles Edward Via, Jr., Department of Civil Engineering, Virginia Tech, Blacksburg, VA. Email: mhebdon@vt.edu

Robert J. Connor, Ph.D., Associate Professor, School of Civil Engineering, Purdue University, West Lafayette, IN. Email: rconnor@purdue.edu

Paper No. 2014-21R

in Iowa and Texas on four different pole types (Koob, 2007). Field monitoring and laboratory fatigue testing were conducted on one Iowa HMLT to confirm the performance of the jacket retrofit (Connor and Hodgson, 2006; Phares et al., 2007; Callahan and Connor, 2011).

Details used on HMLTs in South Dakota required a retrofit jacket with different geometry than previously tested during research performed by Callahan and Connor (2011) to be fabricated; hence, there was concern the data obtained during that study were not directly applicable. Therefore, laboratory fatigue testing was conducted on jacket retrofits designed for typical South Dakota HMLT details. The research confirmed the jacket retrofit concept was an effective method for extending the life of HMLTs with and without existing fatigue cracks. This paper reports on the results of the experimental program, fit-up issues and general commentary on performance and detailing. The objective of this study was not to investigate causes of cracking (i.e., vortex shedding versus natural wind) or perform finite element analysis, but to focus on the development and testing of a robust retrofit strategy.

TEST SPECIMENS

General

Laboratory fatigue testing was conducted on three types of specimens: as-built specimens, tall-jacket retrofit specimens and short-jacket retrofit specimens. The first phase (as-built specimens) consisted of testing two HMLT base sections similar to in-service South Dakota HMLTs that experienced fatigue crack growth. The second phase (tall-jacket retrofit specimens) consisted of three specimens using a jacket retrofit approximately 60 in. tall fastened to a precracked, as-built specimen. The third phase (short-jacket retrofit specimens) consisted of three specimens using a jacket retrofit approximately 30 in. tall fastened to a precracked, as-built specimen.

The as-built specimens had a through-socket fillet-welded base connection detail typical of the majority of the in-service inventory in South Dakota where cracking had been observed. Socket-type connections are constructed by extending the tube base through a hole in the base plate and fillet welding around the perimeter at both the top and bottom of the base plate. In each jacket retrofit test, the base connection of the as-built pole was nearly completely severed (approximately 90%) with a cutting wheel to ensure the entire load was carried by the retrofit. This was conservative because an in-service structure would collapse if the base plate to tube weld were cracked to such a degree.

As-Built Test Specimens

Only the base section of the pole was tested as the location of fatigue-sensitive details, located within the bottom 72 in. of the HMLT, was tested. Two as-built specimens were tested to establish their baseline fatigue performance. No additional specimens were deemed necessary because the fatigue resistance of the as-built pole with the socket connection was known to be poor, typically worse than Category E′ (Rios, 2007; Roy et al., 2011). The as-built specimens were then used as a "fixture" for the jacket retrofit testing.

The as-built specimens were fabricated using a 35-ft-tall, 16-sided HMLT made of galvanized steel. The tube

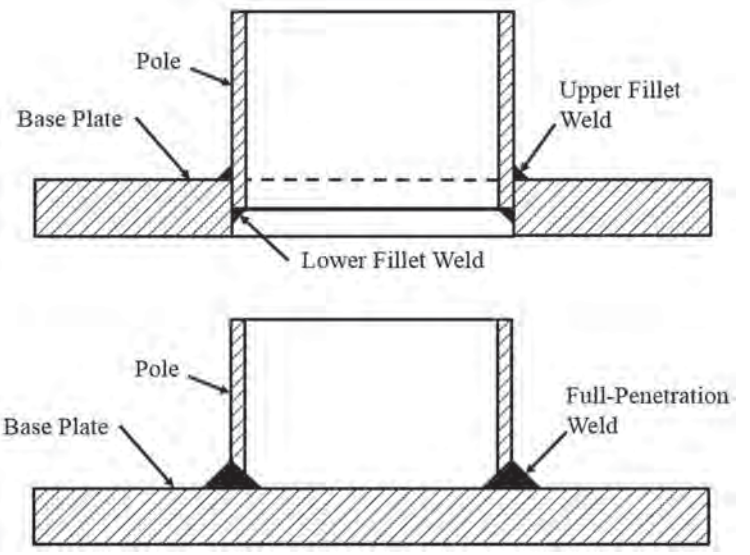

Fig. 1. Typical HMLT base connection details: welded-through socket (top) and full-penetration weld (bottom).

section base diameter was 25.89 in. and tapered at a rate of 0.14 in./ft. The tube wall thickness was 0.19 in., base plate thickness was 1.5 in. and ten 1.5-in. anchor rods secured the base plate to the foundation. A welded through-socket connection detail was used for the base plate-to-tube wall connection, and a doubler plate was used for the hand-hole detail. Strain gage locations for the as-built specimens can be seen schematically in Figure 2, and a photograph can be seen in Figure 3.

Tall-Jacket Retrofit Specimens

The tall-jacket geometry was similar to that used during a previous testing program sponsored by the Iowa Department of Transportation (DOT) (Callahan and Connor, 2011). Three identical tall-jacket retrofit specimens were tested to evaluate their fatigue performance on the same as-built specimen.

The tall-jacket retrofit specimen was comprised of two "half-jacket" base sections connected with splice plates. Both half-jacket sections were 60 in. tall and made of galvanized steel. One hundred fifty ⅞-in. A325 tension-controlled galvanized bolts were used to secure the new 0.5-in.-thick jacket tube wall to the existing tube wall of the pole. All holes were drilled through the existing tube wall using the retrofit jacket as a template. The holes were 1/16 in. over the fastener size. This number of fasteners was used to meet the American Association of State Highway and Transportation Officials (AASHTO) maximum fastener spacing and edge distance requirements and subsequently was well beyond the capacity required for strength considerations to ensure the as-built pole and jacket retrofit acted as one.

The new 1.5-in.-thick jacket base plate was attached to the original base plate with the ten existing anchor rods in addition to twelve 1.0-in. galvanized heavy hex A325 bolts. The A325 bolts connected the two base plates only, and had no connection to the concrete footing. In addition to the half jackets and splice plates, the tall-jacket retrofit also included four fill plates. Fill plates were required to ensure proper bolt tightening at the locations covered by the jacket directly above and below the hand-hole doubler plate. Figure 4 shows the strain gage locations used for the tall-jacket retrofit. A photograph of one of the tall-jacket halves can be found in Figure 5.

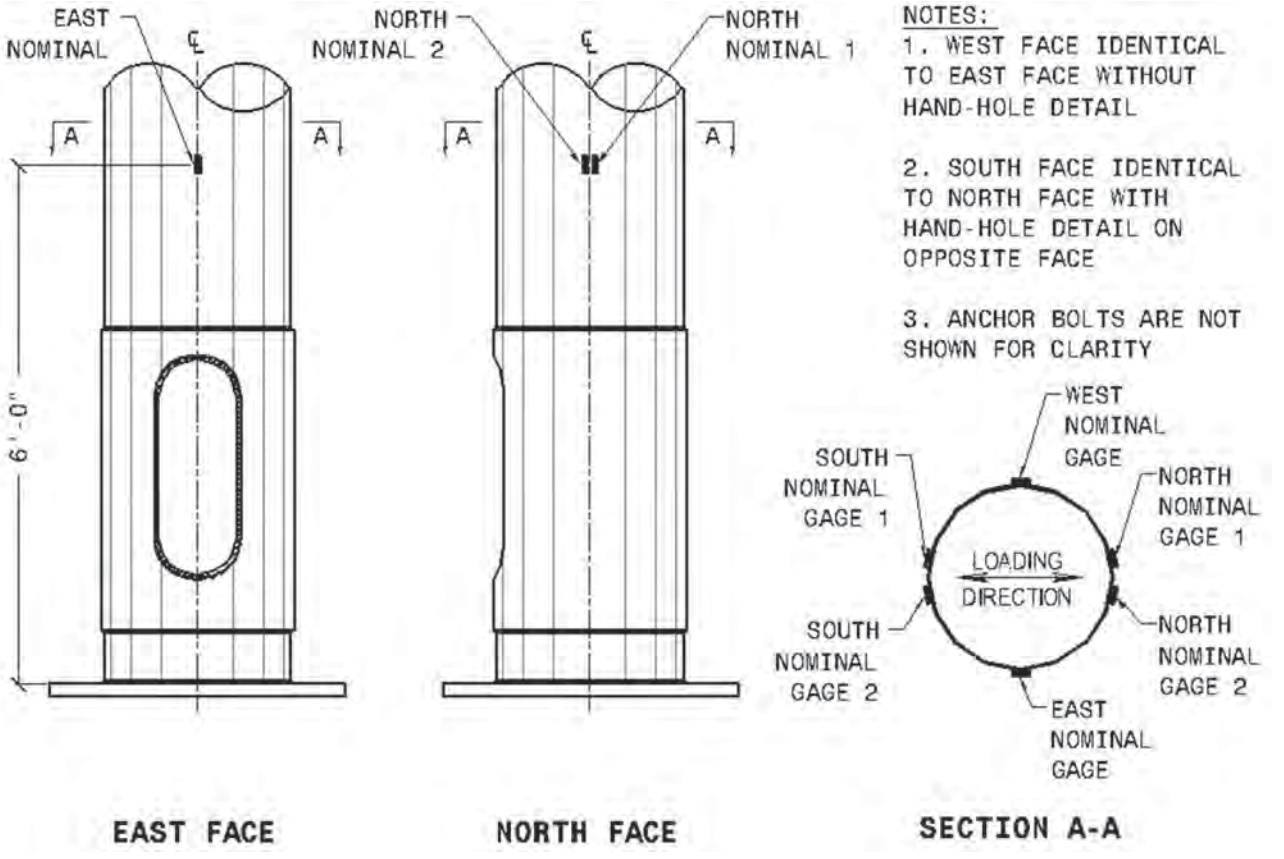

Fig. 2. Strain gage layout for as-built specimen.

Fig. 3. Base section of as-built test specimen (note doubler plate around hand-hole detail).

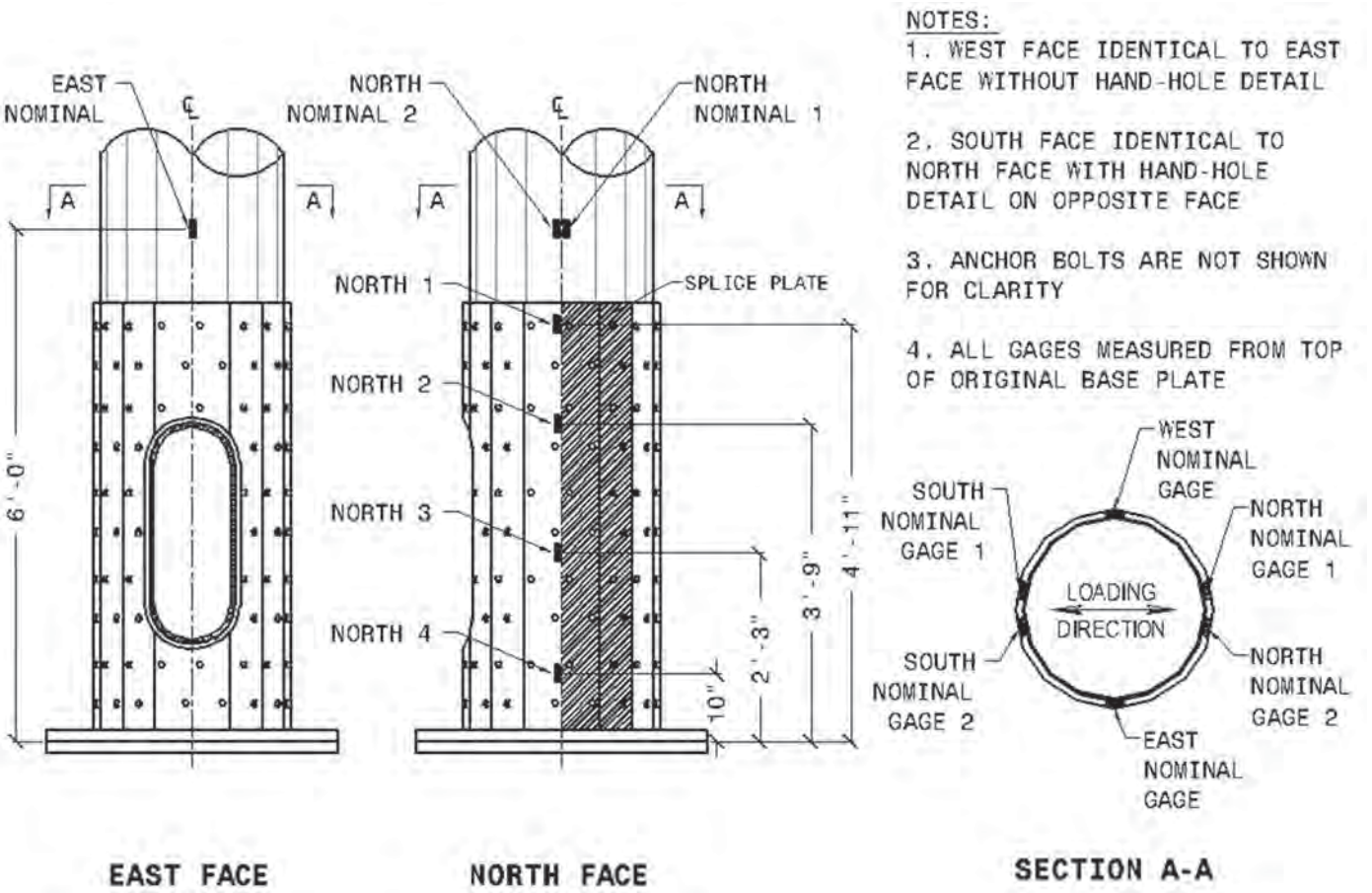

Fig. 4. Dimensions and strain gage layout of tall-jacket specimen.

Short-Jacket Retrofit Specimens

Although the tall retrofit proved to be effective, a second retrofit configuration was developed to reduce the installation challenges that had previously been observed in the field. After evaluating several alternatives, the decision was made to divide the jacket into quarters. Additionally, cracking had not been observed around the hand-hole during field inspections with the doubler plate hand-hole detail. Thus, field performance indicated the jacket did not need to extend above the hand-hole; therefore, the jacket was designed to extend approximately half the height of the tall-jacket retrofit. Reducing the height of the short-jacket retrofit lowered the fabrication cost and aided in quicker and easier installation.

Each short-jacket quarter was 31 in. tall, including the 1.5-in.-thick base plate. The short jacket had the same 0.5-in.-thick tube wall connected to a 1.5-in.-thick base plate with a CJP weld. The weld was inspected using ultrasonic testing during fabrication. Due to the reduction in height, only ninety-eight ⅞-in. A325 tension controlled bolts were required to secure the jacket tube wall to the existing tube wall of the pole. The ten existing anchor rods were used in addition to eighteen 1.0-in. galvanized heavy-hex A325 bolts to connect the new and existing base plates. Strain gage locations for the short jacket are shown in Figure 6. Photographs of the short-jacket retrofit can be found in Figure 7.

The primary differences between the tall and short jackets were height and number of components. Additionally, the short-jacket retrofit incorporated other modifications to resolve some fit-up issues encountered during the tall-jacket installation. Whereas the tall retrofit utilized splice plates between the tube walls of the two jacket halves, the short design eliminated these plates by considering the original as-built tube wall as a splice plate. Both fill plates were subsequently omitted from the short-jacket retrofit. The upper fill plate was no longer required because the top of the short jacket did not extend beyond the doubler plate of the hand-hole. The lower fill plate was omitted because the lowest row of bolts was relocated up to the doubler plate section. Collectively, these design improvements minimized problems experienced during the installation of the tall-jacket retrofit and reduced the total fabrication and installation costs.

Fig. 5. Typical tall-jacket retrofit.

Fabrication and Fit-Up Issues

Additional fabrication and fit-up issues were encountered during the installation of the jacket retrofits. A fabrication error resulted in poor alignment between the breaks in the pole and those in the jacket. It was believed to be a result of a combination of inaccurate field measurements and radial misalignment (see Figure 8 for resulting retrofit fit-up). This fabrication issue was only present in the short-jacket retrofit.

A tolerance issue was observed at the base plate–to–tube wall connection. The angle between the jacket base plate and jacket tube wall differed from the angle of the original pole. Due to the differing angles, full contact between all components was not achieved, resulting in an "oil canning" effect observed during the fatigue testing.

In addition, the internal winch plate on the as-built tube wall conflicted with bolt holes in both the tall and the short-jacket retrofits. The box in Figure 9 highlights the location of the conflict on the short-jacket retrofit. The decision was made to omit a number of fasteners to represent a worst-case field-installed condition.

Given the fabrication and fit-up issues encountered during the testing of the retrofits, the fatigue life results presented herein characterize a conservative representation for similar jacket retrofits. If these issues were improved a longer fatigue life would be expected.

EXPERIMENTAL TESTING

Experimental Test Setup—General

The HMLTs were tested in the vertical position. A reinforced concrete foundation, post-tensioned to the laboratory reaction floor, encased the full-size anchor rods supporting the HMLT. The anchor rod nuts were fastened to the base plate using the turn-of-the-nut tightening procedure and a hydraulic wrench (Dexter and Ricker, 2002). Cyclic loading was applied through an 11-kip MTS servo-controlled hydraulic actuator connected between the top of the HMLT

and the laboratory reaction wall (see Figure 10). To simulate worst-case stress conditions for the weld termination of the jacket, the load was applied perpendicular to the hand-hole location (from south to north). The hand-hole detail was located at the center of a jacket section. During the Iowa retrofit testing, it was found that locating the jacket splice through the hand-hole resulted in poor fatigue performance (Callahan and Connor, 2011).

Strain gages were installed to measure the nominal stress range in the as-built pole as well as to measure load transfer to the jackets. Due to the flexibility of the specimens, the MTS servo-controller was programmed using displacement control. The displacement range was manually adjusted throughout the test to maintain the desired nominal stress range as the specimen cracked. Static tests were conducted periodically during fatigue loading to monitor the stiffness of the pole. The fatigue test was considered complete upon a 10% drop in stiffness relative to the initial conditions or after substantial cracking: total crack length of approximately 20 in. Similar approaches were used on tests of flexible ancillary structures (Koenigs et al., 2003; Callahan and Connor, 2011). Magnetic-particle and liquid-dye-penetrant nondestructive testing were used to verify the crack lengths at the completion of each fatigue test.

Specimens were cycled at a constant amplitude stress range of 8 ksi measured with strain gages at a nominal location on the tube portion of the specimen. Maximum stresses were measured at the strain gages located on the north and south faces of the HMLT, in line with the actuator. Based on previous research, the 8-ksi stress range was found to be representative in terms of upper bound in-situ nominal stress range in poles of similar cross-section while minimizing test duration (Rios, 2007; Callahan and Connor, 2011). Additionally, field monitoring of HMLTs described in NCHRP Report 718 found 8 ksi to be an upper bound effective stress range (Connor et al., 2011). Nominal stresses were measured to avoid stress concentrations around the base plate–to–tube wall connection and to avoid any other jacket effects. The nominal stresses were extrapolated to the base using basic mechanics. Nominal stresses were selected to compare the relative fatigue resistance of the as-built pole with both jacket types. Strain gages were installed on the

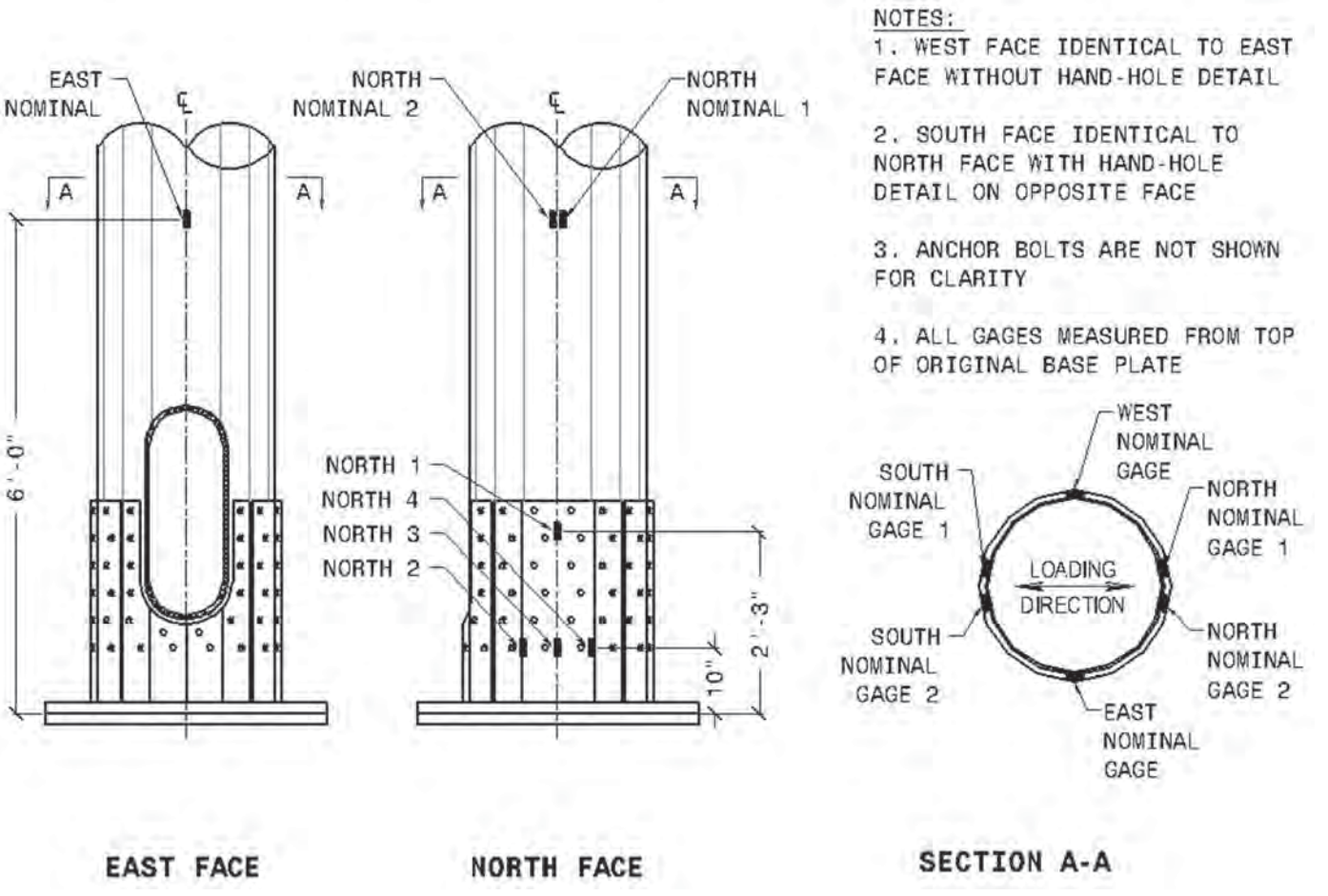

Fig. 6. Dimensions and strain gage layout of short-jacket specimen.

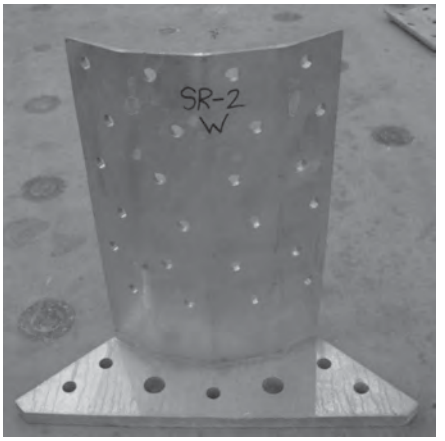

Fig. 7. Typical short-jacket retrofit.

Fig. 8. Short-jacket retrofit misalignment.

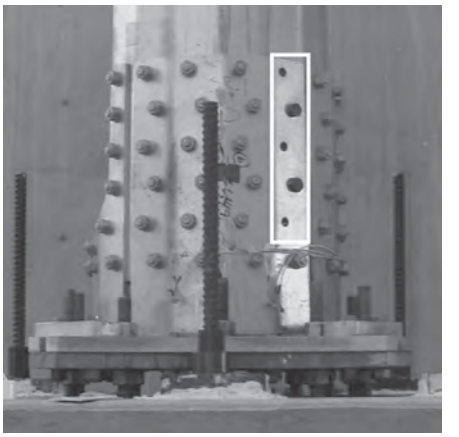

Fig. 9. Short-jacket retrofit with bolts removed at winch plate conflict.

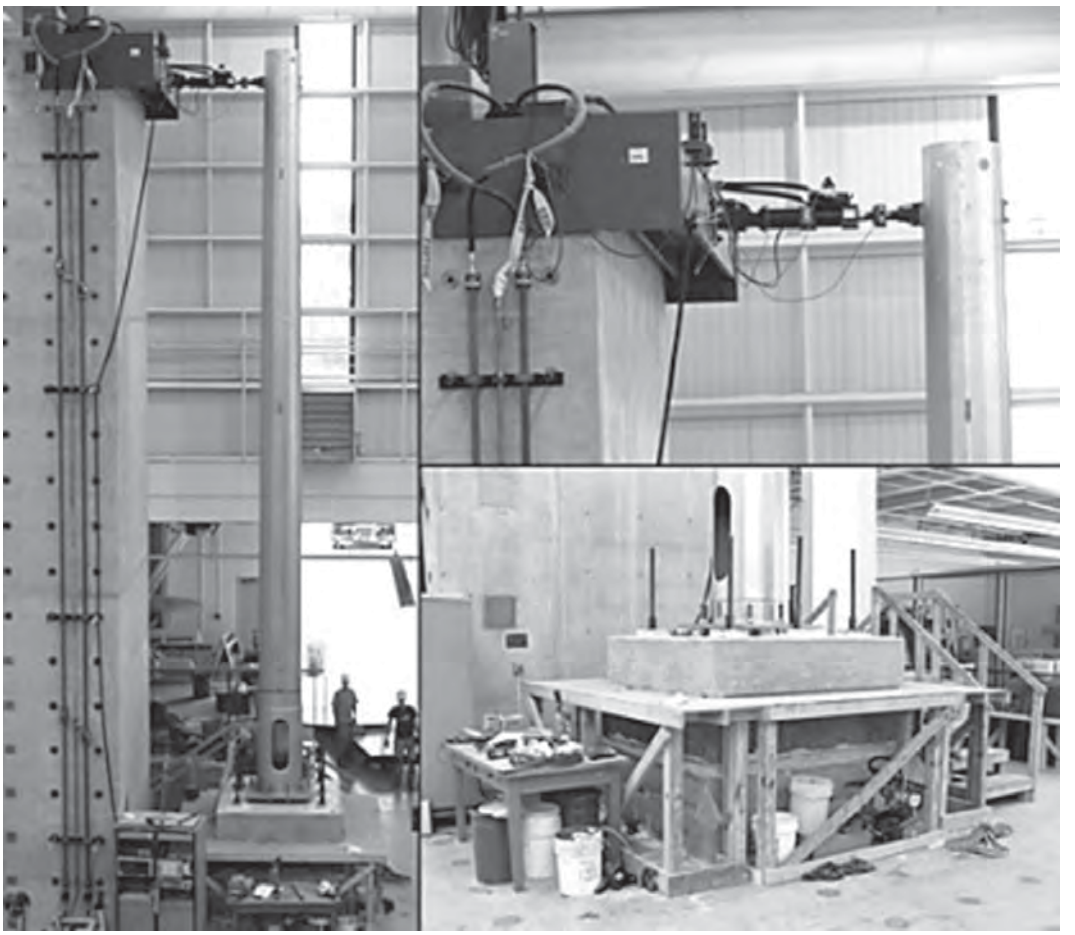

Fig. 10. As-built specimen test set-up (similar for all other specimens).

Table 1: Jacket Retrofit Performance Summary					
		Cycle Count		Final Crack Length (in.)	
Specimen	Projected* SR (ksi)	Crack First Observed	Final	North Face	South Face
AB_1	9.1	162,000	162,000	1.0	14.0
AB_2	9.1	25,800	260,000	21.5	17.0
TR_1	2.9	1,856,260	6,234,949	21.0	No crack
TR_2	2.9	—	10,045,448	No crack	No crack
TR_3	2.9	931,234	2,886,760	19.5	No crack
SR_1	2.9	309,008	1,145,540	17.0	2.0
SR_2	2.9	770,422	2,323,369	16.5	5.0
SR_3	2.9	1,498,373	5,037,731	11.8	7.9
* Nominal stress range in as-built pole 72 in. above base was 8 ksi for all specimens.					

jacket to establish the stress transfer distribution from the pole to the jacket. Though details of these measurements are not discussed herein, the data confirmed the jacket was fully engaged and no slip occurred between the jacket and as-built pole.

As-Built Specimen Results

At the 8-ksi constant stress range, the two as-built specimens lasted 162,000 cycles and 260,000 cycles (Specimens AB_1 and AB_2, respectively) before reaching failure (see Table 1). The resulting fatigue life was worse than category E′ and was comparable with previous research on HMLT through-socket connection details (Rios, 2007; Roy et al., 2011). Fatigue cracks formed at the points of maximum stress at the base plate-to-tube wall connection. Specimen AB_1 had cracks of 14 in. (see Figure 11) on the south and 3.5 in. on the north. Specimen AB_2 had cracks of 21.5 in. and 17 in. (south and north, respectively). All cracks initiated from the base plate to tube wall weld at the upper weld toe. Both tests were stopped due to the size of the fatigue cracks.

Tall-Jacket Retrofit Specimen Results

Three tall-jacket retrofit specimens were tested to establish their fatigue resistance. The addition of the tall-jacket retrofit resulted in a substantial increase in fatigue life of the as-built pole. At a stress range of 8 ksi in the as-built pole, specimen TR_1 had a fatigue life of 6,235,000 cycles, specimen TR_2 had a fatigue life of 10,045,000 cycles and specimen TR_3 had a fatigue life of 2,887,000 cycles

Fig. 11. Cracking on south face of AB_1.

Fig. 12. Specimen TR_1: north crack at upper weld toe after inspection with dye penetrant.

(see Table 1). In two specimens (TR_1 and TR_3), cracks formed at the tube-to-base plate connection in the upper weld toe at the point of maximum stress. Specimen TR_2 was considered a runout for this test after cycling more than 10,000,000 cycles. The other two specimens had fatigue cracks that initiated in the weld toe at the points of maximum stress. Figure 12 shows the completed TR_1 specimen with fatigue cracks after using dye penetrant to verify crack length. The final crack length for specimen TR_1 was 21 in., while TR_3 had a crack measuring 19.5 in. All tests were stopped due to the crack length.

Short-Jacket Retrofit Specimen Results

Strain gages were placed in similar locations as the tall jacket in order to compare behavior. The stress range was maintained in the as-built pole at 8 ksi for the short jackets. Specimen SR_1 had a fatigue life of 1,146,000 cycles, specimen SR_2 had a fatigue life of 2,323,000 cycles and specimen SR_3 had a fatigue life of 5,037,731 cycles before reaching failure (see Table 1). Fatigue cracks initiated at the points of maximum stress and generally had consistent crack growth. Cracks initiated at the upper weld toe of the base plate-to-tube wall connection and grew circumferentially. Each of the three specimens formed cracks at both sides of the jacket (where stresses were highest). Crack lengths varied from 2.0 in. to 17.0 in. (see Figure 13 for cracks on specimen SR_1). Once again, all tests were stopped due to crack length.

DISCUSSION

Results from the fatigue testing are summarized in Table 1. The nominal constant amplitude stress range measured in the tube wall, 8 ksi, versus the number of cycles to failure for each specimen was plotted on an *S-N* curve (see Figure 14), showing the increase in life for the jacket retrofits compared to the as-built pole specimens. This fatigue curve was indicative of the performance for in-service conditions because, for an in-service HMLT, the nominal stress-range due to loading does not change (i.e., wind or loading did not increase because a retrofit was installed). By comparing the *best* performing as-built pole specimen to the *worst* retrofit specimen (AB_2 to SR_1), an increase in life of greater than 440% was achieved.

Two potential reasons for the observed increase in fatigue performance were evaluated: (1) an improvement in category of the fatigue detail and (2) a decrease in the stress range at the controlling fatigue detail. The test data were examined to determine the primary factors for the increased fatigue life of the retrofits.

The nominal stress range for each test was projected to the base of the pole using basic mechanics of materials. Using the nominal stress was desired for comparison to eliminate any local stress concentration effects, base plate flexibility effects and local effects due to the jacket. Strain gage measurements were used to verify the calculated stresses and were representative of the behavior of the pole. In doing so, it was found that the vertical stress near the base appeared to be resisted by a section modulus that included the thickness of the original tube wall and retrofit jacket. As expected, the reinforcing plate around the hand-hole did not significantly contribute to the section modulus because it did not extend to the base of the pole (see Figures 2 and 3). The original tube wall was generally observed to act in conjunction with the jacket near the base, even though there was a gap between these two plates at the very bottom. However, at the very

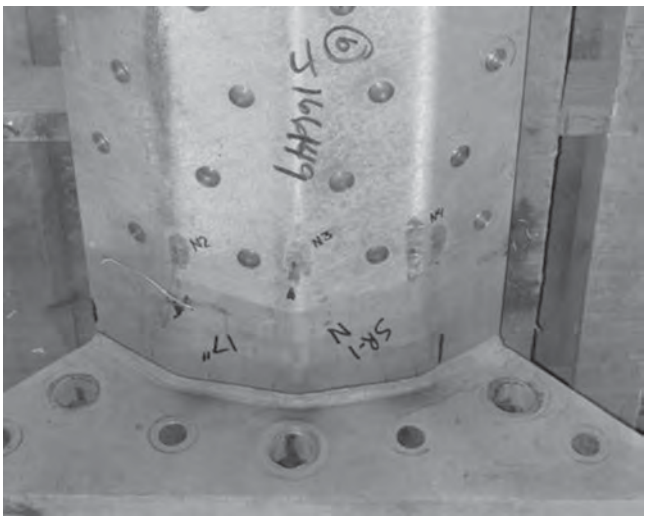

Fig. 13. Specimen SR_1: north crack at upper weld toe after inspection with dye penetrant.

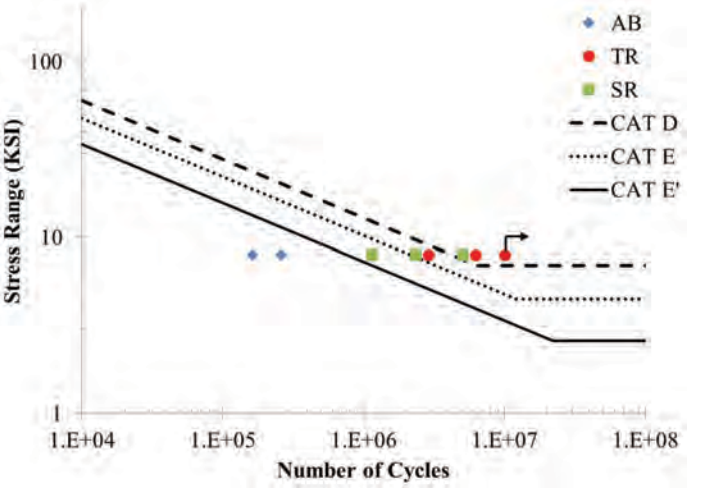

Fig. 14. Fatigue test data (nominal stress-range) plotted with AASHTO fatigue curves.

bottom of the retrofit jacket, adjacent to the weld, only the retrofit jacket was available to carry the moment due to the severed as-built pole to base connection. As a result, only cross-section of the retrofit jacket was used to calculate the stress range at this location. Using these revised stresses and the projected stresses from the as-built pole, the data were plotted again as shown in Figure 15.

Plotting the adjusted data indicated that the increase in fatigue life was primarily due to the decrease in stress range at the controlling fatigue detail and not due to a significant improvement in detail category. The sloped line through the fatigue data points in the *S-N* curve of Figure 15 suggested the behavior of the tall-jacket retrofit was approximately the same as the as-built pole. In fact, the fatigue behavior of the short-jacket retrofit appeared to be slightly worse than that of the as-built structure. The lower fatigue life was not surprising because the short jacket was observed to be more flexible. This added flexibility produced out-of-plane bending stresses near the base plate weld, which are not accounted for by the basic nominal stress range calculations. Thus, a lower fatigue life is observed. Figure 15 shows that the fatigue life of the short jackets was lower than both the as-built specimens and the tall jackets. Thus, the increase in life realized by adding the retrofit jacket was due to the drop in the effective stress range and not an improvement in fatigue category associated with the CJP weld.

Interpretation of Results

The lower fatigue performance of TR_3, compared with TR_1 and TR_2, is attributed to poor fit-up resulting in cyclic distortion between the original base plate and the base plate of the jacket. This was visually observed during testing. The distortion resulted in increased local stress ranges at the base plate weld of the jacket. Similar observations were made during the HMLT retrofit testing conducted for Iowa (Callahan and Connor, 2011).

The stress range applied in the laboratory was greater than the typical in-service effective stress ranges measured in the field on poles of similar cross-section. For example, the average nominal effective stress range in a nearly identical as-built pole located in Rapid City, South Dakota, was approximately 1.0 ksi (Connor et al., 2011). Further, based on field measurements of the Rapid City pole, an average of approximately 12,000 cycles were accumulated per day over an interval of about 590 days. Assuming all cycles less than 0.5 ksi were truncated (due to insignificance), a life estimate of an in-service retrofit jacket was made using the data collected from the in-service measurements in conjunction with the laboratory fatigue test data presented herein.

This estimate was made using several conservative, but reasonable assumptions:

1. The number of cycles per day (12,000) is reasonable based on the field measurements made at 11 other locations across the country as reported in NCHRP Report 718 (Connor et al., 2011).
2. If the laboratory pole was placed under identical loading conditions as the field-tested pole (Rapid City, South Dakota, as reported in NCHRP Report 718), the ratio of the section modulus of the field tested pole (S_{x_Field}) and laboratory pole (S_{x_Lab}), calculated to be approximately 2, should be applied to the field-measured effective stress range (S_{ref_Field}) to obtain the effective stress range of the laboratory pole and/or jacket (S_{ref_Lab}) in field-like conditions.

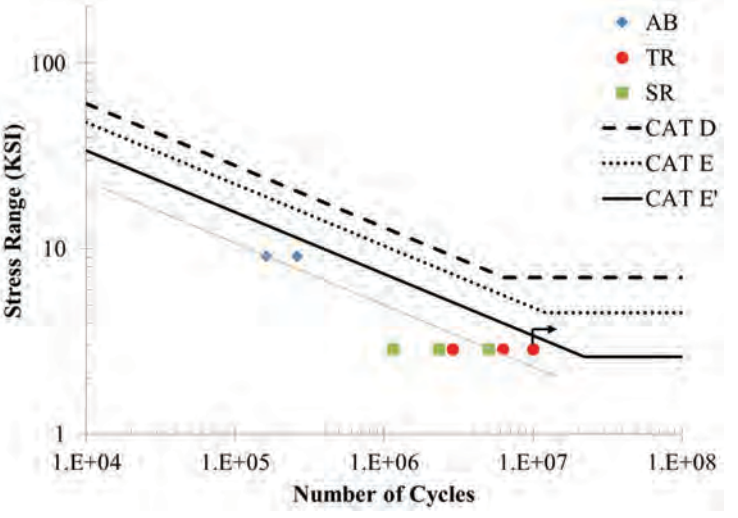

Fig. 15. Fatigue test data (nominal stress-range projected to base) plotted with AASHTO fatigue curves.

$$\left(S_{ref\_Lab}\right)\left(S_{x\_Lab}\right)=\left(S_{ref\_Field}\right)\left(S_{x\_Field}\right)$$

$$S_{ref\_Lab}=S_{ref\_Field}\left(\frac{S_{x\_Field}}{S_{x\_Lab}}\right)$$

$$=1\text{ ksi }(2)$$

$$=2\text{ ksi}$$

3. The number of cycles to failure follows the normal AASHTO *S-N* curve relation:

   $N=A/S_{ref}^{3}$

   where *A* is the detail constant

4. Although S_{ref} is less than the fatigue limit, the fatigue limit is exceeded in the variable amplitude stress range spectrum more than 1 in 10,000 times (i.e., all cycles contribute to damage).

Based on these assumptions the estimated number of cycles to failure, assuming the *poorest* performing of the six tested jackets was installed in the field with a completely severed base connection (an extreme, worst-case condition), was calculated as:

$$A=\left(N_{Field}\right)\left(S_{ref\_Field}\right)^{3}$$

$$=\left(N_{Lab}\right)\left(S_{ref\_Lab}\right)^{3}$$

$$N_{Field}=\frac{(1{,}145{,}540\text{ cycles})(8\text{ ksi})^{3}}{(2\text{ ksi})^{3}}$$

$$=7.3\times10^{7}\text{ cycles}$$

Converting cycles into years (assuming 12,000 cycles/day) yields:

$$\frac{7.3\times10^{7}\text{ cycles}}{\left(12{,}000\ \frac{\text{cycles}}{\text{day}}\right)\left(365\ \frac{\text{days}}{\text{year}}\right)}=16.7\text{ years}$$

Next, using the best performing as-built pole (i.e., no jacket) tested in the laboratory, the life of that same pole installed in the field can be estimated as follows:

$$N_{Field}=\frac{(260{,}000\text{ cycles})(8\text{ ksi})^{3}}{(2\text{ ksi})^{3}}$$

$$=1.7\times10^{7}\text{ cycles}$$

$$\frac{1.7\times10^{7}\text{ cycles}}{\left(12{,}000\ \frac{\text{cycles}}{\text{day}}\right)\left(365\ \frac{\text{days}}{\text{year}}\right)}=3.8\text{ years}$$

The preceding example indicates a life increase from 3.8 years to 16.7 years, or 440%. This approach was applied to all jacket retrofit specimens tested. Life increases ranged from the earlier reported 440% to greater than 3,800% for the run-out specimen, with an average life increase of 1,770%. During the fatigue testing, the jackets resisted the entire bending moment because the tube walls were completely severed. Thus, these calculations were a conservative assessment of the increase in fatigue life for a retrofitted HMLT.

CONCLUSIONS AND RECOMMENDATIONS

Based on the results of the research, the following conclusions and recommendations are made:

- The fatigue performance of the fillet-welded socket base connection is poor.
- Fabrication quality has a large impact on performance; therefore, onsite measurements of the pole to be retrofit are recommended to improve fit-up. Further, an ultrasonic testing (UT) examination should be performed on the base plate–to–tube wall connection detail.
- Installation and fit-up challenges associated with the tall-jacket retrofit concept are much greater than those associated with the short-jacket retrofit concept as tested herein. It is expected that dividing the tall jacket into quarters—though not explicitly tested as part of this research—will improve installation fit-up with little to no impact on fatigue performance (based on the results of the short-jacket retrofit).
- Both jacket retrofit concepts have been shown to provide an effective repair/retrofit solution for existing in-service HMLTs in extending their functional life more than 400%.

REFERENCES

AASHTO (2013), *Standard Specifications for Structural Supports for Highway Signs, Luminaries and Traffic Signals,* 6th ed., American Association of State Highway and Transportation Officials, Washington, DC.

Ahearn, E.B. and Pucket, J.A. (2010), *Reduction of Wind-Induced Vibrations in High-Mast Light Poles,* Wyoming Department of Transportation, Cheyenne, WY.

Callahan, G.L. and Connor, R.J. (2011), *Fatigue Performance of Multi-Sided High-Mast Lighting Towers and Bolted Retrofit Jackets—Final Report,* Purdue University, West Lafayette, IN.

Connor, R.J. and Hodgson, I.C. (2006), *Field Instrumentation, Testing, and Long-Term Monitoring of High-Mast Lighting Towers in the State of Iowa*, Iowa Department of Transportation, Ames, IA.

Connor, R.J., Collicott S.H., DeSchepper, A.M., Sherman, R.J. and Ocampo, J.A. (2011), *Development of Fatigue Loading and Design Methodology for High-Mast Light Poles* NCHRP Report 718, Transportation Research Board, National Research Council, Washington, DC.

Dexter, R. J. and Ricker, M. J. (2002), *Fatigue-Resistant Design of Cantilevered Signal, Sign, and Light Supports,* NCHRP Report 469, Transportation Research Board, National Research Council, Washington, DC.

Kaczinski, M.R., Dexter, R.J. and Dien, J.P.V. (1998), *Fatigue-Resistant Design of Cantilevered Signal, Sign and Light Supports,* NCHRP Report 412, Lehigh University, Washington, DC.

Koenigs, M.T., Botros, T.A., Freytag, D. and Frank, K.H. (2003), *Fatigue Strength of Signal Mast Arm Connections*, Texas Department of Transportation, Austin, TX.

Koob, M. (2007), "Base Connection Retrofits for High Mast Towers and Pole Luminaries Used for Roadway and Bridge Lighting," *Journal of Bridge Structures,* Vol., 3, No. 1, pp. 67–80.

Phares, B.M., Sarkar, P.P., Wipf, T.J. and Chang, B. (2007), *Development of Fatigue Design Procedures for Slender, Tapered Support Structures for Highway Signs, Luminaries, and Traffic Signals Subjected to Wind-Induced Excitation from Vortex Shedding and Buffeting,* Iowa State University, Ames, IA.

Rios, C.A. (2007), *Fatigue Performance of Multi-Sided High-Mast Lighting Towers,* The University of Texas at Austin, Austin, TX.

Roy, S., Park, Y.C., Sause, R., Fisher, J.W. and Kaufmann, E.J. (2011), *Cost-Effective Connection Details for Highway Sign, Luminaire, and Traffic Signal Structures,* NCHRP Web-Only Document 176, Transportation Research Board, National Research Council, Washington, DC.

Sherman, R.J., Connor, R.J. and Mueller, J.M. (2011), *Fatigue Testing and Retrofit Details in High-Mast Lighting Towers*, South Dakota Department of Transportation, Pierre, SD.